

Towards Efficient Three-Dimensional Wide-Angle Beam Propagation  
Methods and Theoretical Study of Nanostructures  
for Enhanced Performance of Photonic Devices

Naar efficiënte driedimensionale wijdhoek-bundelpropagatiemethodes  
en theoretische studie van nanostructuren  
voor verbeterde prestaties van fotonische componenten

Khai Quang Le

Promotor: prof. dr. ir. P. Bienstman  
Proefschrift ingediend tot het behalen van de graad van  
Doctor in de Ingenieurswetenschappen: Fotonica

Vakgroep Informatietechnologie  
Voorzitter: prof. dr. ir. D. De Zutter  
Faculteit Ingenieurswetenschappen en Architectuur  
Academiejaar 2010 - 2011



ISBN 978-90-8578-435-7  
NUR 959, 924  
Wettelijk depot: D/2011/10.500/39



Ghent University  
Faculty of Engineering and  
Architecture  
Department of Information Technology  
(INTEC)

**Promoter**

Prof. Dr. Ir. Peter Bienstman

Ghent University, INTEC

**Examiners**

Prof. Dr. Ir. Ronny Verhoeven  
(president)

Ghent University, Department of Civil  
Engineering

Prof. Dr. Trevor M. Benson

University of Nottingham, School of  
Electrical and Electronic Engineering

Prof. Dr. Ir. Geert Morthier

Ghent University, INTEC

Prof. Dr. Ir. Peter Bienstman  
(promoter)

Ghent University, INTEC

Prof. Dr. Ir. Jeroen Beeckman  
(secretary)

Ghent University, ELIS

Prof. Dr. Ir. Bjorn Maes

University of Mons, Faculty of  
Sciences

Ghent University

Faculty of Engineering and  
Architecture

Department of Information Technology  
(INTEC)

Sint-Pietersnieuwstraat 41, Ghent  
9000, Belgium

Tel: +32-9-264-3316

Fax: +32-9-264-3593

<http://www.intec.ugent.be>



# Acknowledgements

The dissertation is dedicated to my passed away grandmother and mother. I believe that they are always around to support me during the hard time doing a PhD in Belgium. I can imagine how happy they are when I get the PhD.

To finish the PhD I would like to thank Prof. Peter Bienstman for his brilliant supervision. He gave me a valuable chance to come to Belgium. To my deep heart he is not only an excellent advisor but also a big colleague. He is always very kind to discuss, encourage and listen to my “crazy” ideas. He introduced me to fascinating topics and always allowed me to do whatever I was interested in area of photonics. Such a flexible supervision helped me achieve a fruitful scientific output during my early research stages.

During this PhD period in the Photonics Research Group, I met a lot of nice people who were always willing to help me and made me feel the group as a big family. I really do not know how to express my gratitude to my beloved colleagues but best wishes to them will be always given from me.

I am very grateful to Dr. G. Ronald Hadley for his valuable discussions to my work related to the complex Jacobi iterative method in which he is a pioneer. My great thanks are devoted to Prof. Trevor Benson from the University of Nottingham, UK for giving me a great chance to do a 3-month-collaboration with his group in the framework of the COST Action MP0702. Such a valuable time in Nottingham was undoubtedly very helpful for my future.

I would like to thank Prof. Sangin Kim and Prof. Hanjo Lim from Ajou University, Korea for bringing me to Korea to study for a Msc degree. The time at Ajou University helped me build basic research skills as a key step for my early research stages.

I would also like to thank Prof. Vo Van Hoang, Prof. Dang Van Liet and Prof. Hoang Dung for their recommendations to my supervisors from Korea and Belgium.

Apart from doing research I cannot imagine how my life would be going in Belgium without my best friend Tran Diem Phuong and my Vietnamese friends who have been studying at UGent. I am very grateful for her sharing and for her encouraging my work. I would like to thank all members of my football team in Gent who helped me to release stress and recover energy.

Finally and always the most important part, my great gratitude is sent to my beloved grandmother, parents, brothers and sisters of my family for their support and encouragement to my life.

Ghent, March 2011

Khai Quang Le

# Table of contents

Acknowledgement	
List of acronyms	
Samenvatting	
Abstract	
Chapter I: Introduction .....	1
I.1. Context .....	1
I.2. Structure of this thesis .....	7
I.3. List of publications .....	8
References .....	11
Chapter II: The beam propagation method .....	13
II.1. Introduction .....	13
II.2. Frequency-domain BPMs .....	15
II.2.1. Scalar and paraxial BPMs .....	15
II.2.2. Vectorial BPMs .....	16
II.2.3. Wide-angle BPMs .....	17
II.2.4. Conventional Padé approximant operators for WA-BPMs .....	18
II.2.4.1. Padé approximant operators for WA beam propagation .....	18
II.2.4.2. Multistep solution for WA beam propagation .....	20
II.2.4.3. Boundary conditions for WA-BPMs .....	21
II.2.4.4. Slanted-wall beam propagation using the Padé(1,1) operator .....	22
II.3. Time-domain BPMs .....	25
II.3.1. Time-domain BPMs for treating reflected waves .....	26
II.3.2. Time-domain BPMs for modeling ultrashort pulses in wide-angle structures .....	26
II.4. Conclusion .....	27
References .....	28
Chapter III: New Padé approximant operators for WA-BPMs .....	31
III.1. Modified Padé approximant operators .....	31
III.1.1. Formulation .....	32
III.1.2. Example .....	34

III.1.3. Generalized rectangular WA-BPMs using modified operators .....	38
III.1.4. Application of modified Padé approximant operators for time-domain BPMs .....	42
III.1.4.1. Time-domain BPMs for treating reflected waves .....	42
III.1.4.2. Time-domain BPMs for modeling ultrashort pulses in wide-angle structures .....	45
III.1.5. Comparative assessment of time-domain models for nonlinear optical propagation .....	49
III.2. KP approximant operators for WA-BPMs without using slowly varying envelope approximation .....	54
III.2.1. Formulation .....	54
III.2.2. Analytical assessment .....	55
III.2.3. Example .....	57
III.3. Conclusion .....	59
References .....	61
Chapter IV: Iterative Helmholtz solvers for solution of beam propagation .....	63
IV.1. The Helmholtz equation .....	64
IV.2. The iterative Krylov subspace methods .....	65
IV.2.1. GMRES .....	65
IV.2.2. Bi-CGSTAB .....	67
IV.2.3. Application in beam propagation .....	70
IV.3. CJI .....	71
IV.3.1. Formulation .....	71
IV.3.2 Example .....	72
IV.4. Conclusion .....	73
References .....	74
Chapter V: Three-dimensional wide-angle beam propagation using CJI .....	75
V.1. Adaptation of CJI for 3D wide-angle beam propagation .....	76
V.1.1. Formulation .....	76
V.1.2. Convergence studies of CJI .....	77
V.1.3. Benchmark results .....	78
V.2. Efficient CJI-WA-BPMs for beam propagation in nonlinear waveguides .....	81

V.3. High order Padé approximant-based 3D WA-BPMs using CJI .....	84
V.4. Stable semivectorial CJI-WA-BPM using the iterated Crank-Nicholson method .....	86
V.4.1. Formulation .....	87
V.4.2. Convergence study of semivectorial CJI-WA-BPM .....	89
V.5. CJI-WA-BPMs: integrated in LightPy framework .....	91
V.6. Conclusion .....	93
References .....	95
Chapter VI: New approximate solution for wave propagation in graded-index metamaterials .....	97
VI.1. Formulation .....	98
VI.1.1. Real Padé approximant operators .....	99
VI.1.2. Modified Padé approximant operators .....	100
VI.1.3. Numerical implementation of Padé-based wave propagation .....	101
VI.2. Example .....	101
VI.3. Conclusion .....	102
References .....	103
Chapter VII: Enhanced sensitivity of silicon-on-insulator surface plasmon interferometer with additional silicon layer .....	105
VII.1. SPI on SOI .....	106
VII.1.1. Device structure .....	106
VII.1.2. Sensing principle .....	106
VII.2. Enhanced sensitivity of SOI-SPI by additional Si top layer .....	108
VII.2.1. Sensitivity enhancement .....	108
VII.2.2. Optimization: towards chip-scale sensors .....	111
VII.3. Conclusion .....	115
References .....	116
Chapter VIII: Enhanced light emission of silicon LEDs with plasmonic nanoparticles .....	117
VIII.1. An improved model of plasmonic nanoparticles enhanced light emitters .....	118
VIII.2. Optical properties of a random assembly of nanoparticles .....	121
VIII.3. Enhanced light emission of silicon LEDs by isolated nanoparticles .....	123
VIII.4. Conclusion .....	125

References .....	126
Chapter IX: Enhanced light absorption of thin-film silicon solar cells by plasmonic core-shell nanostructures .....	127
IX.1. Optical properties of a single core-shell nano-antenna .....	128
IX.2. Enhanced light absorption by a single nano-antenna .....	130
IX.3. Conclusion .....	132
References .....	133
Chapter X: Summary and perspectives .....	135
X.1. Summary .....	135
X.2. Perspectives .....	136
References .....	137

# List of acronyms

2D, 3D	Two-dimensional, three-dimensional
ADI	Alternating-direction implicit
Ag	Silver
Au	Gold
AWG	Arrayed waveguide grating
Bi-BPM	Bidirectional beam propagation method
Bi-CGSTAB	Bi-conjugate gradient stabilized
BPM	Beam propagation method
CAD	Computer-aided design
CG	Conjugate gradient
CJI	Complex Jacobi iterative
CJI-WA-BPM	Wide-angle beam propagation method using CJI
DMI	Direct matrix inversion
DtN	Dirichlet-to-Neumann
EM	Electromagnetic
EME	Eigenmode expansion
FD-BPM	Finite difference beam propagation method
FDTD	Finite difference time domain
FE-BPM	Finite element beam propagation method
FFT-BPM	Fast Fourier transform beam propagation method
FOM	Figure of merit
FWHM	Full-width at half maximum
GMRES	Generalized minimal residual
GNLSE	Generalized nonlinear Schrodinger equation
GR-WA-BPM	Generalized rectangular wide-angle beam propagation method
ICN	Iterated Crank-Nicholson
LEDs	Light emitting diodes
MINRES	Minimal residual

MMI	Multimode interference
MoL	Method of lines
PICs	Photonics integrated circuits
PLCs	Planar lightwave circuits
PML	Perfectly matched layer
RIU	Refractive index unit
SC	Solar cell
Si	Silicon
SiO <sub>2</sub>	Silica
SOI	Silicon-on-insulator
SPI	Surface plasmon interferometer
SPP	Surface plasmon polariton
SPR	Surface plasmon resonance
SVEA	Slowly varying envelope approximation
S-WA-BPM	Standard wide-angle beam propagation method
TBC	Transparent boundary condition
TD-BPM	Time-domain beam propagation method
TLM	Transmission line modeling
WA-BPM	Wide-angle beam propagation method
WDM	Wavelength demultiplexing

# Samenvatting

In dit doctoraat stellen we een nieuwe klasse van approximanten voor, de zogenaamde gewijzigde Padé approximant operatoren, voor gebruik in de wijdhoek-bundelpropagatiemethode (WA-BPM). Deze nieuwe operatoren laten niet alleen een nauwkeurigere benadering van de Helmholtzvergelijking toe dan conventionele operatoren, maar ze geven ook de vereiste demping aan evanescente modi. We hebben ook de voordelen van deze nieuwe operatoren aangetoond voor de oplossing van problemen met bundelpropagatiemethodes in het tijdsdomein. We hebben dit onder meer gedaan voor de analyse van een drie-dimensionele fotonische component, nl. een 1x4 multimode interferentie koppelaar (MMI). De resulterende methode biedt het voordeel een grotere propagatiestap te kunnen gebruiken dan bij de klassieke methodes, bij gelijkblijvende nauwkeurigheid, hetgeen een aanzienlijke reductie in rekentijd met zich meebrengt.

We hebben ook het nut aangetoond van deze nieuwe operatoren voor de oplossing van bundelpropagatiemethodes in het tijdsdomein. We hebben dit gedaan zowel voor een breedbandmethode die reflecties kan in rekening brengen, als voor een split-step methode om ultrakorte unidirectionele pulsen te modelleren. De resulterende aanpakken halen een hoge-orde-accuraatheid, niet alleen in de ruimte, maar ook in de tijd.

Bovendien hebben we een aanpassing voorgesteld van de onlangs voorgestelde complexe Jacobi iteratieve methode (CJI) om wijdhoek-bundelpropagatieproblemen op te lossen, gebaseerd op de eenvoudige Padé(1,1) approximant operator. Voor bundelpropagatie in golfgeleiderprofielen met een 2D doorsnede, kan de breedhoek-bundelpropagatiemethode geformuleerd worden in termen van een Helmholtzvergelijking met bronterm, waarbij de effectieve absorptie (of verlies in het medium) die in deze vergelijkingen optreedt bijzonder hoog is, hetgeen leidt tot een snelle convergentie van de CJI aanpak. We hebben ook aangetoond dat de CJI methode voor breedhoek-bundelpropagatiemethodes gebaseerd op de gewijzigde Padé(1,1) approximant operator nog sneller convergeert dan deze gebaseerd op de gewone operator. Dit kan verklaard worden door het feit dat het effectieve verlies dat optreedt in de propagatievergelijking groter is bij de gewijzigde operator dan bij de gewone operator.

We hebben eveneens een CJI oplossing voorgesteld voor 3D breedhoek-bundelpropagatiemethodes gebaseerd op hogere orde Padé(3,3) approximant operatoren. De

resulterende CJI-WA-BPM geeft nauwkeurigere resultaten en convergeert sneller dan andere state-of-the-art solvers voor breedhoek-bundelpropagatie. Voor grote 3D problemen waar het brekingsindexprofiel varieert in de propagatierichting kan de CJI methode bundelpropagatie vier keer sneller uitvoeren vergeleken met andere state-of-the-art methodes. Voor praktische problemen blijkt de CJI-WA-BPM bijzonder nuttig te zijn, zoals b.v. voor de studie van grote componenten zoals de arrayed waveguide grating (AWG) in het silicium-op-isolator materiaalsysteem, waar onze groep onderzoek naar verricht.

Naast niet-lineaire BPM's in het tijdsdomein hebben we ook naar niet-lineaire BPM's in het frequentiedomein gekeken, en hebben we de CJI-WA-BPM uitgebreid voor niet-lineaire golfgeleiderproblemen. Uit benchmark tests en vergelijkingen met andere state-of-the-art methodes is gebleken dat de niet-lineaire CJI-WA-BPM zeer efficiënt is in termen van rekentijd.

We hebben ook een semi-vectoriële versie van de CJI-WA-BPM ontwikkeld die polarisatie-effecten in rekening kan brengen, maar die de koppeling tussen de veldcomponenten verwaarloost. We hebben de invloed van deze effecten onderzocht op de convergentiesnelheid van de semi-vectoriële CJI-WA-BPM. Het blijkt dat voor 3D golfgeleiders met een constant brekingsindexprofiel de resulterende iteratieve BPM nog altijd snel convergeert. Voor golfgeleiders daarentegen met een variabel brekingsindexprofiel in de propagatierichting blijkt de implementatie last te hebben van het feit dat het aantal iteraties tussen twee opeenvolgende doorsnedes snel oploopt tijdens de propagatie. Om dit probleem op te lossen, stelden we voor om de iteratieve Crank-Nicholson (ICN) methode te gebruiken. De resulterende CJI-WA-BPM met de ICN methode is stabiel en biedt aanzienlijke voordelen in termen van rekensnelheid voor semi-vectoriële bundelpropagatie over zeer lange afstanden.

Tevens hebben we een andere klasse van approximanten voorgesteld die we de KP approximanten genoemd hebben, en die gebruikt kunnen worden voor WA-BPM zonder gebruik te moeten maken van de benadering van de traag variërende omhullende. De resulterende aanpak laat toe om meer nauwkeurige benaderingen van de Helmholtz vergelijking door te voeren dan bij de klassieke en de gewijzigde Padé approximant operatoren in een breed bereik van parameters.

Naast wijdhoek-bundelpropagatieproblemen voor uniforme golfgeleiderstructuren, hebben we ook een nieuwe benaderende oplossing voorgesteld voor golfpropagatie in metamaterialen met

gradueel veranderende brekingsindex. Deze methode is zeer beloftevol voor dergelijke complexe problemen.

Aan de andere kant hebben we ook een studie doorgevoerd omtrent performantieverbetering van optische componenten zoals labelvrije biosensoren, licht-emitterende diodes en zonnecellen. We hebben dit gedaan aan de hand van numerieke en analytische methodes.

We hebben een oplossing voorgesteld om de gevoeligheid te verhogen van een silicium-op-isolator oppervlakteplasmon-interferometer biosensor die eerder was voorgesteld in onze groep. Met onze aanpak is de gevoeligheid met een factor vijf verhoogd. Dit is zo zowel voor de bulk sensing mode als voor de oppervlakte sensing mode van de sensor. We hebben ook de redenen achter deze verbetering verduidelijkt, en die blijken verschillend te zijn dan bij andere gevallen uit de literatuur. In ons geval is de verbetering te danken aan een verhoogde symmetrie van de twee oppervlakteplasmonmodes van de interferometer.

We hebben ook een verbeterd model opgesteld om de invloed van metaaldeeltjes te onderzoeken op het emissiegedrag van licht-emitterende diodes. Deze verbetering kwam tot stand door een aanpassing van een eerder voorgesteld model gebaseerd op de effectieve mode volume theorie. Dit nieuwe model levert resultaten die goed overeenstemmen met experimentele gegevens. Bovendien hebben we het gebruik van de effectieve medium theorie voorgesteld om de optische eigenschappen te beschrijven van een willekeurig ensemble van individuele nanopartikels. De correctheid van het model is aangetoond via een vergelijking met Mie theorie.

Tot slot hebben we het nut aangetoond van kern-schil nanostructuren als nanoantennes om de lichtabsorptie te verbeteren in dunnefilm-zonnecellen in amorf silicium. Uit onze studie blijkt dat de beste plaats voor deze antennes bovenop de cel is. We hebben theoretisch een performantieverhoging van 33% aangetoond.

# Abstract

In this dissertation, we have proposed a novel class of approximants, the so-called modified Padé approximant operators for the wide-angle beam propagation method (WA-BPM). Such new operators not only allow a more accurate approximation to the true Helmholtz equation than the conventional operators, but also give evanescent modes the desired damping. We have demonstrated the benefits of these modified operators for beam propagation analysis of a three dimensional (3D) practical photonic device i.e a 1x4 multimode interference (MMI) coupler. The resulting method can offer the advantage of using larger propagation steps than the conventional method for the same accuracy, with an associated reduction in computation times.

We have also demonstrated the usefulness of these new operators for the solution of time domain beam propagation problems. We have shown this both for a wideband method, which can take reflections into account, and for a split-step method for the modeling of ultrashort unidirectional pulses. The resulting approaches achieve high-order accuracy not only in space but also in time.

We have extended the resulting time domain BPMs based on these modified operators for nonlinear propagation problems. Through a comparative assessment with the rigorous time domain transmission line method, it results in a promising alternative method for demanding problems in terms of more efficient execution speed.

In addition, we have proposed an adaptation of the recently introduced complex Jacobi iterative (CJI) method for the solution of three dimensional wide-angle beam propagation problems based on the simple Padé(1,1) approximant operator. For beam propagation in waveguide profiles with a 2D cross section, the wide-angle beam propagation equation can be recast in terms of a Helmholtz equation with a source term, and the effective absorption (or medium loss) coefficient appearing in this equation is very high, leading to the rapid convergence of the CJI method. It has been found that the CJI solution of the wide angle beam propagation based on the modified Padé(1,1) approximant operator converges faster than that based on the conventional one. It is attributed to the fact that the effective absorption appearing in the propagation equation based on the modified operator is higher than the conventional operator.

Furthermore, we have demonstrated the CJI solution for the 3D wide-angle beam propagation method based on higher order of Padé(3,3) approximant operators. The resulting CJI-WA-BPM offers more accurate results and still converges quicker than other state-of-the-art solvers for wide-angle beam propagation. For large 3D waveguide problems with refractive index profiles varying in the propagation direction, the CJI method can speed up beam propagation up to four times compared to other solvers chosen here. For practical problems, the resulting CJI-WA-BPMs are found to be very useful to simulate a big component such as an arrayed waveguide grating (AWG) in the silicon-on-insulator platform, which our group is looking at.

Apart from time domain nonlinear BPMs, we have also looked at frequency domain nonlinear BPMs and we have extended the CJI-WA-BPM for nonlinear waveguide problems. Through benchmark tests with other state-of-the-art methods for such a demanding problem, we have found out that the resulting nonlinear CJI-WA-BPM is very efficient in terms of computational speed.

We have also developed a semivectorial CJI-WA-BPM which takes polarization effects into account but ignores the coupling between the field components. We have investigated the influence of these effects on the convergence rate of the semivectorial CJI-WA-BPM. It has been found that for 3D waveguides with constant refractive index profile the resulting iterative BPM still converges rapidly. However, for waveguides with varying index profile a straightforward implementation suffers from the fact that the iteration count between two successive cross sections increases dramatically during the propagation direction. To overcome this problem, we have proposed to use the iterated Crank-Nicholson (ICN) method. The resulting CJI-WA-BPM using the ICN method is stable and offers significant advantages in terms of execution speed for semivectorial beam propagation over a very long path length.

Furthermore, we have proposed another new class of approximants that we called the KP approximants, which can be used for WA-BPM without using the slowly varying envelope approximation. The resulting approach allows more accurate approximations to the true Helmholtz equation than the conventional and modified Padé approximant-based approaches in a wide range of parameters.

Apart from WA beam propagation problems for uniform waveguide structures, we have developed novel Padé approximate solutions for wave propagation in graded-index

metamaterials. The resulting method gives an excellent approximation to the true wave propagation. Thus, it offers a very promising tool for such demanding problems.

On the other hand, we have carried out the study of improved performance of optical devices such as label-free optical biosensors, light-emitting diodes and solar cells by means of numerical and analytical methods.

We have proposed a solution for enhanced sensitivity of a silicon-on-insulator surface plasmon interference biosensor which had been previously proposed in our group. The resulting sensitivity has been enhanced up to five times. This enhancement is true for both bulk and surface sensing modes of the sensor. We have elucidated the mechanisms behind this improvement, which is different from the ones described in literatures. In our case, the enhancement is attributed to the increased symmetry of the two surface plasmon modes of the interferometer.

Furthermore, we have developed an improved model to investigate the influence of isolated metallic nanoparticles on light emission properties of light-emitting diodes. The improvement has been achieved by a modification of the previously proposed model based on the effective mode volume theory. The resulting model has compared very well to experimental results. In addition, we have proposed the use of the effective medium theory to describe the optical properties of a random assembly of individual nanoparticles as a means to the optimal design of nanoparticles for enhanced light emitters. The validity of the model has been confirmed via a comparison to Mie theory.

Finally, we have proposed the usefulness of core-shell nanostructures as nanoantennas to enhance light absorption of thin-film amorphous silicon solar cells. Through an investigation of optical properties of a single core-shell antenna, the best place to add the antenna was found to be on top of the solar cells. As a result, an increased absorption up to 33 % has theoretically been demonstrated.

# Chapter I

## Introduction

### I.1. Context

The dissertation is devoted to developing efficient three-dimensional (3D) wide-angle beam propagation methods (WA-BPMs) and to theoretically studying nanostructures to improve the performance of photonic devices. Therefore, this thesis consists of two different parts.

The first part focuses on the development of novel and fast beam propagation methods to design 3D optical waveguides effectively. This work is motivated by the fact that there is lack of efficient numerical tools to model optical propagation in 3D waveguide structures, which are critical for the design of chip-scale photonic integrated circuits (PICs). A PIC is conceptually very similar to an electronic IC. While the latter integrates many transistors, capacitors, and resistors, a PIC integrates multiple optical components such as waveguides, filters, cavities, lasers, modulators, detectors, attenuators, multiplexers/de-multiplexers, optical amplifiers, etc... The primary application for PICs is in the area of telecom and datacom transmission systems [1].

There is a significant increase in high-bandwidth requirements for such transmission systems due to the rapid growth of the Internet. This leads to stringent performance demands on the light-wave transmission systems and their basic building blocks: the integrated and fiber-optic photonic components including fibers, lasers, detectors, modulators, switches and wavelength division multiplexing (WDM) devices. The development of novel device concepts towards more efficient communication systems has undoubtedly made demands for efficient computer simulation packages to aid the design and simulation of such photonic devices and systems. Especially techniques for finding modes and describing propagation attract tremendous attention and investment [2]. Such computer-aided design (CAD) tools must typically not only provide accurate vector results, or at least a reliable error estimate, but also be able to deal with multi-scale problems where intricate material properties and arbitrary geometries should be addressed properly [3].

In the past few years, a lot of numerical techniques for modeling guided-wave photonic devices have been developed such as the finite-difference time-domain (FDTD) method [4], the transmission line modeling (TLM) method [5], the method of lines (MoL) [6], the eigenmode expansion (EME) method [7], and the beam propagation method (BPM) [8]. Since exact methods including FDTD and TLM can be very time-consuming for some cases of huge waveguide components such as arrayed waveguide gratings (AWGs), approximate techniques such as BPM can be much faster [9]. An example of a typical A WG is shown in Fig. 1.1. Since it is very a big component to simulate completely with exact methods, it is advantageous to simulate several subparts of it separately. Very large unidirectional subparts can certainly benefit tremendously from fast approximate methods like BPM.

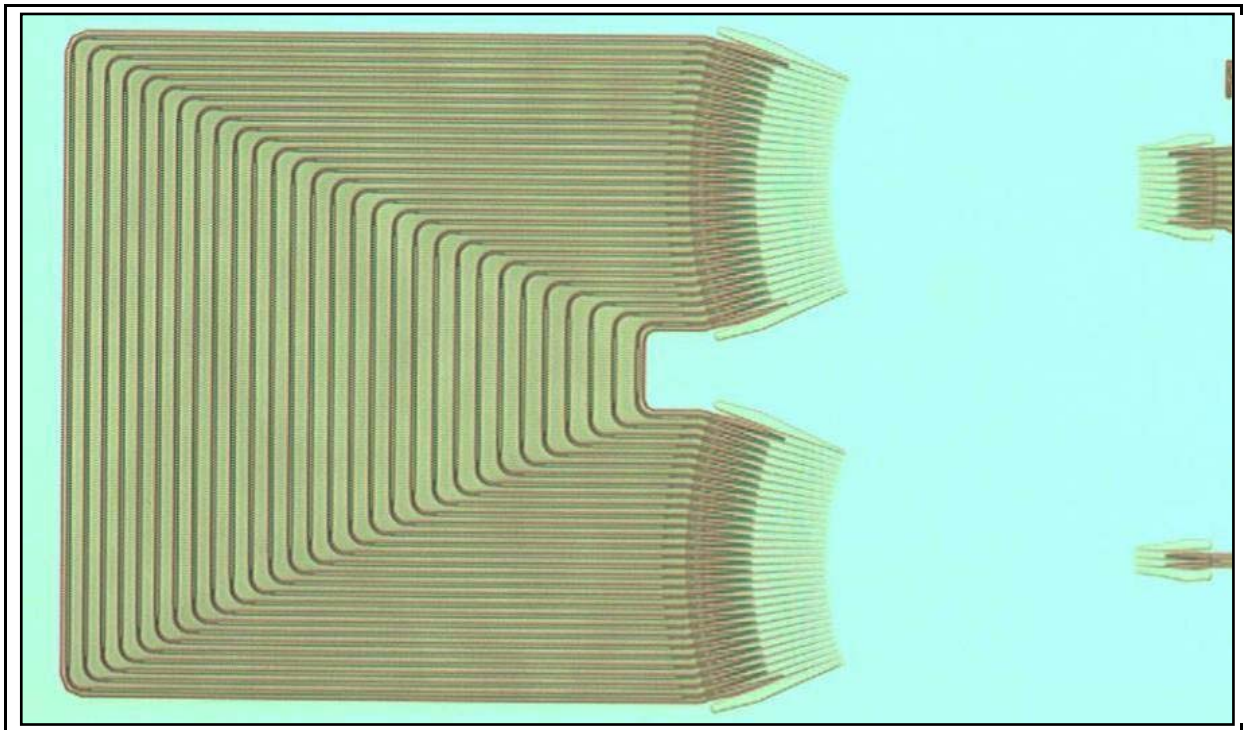


Figure 1.1. A typical arrayed waveguide grating on silicon-on-insulator platform.

In addition, the reason for the popularity of BPM for such a demanding problem is its straightforward and simple implementation. It results in less time-consuming and more efficient memory-usage than other methods even for large 3D practical problems. This conceptual simplicity also benefits users as well as implementers of a BPM-based tool, especially for non-experts in numerical methods [2]. In addition, it is readily applied to complex geometries without

having to develop specialized versions of the method and automatically includes the effects of both guided and radiating fields as well as mode coupling and conversion. Another characteristic of BPM is the fact that it is very flexible and extensible, allowing inclusion of most effects of interest including polarization and nonlinearities. This can be achieved by extensions of the basic method that fit within the same overall framework. The BPM has found numerous applications in modeling practical photonic devices and systems [2]. Several examples can be listed such as channel-dropping filters, electrooptic modulators, ring lasers, optical delay line circuits, optical interconnects, polarization splitters, multimode interference (MMI) devices, and AWGs as well. The Photonics Research Group, Ghent University aims at developing a powerful in-house tool called LightPy framework, an integrated tool for the design and simulation of Silicon photonics [10]. This work in this thesis is an integrated part of this framework, since we aim at developing fast and efficient BPMs for 3D optical waveguides which allow to simulate waves propagating in wide-angle structures. Especially our solvers for AWGs have been incorporated in this framework and are being used by other researchers.

By proposing novel approximant operators for the beam propagator, a number of efficient WA-BPMs have been developed in this project. Furthermore, the adaption of the recently introduced complex Jacobi iterative (CJI) method for 3D wide-angle beam propagation has been proposed and demonstrated as a very competitive tool for the design of guided-wave photonic devices.

The second part of this work is dedicated to looking at dielectric and plasmonic structures to enhance the performance of photonic devices by means of numerical and analytical approaches. The devices we have looked at are biosensors, light-emitting diodes (LEDs) and solar cells (SCs).

Biosensors have attracted tremendous interest in the last ten years due to their application in monitoring of diseases, and the detection of environment pollutants and biological agents. Biosensors are devices to measure the presence or concentration of biological molecules, biological structures, micro-organisms, etc., by translating a biochemical interaction at the probe surface into a quantifiable physical signal.

Better sensors aiming to detect biomolecules in a multi-parameter fashion are crucial for the further development of biotechnology and the total analysis of a biological system. There are

three main issues that require nanotechnology solutions: large-scale multi-parameter analysis, high sensitivity and the ability to get real time quantitative results. New sensors should have maximum sensitivity to allow measurements of biological samples with a high accuracy, high throughput, and in an array setup for multi-parameter analysis [11].

Nowadays, typical detection systems use antibodies that are labeled using radioactivity, enzymes or fluorescence. When such a labeled molecule binds to a surface, its presence can be detected using straightforward luminometry, fluorimetry, spectrometry, etc... While this technique is extremely sensitive with a detection limit down to a single molecule, it requires expensive and/or hazardous labeling procedures. Furthermore, labeling may change the reactivity of the labeled biomolecules which reduces both the qualitative and quantitative information of biological assays.

It is much better to have alternative elegant way to detect the presence of biomolecules directly without an intermediate labeling step. This results in label-free detection schemes. An example of a label-free optical biosensor is depicted in Fig. 1.2. A biomolecule binds to a chemically adapted surface containing detector groups. Since the target analytes have a different refractive index than the buffer solution (e.g. the refractive index of a protein is 1.5 vs 1.33 for buffer solution), this results in a refractive index change near the surface, which can be detected optically [11].

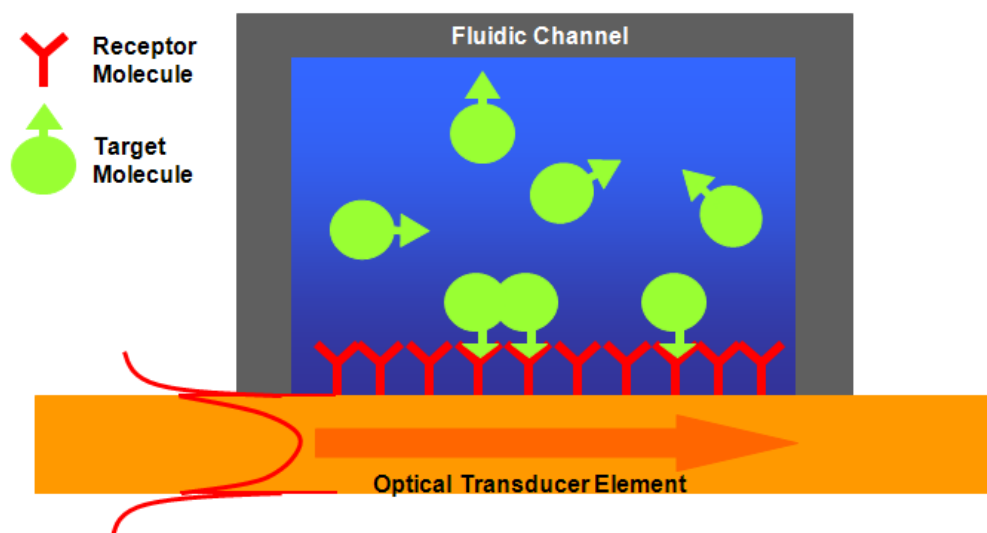


Figure 1.2. Schematical depiction of label-free biosensor. Source file from [11].

There is a number class of label-free optical biosensors such as surface plasmon resonance (SPR) biosensors, surface plasmon interference (SPI) biosensors, etc... Among those, the SPI sensor proposed in our group attracts much attention due to its miniaturization and parallelization. However, this device is itself very low sensitivity. In this work, we aim to improve the sensitivity of this sensor. This is obtained by making the sensing structure more symmetric.

A second class of devices we have optimised in this work are silicon LEDs. Silicon LEDs are very promising light sources due to their applications in optical communication technologies (see Fig. 1.3 for a typical silicon LED) [12]. Light emission from silicon has attracted tremendous interests in the past decades because of the ability to integrate such a device with silicon chips, which would add significant new functionalities to the modern photonic integrated circuits.

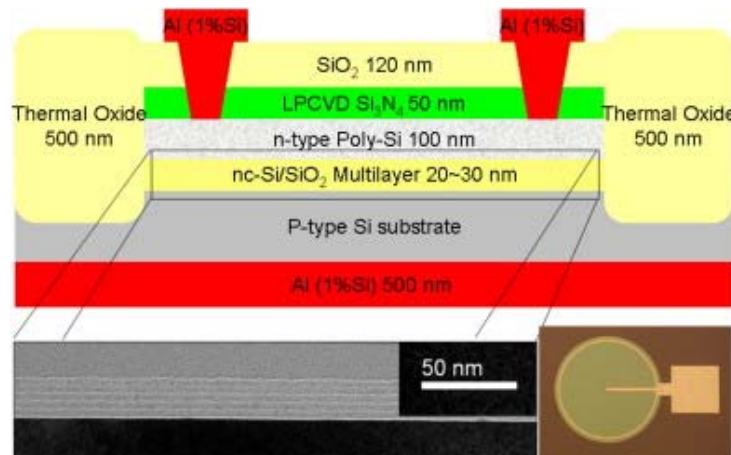


Figure 1.3. Schematical cross-section of LED structure (top), top view of the LED (bottom right) and TEM image (bottom left) of the nanocrystalline Si/SiO<sub>2</sub> multilayer structure. Source file from [12].

In addition, demands for increasing luminescence efficiency of silicon LEDs have also received growing interests. Efforts to improve silicon LEDs efficiency have so far made use of plasmonic nanostructures. Large efficiency enhancement of luminescence has been achieved by placing metal nanoparticles close to light emitters [13]. The enhancement is due to coupling between the electromagnetic excitations of the metallic nanoparticles and the waveguide modes. Formation of localized surface plasmons at resonance frequency results in high output enhancements of these LEDs. The properties of these resonances are determined by shape, size

and distribution of the nanoparticles. Therefore, an accurate theoretical model is very important in design of nanoparticle-enhanced light emitters. In this project, we have developed an improved model based on the effective mode volume theory to investigate the effect of metallic nanoparticles on light emission of silicon LEDs. The resulting model has explained experimental results better than previously published models.

A final class of devices we have studied in the second part of this thesis are photovoltaic devices. Photovoltaic (PV) devices (solar cells) are well-known as clean energy sources in future. They play a potential role to reform our energy system and reduce current problems associated with the use of fossil fuels [14]. Towards such a development we need to improve the light capturing ability of PV materials so that thinner layers can be used without compromising light absorption. This would reduce the cost of expensive PV materials, improve conditions for charge carrier collection and raise the efficiency.

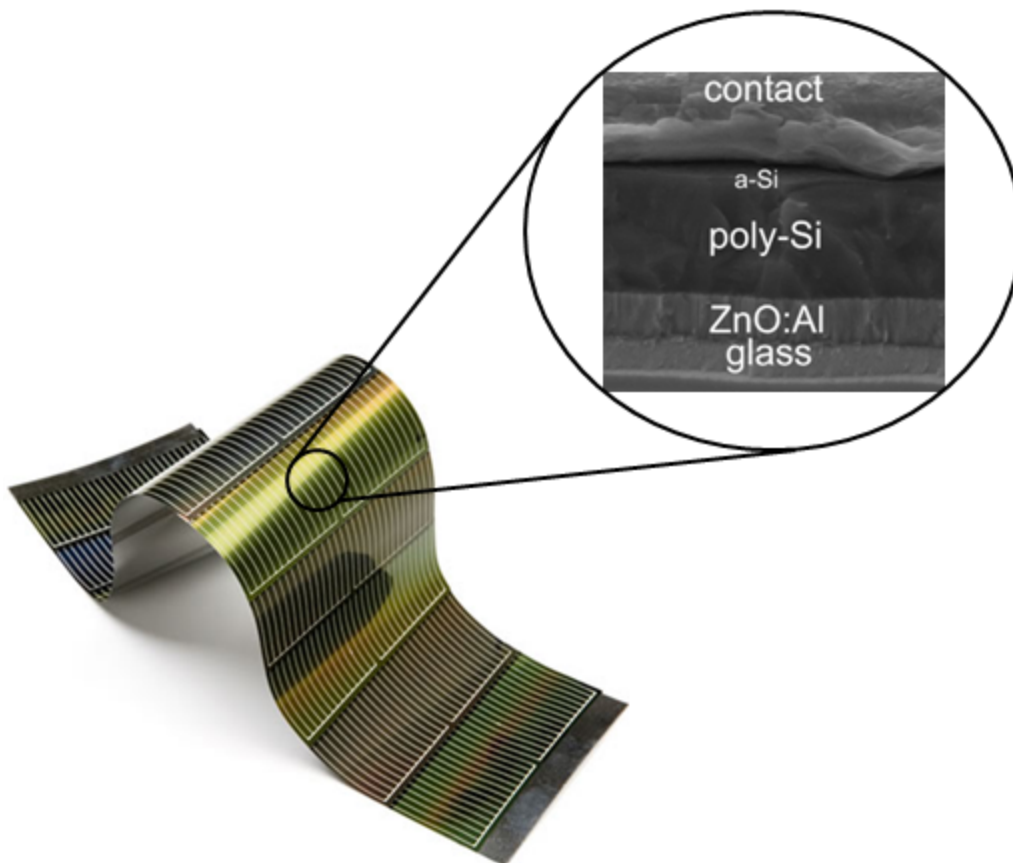


Figure 1.4. A thin-film silicon solar cell structure.

Silicon has been the material of choice for PV devices due to low cost, earth abundance, non-toxicity, and the availability of a very mature processing technology. To enable large-scale implementation, the cost of the current PV devices still needs to be significantly reduced and efficiency substantially increased. Thin-film silicon solar cells have shown to be promising candidates to provide a viable pathway towards this goal because of their low material and processing costs [15]. An example of a thin-film silicon solar cell is depicted in Fig. 1.4. Unfortunately, the low efficiency of these silicon PV devices has been hampering their development. Therefore, research to improve light absorption of PV devices has been attracting much attention. Many solutions for enhanced light absorption of PV cells have been proposed and demonstrated [16]. In this project, we have studied novel nanoscale structures to boost light absorption in active layer of thin-film amorphous silicon solar cells.

## I.2. Structure of this thesis

The rest of this thesis is structured as follows.

In chapter II, the beam propagation method (BPM) and its recent advances are reviewed. We focus on the important version of BPM for modeling waves propagating in wide-angle waveguide structures, the so-called wide-angle BPM (WA-BPM). More details of such a method based on conventional Padé approximant operators are also given in this chapter. Since conventional Padé operators have some limitations, we have addressed these issues and introduced a novel class of approximants. These are presented in chapter III. In chapter IV, we review several state-of-the-art solvers to implement beam propagation. The solvers we looked at are the generalized minimum residual (GMRES), bi-conjugate gradient stabilized (Bi-CGSTAB) method, and the recently introduced complex Jacobi iterative (CJI) method. The successive chapter is dedicated to presenting our adaptation of the CJI method for 3D WA-BPMs and benchmark results of these solvers is reported in this chapter as well.

Apart from beam propagation in uniform waveguides, we introduce a new approximate solution for wave propagation in graded-index metamaterials in chapter VI.

The next three chapters are used to present the study of improved performance of photonic devices. The devices we looked at are biosensors, LEDs and PV cells.

For biosensors, we have proposed to add an additional silicon layer on top of the sensor and an enhanced sensitivity has been obtained. The enhancement is due to the symmetry of the sensing structure we made. Details of this enhancement are discussed in chapter VII.

For LEDs, we have developed an improved model to investigate influences of metallic nanoparticles on light emission of light-emitters. Such a model is presented in chapter VIII.

Chapter IX is used to present the usefulness of a novel structure to enhance light absorption of thin-film amorphous silicon solar cells. Finally, we make a general summary of the project and give some outlooks.

### I.3. List of publications

The key achievements of our scientific research have been published in a number of peer-reviewed international journals and have been presented at several international and national conferences:

#### International journals

1. **Khai Q. Le**, A. Abass, B. Maes, P. Bienstman, *Plasmonic nanoantennas for absorption enhancement in thin-film amorphous Si solar cells*, in preparation.
2. **Khai Q. Le** and P. Bienstman, *Enhanced sensitivity of silicon-on-insulator surface plasmon interferometer with additional silicon layer*, accepted for publication on IEEE Photonics Journal.
3. **Khai Q. Le** and P. Bienstman, *Optical modeling of plasmonic nanoparticles enhanced light emission of silicon light-emitting diodes*, Plasmonics 6(1), p. 53-57 (2011).
4. **Khai Q. Le** and P. Bienstman, *Padé approximate solution for wave propagation in graded-index metamaterials*, Journal of Optics 13(2), p. 024015 (2010).
5. **Khai Q. Le** and P. Bienstman, *The complex Jacobi iterative method for non-paraxial beam propagation in nonlinear optical waveguides*, Optical and Quantum Electronics, 41(9), p. 705-709 (2010).
6. **Khai Q. Le** and P. Bienstman, *Three-dimensional higher-order Padé approximant-based wide-angle beam propagation method using complex Jacobi iteration*, Electronics Letters, 46(3), p.231-233 (2010) .

7. **Khai Q. Le** and P. Bienstman, *A stable complex Jacobi iterative solution of 3D semivectorial wide-angle beam propagation using the iterated Crank-Nicholson method*, *Optical and Quantum Electronics*, 41(215-221), (2009).
8. **Khai Q. Le**, Trevor Benson and P. Bienstman, *Application of modified Padé approximant operators to time-domain beam propagation methods*, *Journal of Optical Society of America B*, 26(12), p.2285-2289 (2009).
9. **Khai Q. Le** and P. Bienstman, *Fast three-dimensional generalized rectangular wide-angle BPM using complex Jacobi iteration*, *Journal of Optical Society of America B*, 26(7), p.1469-1472 (2009).
10. **Khai Q. Le**, *Complex Padé approximant operators for wide-angle beam propagation*, *Optics Communications*, 282(7), p.1252-1254 (2009).
11. **Khai Q. Le** and P. Bienstman, *Wide-angle beam propagation method without using slowly varying envelope approximation*, *Journal of Optical Society of America B*, 26(2), p.353-356 (2009).
12. **Khai Q. Le**, R. Godoy-Rubio, P. Bienstman and G. R. Hadley, *The complex Jacobi iterative method for three-dimensional wide-angle beam propagation: erratum*, *Optics Express*, 16(26), p.21942-21942 (2008).
13. **Khai Q. Le**, R. Godoy-Rubio, P. Bienstman and G. R. Hadley, *The complex Jacobi iterative method for three-dimensional wide-angle beam propagation*, *Optics Express*, 16(21), p.17021-17030 (2008).
14. **Khai Q. Le**, *Design of Type-II Interband Cascade Lasers for Terahertz Emission*, *Optical and Quantum Electronics*, 40(973-981), (2009).
15. **Khai Q. Le**, *Finite Element Analysis of Quantum States in Layered Quantum Semiconductor Structures with Band Nonparabolicity Effect*, *Microwave and Optical Technology Letters*, 51(1), p.1-5 (2008).
16. **Khai Q. Le** and Sangin Kim, *Model for Cross-plane Thermal Conductivity of Layered Quantum Semiconductor Structures and Application for Thermal Modeling of GaInAs/-AlInAs-based Quantum Cascade Lasers*, *Physica Status Solidi A*, 205(2), p.392 (2008).

## International conference proceedings

1. **Khai Q. Le**, A. Abass, B. Maes and P. Bienstman, *Plasmonic nanoantennas for absorption enhancement in thin-film silicon solar cells*, 3<sup>rd</sup> NANOMETA, Tirol, Austria (2011).
2. **Khai Q. Le** and P. Bienstman, *Nanoplasmonic resonator for biosensing applications*, 15<sup>th</sup> Annual Symposium of the IEEE Photonics Benelux Chapter, Deft, Netherlands (2010).

3. **Khai Q. Le**, A. Abass, B. Maes and P. Bienstman, *Analytical study of enhanced optical absorption of molecules near silver nanoparticles*, Optical Nanostructures for Photovoltaics, Germany (2010).
4. **Khai Q. Le** and P. Bienstman, *Enhanced Sensitivity of Absorption-Based Surface Plasmon Interference Sensors in Silicon-On-Insulator by Adsorbed Layer*, 15<sup>th</sup> European Conference on Integrated Optics, United Kingdom, (2010).
5. **Khai Q. Le**, B. Maes and P. Bienstman, *Numerical study of plasmonic nanoparticles enhanced light emission in silicon light-emitting-diodes*, 15th European Conference on Integrated Optics, United Kingdom (2010).
6. **Khai Q. Le**, Trevor Benson and P. Bienstman, *Modified Padé Approximant Operators for Efficient Time-Domain Beam Propagators*, 19th International Workshop on Optical Waveguide Theory and Numerical Modelling, United Kingdom, (2010).
7. **Khai Q. Le** and P. Bienstman, *Modeling the optical properties of metallic nanoparticles*, 14th Annual Symposium of the IEEE Photonics Benelux Chapter, Brussels, Belgium, p.217-220 (2009).
8. **Khai Q. Le**, Harshana G. Dantanarayana, Elena A. Romanova, Trevor Benson and P. Bienstman, *Comparative Assessment of Time-Domain Models of Nonlinear Optical Propagation*, 3rd ICTON-MW, France, (2009).
9. **Khai Q. Le** and P. Bienstman, *Non-paraxial beam propagation in nonlinear optical waveguides using complex Jacobi iteration*, 9th International Conference on Numerical Simulation of Optoelectronic Devices, South Korea, (2009) .
10. **Khai Q. Le**, P. Bienstman and G. R. Hadley, *Fast wide-angle BPMs using complex Jacobi iteration*, XVIII th International Workshop on Optical Waveguide Theory and Numerical Modelling, Germany, (2009).
11. **Khai Q. Le**, R. Godoy-Rubio and P. Bienstman, G. R. Hadley, *A three-dimensional non-paraxial beam propagation method using complex Jacobi iteration*, 13th Annual Symposium of the IEEE/LEOS Benelux Chapter, Netherlands, p.221 (2008).
12. **Khai Q. Le**, R. Godoy-Rubio and P. Bienstman, G. R. Hadley, *A Three-Dimensional Non-Paraxial Beam Propagation Method using Complex Jacobi Iteration*, International workshop on photonics and applications, Vietnam, (2008) .

## National conferences

1. **Khai Q. Le** and P. Bienstman, *Enhanced sensitivity of silicon-on-insulator surface plasmon interference biosensors with additional silicon top layer*, 11<sup>st</sup> FirW PhD symposium, Gent, Belgium (2010).
2. **Khai Q. Le** and P. Bienstman, *Modified Padé-Approximant-Based Wide-Angle Beam Propagators*, 10<sup>th</sup> FirW PhD symposium, Gent, Belgium (2009).

# References

1. Infinera Corporation, "Photonics integrated circuits: a technology and application primer," DS-008-001/0605 (2005).
2. R. Scarmozzino, A. Gopinath, R. Pregla, and S. Helfert, "Numerical techniques for modeling guided-wave photonic devices," *IEEE J. Sel. Top. Quantum Electron.* **6**, 150-161 (2000).
3. T. M. Benson, E. V. Bekker, A. Vukovic, and P. Sewell, "Challenges for integrated optics design and simulation," *Proc. of SPIE* **6769**, 67963C (2007).
4. S. T. Chu and S. Chaudhuri, "A finite-difference time-domain method for the design and analysis of guided wave optical structures," *J. Lightwave Technol.* **7**, 2033-2038 (1989).
5. C. Christopoulos, *The transmission-line modeling method: TLM*. Piscataway, NJ: IEEE Press, 1995.
6. U. Rogge and R. Pregla, "Method of lines for the analysis of dielectric waveguides," *J. Lightwave Technol.* **11**, 2015-2020 (1993).
7. P. Bienstman, and R. Baets, "Optical modelling of photonic crystals and VCSELs using eigenmode expansion and perfectly matched layers," *Opt. and Quantum Electron.* **33**, 327-341 (2001).
8. M. D. Feit and J. A. Fleck Jr., "Analysis of rib waveguides and couplers by the propagating beam method," *J. Opt. Soc. Am. A* **7**, 73-79 (1990).
9. S. Lidgate, "Advanced finite-difference beam propagation method analysis of complex components," PhD Thesis, GGIEMR, The University of Nottingham, 2004.
10. W. Bogaerts, P. Bradt, L. Vanholme, P. Bienstman, and R. Baets, "Closed-loop modeling of silicon nanophotonics from design to fabrication and back again," *Opt. and Quantum Electron.* **40**, 801-811 (2009).
11. P. Debackere, "Nanophotonic biosensor based on surface plasmon interference," PhD Thesis, Ghent University, 2010, pp. 4-22-4-36.
12. M. Wang, A. Anopchenko, A. Marconi, E. Moser, S. Prezioso, L. Pavesi, G. Pucker, P. Belluttin, and L. Vanzetti, "Light emitting devices based on nanocrystalline-silicon multilayer substrate," *Phys. E* **41**, 912-915 (2009).

13. S. Pillai, K. R. Catchpole, T. Trupke, G. Zhang, J. Zhao, and M. A. Green, "Enhanced emission from Si-based light-emitting diodes using surface plasmons," *Appl. Phys. Lett.* **88**, 161102 (2006).
14. C. Hagglund and B. Kasemo, "Nanoparticle plasmonics for 2D photovoltaics: mechanisms, optimization and limits," *Opt. Express* **17**, 11944-11957 (2009).
15. R. A. Pala, J. White, E. Barnard, J. Liu, and M. L. Brongersma, "Design of plasmonic thin-film solar cells with broadband absorption enhancements," *Adv. Mater.* **21**, 3504-3509 (2009).
16. H. A. Atwater and A. Polman, "Plasmonics for improved photovoltaic devices," *Nat. Mater.* **9**, 205-213 (2010).

# Chapter II

## The beam propagation method

In this chapter, we will present the beam propagation method (BPM) and its recent advances in both frequency and time domain. For frequency domain BPMs, we focus on the wide-angle version of BPM. For time-domain BPMs, we discuss two methods that enable waves propagating in reflective waveguides and ultrashort pulses propagating in wide-angle structures.

### II.1. Introduction

A simulation of the light wave propagation in an arbitrary medium can be done rigorously by a solution of Maxwell's equations. However, solving these equations directly is particularly difficult and finding the exact analytical solutions for wave propagation in guided-wave structures can be done only for a limited number of simple structures such as step-index slab waveguides and fibers. For more complicated structures, which cannot be solved analytically, numerical treatments may be feasible. For specific applications, a simplification of Maxwell's equation is needed to have an efficient and fast solution by numerical approaches. The well-known simplified version of Maxwell's equations with certain assumptions is the Helmholtz equation. This equation can be reformed for various applications [1]. In this section, the vectorial Helmholtz equation is derived directly from the Maxwell's equations.

Maxwell's equations in a homogeneous and lossless dielectric medium are given in terms of the electric field  $\vec{E}$  and magnetic field  $\vec{H}$  by [2]

$$\begin{aligned}\nabla \times \vec{E} &= -\mu \frac{\partial \vec{H}}{\partial t}, \\ \nabla \times \vec{H} &= \varepsilon \frac{\partial \vec{E}}{\partial t},\end{aligned}\tag{2.1}$$

with  $\varepsilon$  and  $\mu$  being the permittivity and permeability of the medium, respectively. For continuous waves with field having  $\exp(i\omega t)$  time dependence in linear and isotropic media, Eq. (2.1) can be written as:

$$\nabla \times \vec{E} = -i\omega\mu_0 \vec{H}, \quad (2.2a)$$

$$(2.2b)$$

$$\nabla \times \vec{H} = i\omega n^2 \varepsilon_0 \vec{E},$$

where  $\omega$  and  $n$  are an angular frequency and a refractive index of medium. In the following, we derive the vectorial wave equation for the electric field. Those for the magnetic field are similar. By taking the curl of Eq. (2.2a) and using Eq. (2.2b), we obtain the vectorial wave equation as follows:

$$\nabla \times \nabla \times \vec{E} - n^2 k^2 \vec{E} = 0, \quad (2.3)$$

with  $k$  being the wavenumber in vacuum. By using the vector identity, Eq. (2.3) can be rewritten by

$$\nabla^2 \vec{E} + n^2 k^2 \vec{E} = \nabla \left( \nabla \cdot \vec{E} \right). \quad (2.4)$$

If we consider the transverse components of an electric field, Eq. (2.4) is written by

$$\nabla_t^2 \vec{E}_t + n^2 k^2 \vec{E}_t = \nabla_t \left( \nabla_t \cdot \vec{E}_t + \frac{\partial E_z}{\partial z} \right), \quad (2.5)$$

where the subscript  $t$  stands for the transverse components. Using Gauss's law ( $\nabla \cdot (n^2 \vec{E}) = 0$ ), we obtain

$$\nabla_t \cdot \left( n^2 \vec{E}_t \right) + \frac{\partial n^2}{\partial z} E_z + n^2 \frac{\partial E_z}{\partial z} = 0. \quad (2.6)$$

If the refractive index  $n(x,y,z)$  varies slowly along the propagation direction ( $z$ -axis), then the second term is much smaller than the other two terms in Eq. (2.6). Thus we obtain the equation for  $z$ -invariant structures as follows:

$$\frac{\partial E_z}{\partial z} \approx -\frac{1}{n^2} \nabla_t \cdot \left( n^2 \vec{E}_t \right). \quad (2.7)$$

By substituting Eq. (2.7) into Eq. (2.5), we obtain the vectorial Helmholtz equation based on the transverse electric field

$$\nabla_t^2 \vec{E}_t + n^2 k^2 \vec{E}_t = \nabla_t \left[ \nabla_t \cdot \vec{E}_t - \frac{1}{n^2} \nabla_t \cdot \left( n^2 \vec{E}_t \right) \right]. \quad (2.8)$$

From this equation, different variants under certain assumptions and approximations can be given for specific applications. One of those is the beam propagation equation.

## II.2. Frequency-domain BPMs

For analysis of optical waveguides having nonuniform structures such as bends, tapers, and crosses in the propagation direction, the BPM is an excellent technique. Various kinds of BPMs including the fast Fourier transform (FFT-BPM) [3], the finite-difference (FD-BPM) [2], the Dirichlet-to-Neumann (DtN) maps-based BPM [4] and the finite-element (FE-BPM) [5] have been developed. In this project, however, attention is paid only to the FD-BPM due to its simplicity and accuracy.

### II.2.1. Scalar and paraxial BPMs

The formulation of the BPM is essentially based on an approximate solution of the exact wave equation for monochromatic waves. The resulting equations are numerically solved. Within an assumption of a scalar field where polarization effects are neglected, the wave equation Eq. (2.8) for monochromatic waves can be written in the form of the well-known scalar Helmholtz equation [2]:

$$\frac{\partial^2 \Psi}{\partial x^2} + \frac{\partial^2 \Psi}{\partial y^2} + \frac{\partial^2 \Psi}{\partial z^2} + k_0^2 n^2(x, y, z) \Psi = 0 \quad (2.9)$$

where  $n$  is the refractive index profile,  $k_0$  is the vacuum wavevector. For practical problems, it is best suited for low-index contrast waveguides. Here the scalar electric field is rewritten as  $E(x, y, z, t) = \Psi(x, y, z) \exp(-i\omega t)$  with  $\omega$  being the angular frequency.

Apart from the scalar assumption, Eq. (2.9) is the exact wave equation. For typical waveguide problems, it is considered that the most rapid variation in the field  $\Psi$  is the phase variation due to propagation along the guiding axis, and with an assumption of the predominant axis being the  $z$  direction this rapid variation can be factored out of the problem by using the slowly varying envelope approximation (SVEA). Then,  $\Psi(x, y, z)$  can be separated into two parts: the complex field amplitude  $\Phi(x, y, z)$  (the axially slowly varying envelope term) and the propagation factor  $\exp(ik_0 n_{ref} z)$  (the rapid varying phase term), and written as:

$$\Psi(x, y, z) = \Phi(x, y, z) \exp(ik_0 n_{ref} z) \quad (2.10)$$

where  $n_{ref}$  is referred to as the reference refractive index, which is a parameter that can be chosen by the user.

By substituting Eq. (2.10) into Eq. (2.9) and after slight rearrangement, the following relevant equation is obtained:

$$\frac{\partial \Phi}{\partial z} - \frac{i}{2k} \frac{\partial^2 \Phi}{\partial z^2} = \frac{iP}{2k} \Phi, \quad (2.11)$$

where  $P = \nabla_T^2 + k_0^2(n^2 - n_{ref}^2) = \frac{\partial^2}{\partial x^2} + \frac{\partial^2}{\partial y^2} + k_0^2(n^2 - n_{ref}^2)$  with  $k = k_0 n_{ref}$ . From this equation, various approximate solutions have been introduced. In the paraxial approximation where the propagation is restricted to a narrow range of angles the second order derivative  $\frac{\partial^2 \Phi}{\partial z^2}$  can be

neglected by assuming  $\left| i2k \frac{\partial \Phi}{\partial z} \right| \gg \left| \frac{\partial^2 \Phi}{\partial z^2} \right|$ . Then, the above equation reduces to

$$\frac{\partial \Phi}{\partial z} = \frac{iP}{2k} \Phi. \quad (2.12)$$

## II.2.2. Vectorial BPMs

In the above section, polarization effects were neglected. However, they can be included in the BPM by considering the electric field  $E$  to be a vector and starting the derivation of the beam propagation equation from the vector wave equation rather than the scalar Helmholtz equation. The resulting vector propagation equations that are formulated in terms of the transverse components of the field ( $E_x$  and  $E_y$ ) are given in the following set of coupled equations for the corresponding fields under the SVEA ( $\Phi_x$  and  $\Phi_y$ ):

$$\frac{\partial \Phi_x}{\partial z} = P_{xx} \Phi_x + P_{xy} \Phi_y \quad (2.13)$$

$$\frac{\partial \Phi_y}{\partial z} = P_{yx} \Phi_x + P_{yy} \Phi_y. \quad (2.14)$$

The  $P_{ij}$  are complex differential operators given by

$$P_{xx} \Phi_x = \frac{i}{2k} \left\{ \frac{\partial}{\partial x} \left[ \frac{1}{n^2} \frac{\partial}{\partial x} (n^2 \Phi_x) \right] + \frac{\partial^2}{\partial y^2} \Phi_x + k_0^2 (n^2 - n_{ref}^2) \Phi_x \right\}, \quad (2.15)$$

$$P_{yy} \Phi_y = \frac{i}{2k} \left\{ \frac{\partial^2}{\partial x^2} \Phi_y + \frac{\partial}{\partial y} \left[ \frac{1}{n^2} \frac{\partial}{\partial y} (n^2 \Phi_y) \right] + k_0^2 (n^2 - n_{ref}^2) \Phi_y \right\}, \quad (2.16)$$

$$P_{yx} \Phi_x = \frac{i}{2k} \left\{ \frac{\partial}{\partial y} \left[ \frac{1}{n^2} \frac{\partial}{\partial x} (n^2 \Phi_x) \right] - \frac{\partial^2}{\partial y \partial x} \Phi_x \right\}, \quad (2.17)$$

$$P_{xy} \Phi_y = \frac{i}{2k} \left\{ \frac{\partial}{\partial x} \left[ \frac{1}{n^2} \frac{\partial}{\partial y} (n^2 \Phi_y) \right] - \frac{\partial^2}{\partial x \partial y} \Phi_y \right\}. \quad (2.18)$$

The operators  $P_{xx}$  and  $P_{yy}$  take polarization effects into account due to different boundary conditions at interfaces and describe such effects as different polarization constants, field shape and bending loss, etc., for field components ( $\Phi_x$  and  $\Phi_y$ ). The off-diagonal terms  $P_{xy}$  and  $P_{yx}$  account the coupling between these components. With minor changes, these equations can also be used for the analysis of wave propagation in anisotropic materials whose refractive index is described by a diagonal matrix. The above equations are generally referred as the full-vectorial BPM. For simplification purposes, if the transverse field components are weakly coupled while retaining polarization effects, the coupling terms can be ignored ( $P_{xy}=P_{yx}=0$ ) and the so-called semivectorial BPM is then obtained.

### II.2.3. Wide-angle BPMs

The wide-angle or non-paraxial behaviour of BPMs enables propagation in wide range of angles, not only propagation along the z-axis. In contrast to the paraxial BPMs, the second order derivative  $\frac{\partial^2 \Phi}{\partial z^2}$  term is included in the wide-angle version. For the paraxial approximation or Fresnel equation used in BPM, this is usually accomplished by split-step methods, including the alternating-direction implicit (ADI) methods that are both fast and easy to implement [6]. However, the split-step schemes are only first-order-accurate in the step size, and a direct matrix inversion or iterative matrix solver is required for acceptable accuracy if wide-angle (WA) propagation is needed. Besides the limitation to paraxial beams, these methods also restrict the simulations to a low refractive index contrast ratio between the core and cladding of the waveguide. Efforts have been taken to relax both these limitations resulting in the so-called WA-BPMs. Different treatments of WA-BPMs based on the slowly varying envelope approximation (SVEA) have been developed by incorporating the effect of the second order derivative  $\frac{\partial^2 \Phi}{\partial z^2}$  term that was neglected in the paraxial BPM, including rational approximants of the square root operator [7], the exponential of the square root operator [8], and the Padé approximant operator [9], for rectangular coordinates as well as an oblique coordinate system [10]. In addition, treatments of WA-BPM without having to make use of the SVEA have also been reported, including the series expansion technique of the propagator [11], the rational approximation of the one way propagator [12] and the split-step of beam propagation equation [13-14]. Among those, the Padé-approximant-based WA-BPM is one of the most commonly used techniques for

modeling optical waveguide structures. Details of such Padé approximant operators will be presented in the next section.

## II.2.4. Conventional Padé approximant operators for WA-BPMs

Padé approximant operators, first introduced by Hadley in 1992 [9], have become one of the most widely used approximate techniques for the solution of WA beam propagation and most commercial BPM software packages have used them. One of the reasons for this popularity is attributed to the fact that apart from their high accuracy, they are simple and easy to implement. Their accuracy can be further increased by using higher order Padé operators. This can be easily implemented in the multistep method introduced by Hadley as well [15]. In addition, advanced boundary conditions have been successfully employed to avoid unexpected reflections from boundaries of a computational window so that the WA-BPM becomes more stable and reliable. The most significant advance in WA-BPMs is the slanted-wall beam propagation method. The method allows the modeling of an extremely wide variety of high-index-contrast waveguide structures with excellent phase accuracy and energy conservation.

### II.2.4.1. Padé approximant operators for wide-angle beam propagation

In this section, the formulation of the conventional Padé approximant operators is reviewed. The scalar Helmholtz equation (2.11) under the SVEA can be rewritten in the following form:

$$\frac{\partial \Phi}{\partial z} = i \frac{\frac{P}{2k}}{1 - \frac{i}{2k} \frac{\partial}{\partial z}} \Phi. \quad (2.19)$$

Eq. (2.19) suggests the recurrence relation

$$\left. \frac{\partial}{\partial z} \right|_{n+1} = i \frac{\frac{P}{2k}}{1 - \frac{i}{2k} \left. \frac{\partial}{\partial z} \right|_n}. \quad (2.20)$$

Hadley [9] proposed the rational approximation of WA beam propagation using Padé approximant operators with an initial value of  $\left. \frac{\partial}{\partial z} \right|_0 = 0$ . For  $\left. \frac{\partial}{\partial z} \right|_2$ , this gives us the well-known

Padé(1,1) approximant-based WA beam propagation formula as follows:

$$\frac{\partial H}{\partial z} \approx i \frac{\frac{P}{2k}}{1 + \frac{P}{4k^2}} H. \quad (2.21)$$

The most useful low-order Padé approximant operators are shown in table 2.1. If Eq. (2.21) is compared with a formal solution of Eq. (2.11) written in the well-known form

$$\frac{\partial H}{\partial z} = i(\sqrt{P+k^2} - k)H = ik(\sqrt{1+X} - 1)H, \quad (2.22)$$

where  $X = \frac{P}{k^2}$ , the following approximation formula is obtained:

$$\sqrt{1+X} - 1 \approx \frac{\frac{P}{2k^2}}{1 + \frac{P}{4k^2}} = \frac{\frac{X}{2}}{1 + \frac{X}{4}}. \quad (2.23)$$

Since the operator  $X$  has a real spectrum, it is useful to consider the approximation of  $\sqrt{1+X} - 1$  by the Padé approximant propagation operator. Figure 2.1 shows the absolute value of  $\sqrt{1+X} - 1$  and its first-order Padé(1,1) approximant as a function of  $X$ . The same figure shows higher order of Padé approximant operators. It is seen that a good agreement between the approximate results and the exact one is obtained in certain range of  $X$ . The higher the order of Padé operators, the more accurate the approximation will be.

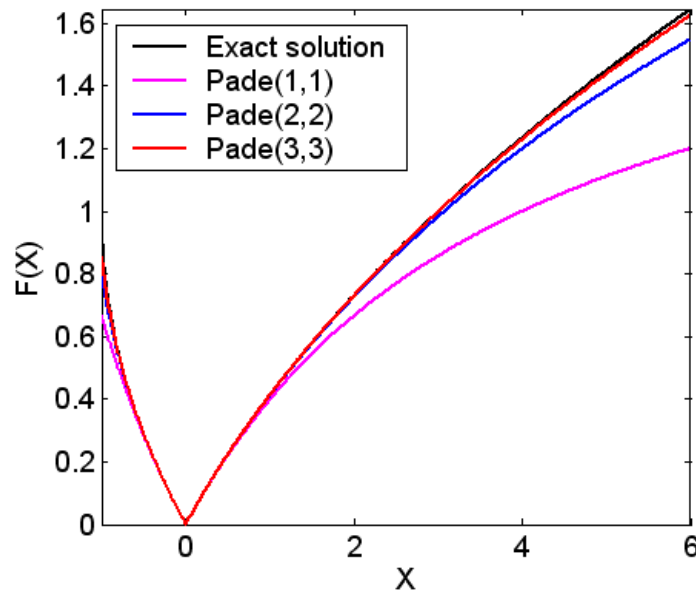


Figure 2.1: The absolute values of  $F(X) = (1+X)^{1/2} - 1$  and the most useful low-order Padé approximants of  $(1+X)^{1/2} - 1$ .

Table 2.1

Most useful low-order Padé approximants of  $\sqrt{1+X} - 1$  in terms of the operator  $X$

Order	Expression
(1,0)	$\frac{X}{2}$
(1,1)	$\frac{X}{2} \frac{X}{1 + \frac{X}{4}}$
(2,2)	$\frac{\frac{X}{2} + \frac{X^2}{4}}{1 + \frac{3X}{4} + \frac{X^2}{16}}$
(3,3)	$\frac{\frac{X}{2} + \frac{X^2}{2} + \frac{3X^3}{32}}{1 + \frac{5X}{4} + \frac{3X^2}{8} + \frac{X^3}{64}}$

### II.2.4.2. Multistep solution for WA beam propagation

It is seen that a numerical solution of Padé(1,1)-based WA beam propagation is relatively easy. However, for higher order Padé-based approximants, it is very challenging to perform WA propagation in a straightforward way. For this purpose, the multistep method has been proposed.

From the recurrence relation (2.20), the formulation of various orders of Padé operators can be established from the initial value of 0. For simplification purpose, Eq. (2.20) can be described by an approximate expression containing only the operator  $P$  and the useful propagator is given as follows:

$$\frac{\partial \Phi}{\partial z} = \frac{iN}{D} \Phi, \quad (2.24)$$

where  $N$  and  $D$  are polynomials in  $P$ .

If Eq. (2.24) is discretized using standard centered differencing, it is given by:

$$D(\Phi^{m+1} - \Phi^m) = \frac{i\Delta z}{2} N(\Phi^{m+1} + \Phi^m), \quad (2.25)$$

where the subscript indicates position along the propagation direction ( $z$ -axis). Then, the above equation may be recast in the following form:

$$\Phi^{m+1} = \frac{\sum_{i=0}^w \xi_i P^i}{\sum_{i=0}^w \xi_i^* P^i} \Phi^m, \quad (2.26)$$

where  $\xi_0 = P^0 = 1$ ,  $w$  is the order of Padé operators and the other  $\xi$ 's are determined from the coefficients of the polynomial  $N$  and  $D$ . Since a polynomial of degree  $w$  can always be factored in terms of its  $w$  roots, Eq. (2.26) can be rewritten as:

$$\Phi^{m+1} = \frac{(1 + a_1 P)(1 + a_2 P) \dots (1 + a_w P)}{(1 + a_1^* P)(1 + a_2^* P) \dots (1 + a_w^* P)} \Phi^m, \quad (2.27)$$

From Eq. (2.27), a  $w^{\text{th}}$  order Padé propagator can be decomposed into a  $w$ -step algorithm for which the  $i^{\text{th}}$  partial step is given by the following form:

$$\Phi^{m+\frac{i}{w}} = \frac{(1 + a_i P)}{(1 + a_i^* P)} \Phi^{m+\frac{i-1}{w}}. \quad (2.28)$$

It has been shown that the resulting multistep algorithm is fast and unconditionally stable. The run time for each step is the same as the run time for the paraxial propagation [15].

### II.2.4.3. Boundary conditions for WA-BPMs

Since propagation problems are normally performed in a finite computational domain, reflections from the edge of boundaries going back to the computational domain may lead to spurious solutions. Several boundary conditions have been proposed to absorb such unexpected reflected waves and this section is used to review such advanced boundary conditions.

One of the most traditional ways is the use of artificial absorbing materials near the edge of the domain. However, adjusting the parameters of the absorber to minimize reflection is cumbersome, and artificial reflections still remain in many cases since the interface between the problem space and the absorber will also be partially reflected [16]. Efforts to get rid of such reflections and avoid using of extra artificial absorbing materials have been done. One of the most widely used boundary conditions for WA-BPMs is the transparent boundary condition (TBC), also introduced by Hadley [17-18]. The basic idea of such a technique is to assume that near the boundary the field plays the role of an outgoing plane wave. The TBC is generally very effective in allowing radiation to freely escape and avoiding reflection back into the computational domain.

In addition, several other absorbing boundary conditions have been proposed for WA-BPMs. These include the highly efficient absorbing boundary condition introduced by Vassalo *et al.*

[19], the perfectly matched layer (PML) [20], and complementary operators as the absorbing boundary condition [21]. For details of a performance comparison between these boundary conditions, we refer the reader to Refs. [19,22] for further information.

#### **II.2.4.4. Slanted-wall beam propagation using the Padé(1,1) operator**

In the previous sections, significant advances in many aspects of the BPM have been briefly reviewed, including the extension to wide-angle propagation, the use of advanced boundary conditions, and the inclusion of vector components. However, most of these contributions involve formulations that assume all dielectric boundaries to be along planes that never intersect the propagation axis (z-axis). It means that the waveguide cross-section is assumed to be independent of the propagation direction. In general, to investigate waves propagating in a waveguide where its cross section varies along the propagation direction, the so-called stair-case approximation has been used to describe the refractive index profile. In this approximation, slanted or curved structures have been modeled by a series of sudden (but slight) modifications in cross section that approximate the real waveguide walls. However, this leads to the generation of artificial mode-mixing and numerical loss at each transition point that is not characteristic of the structure being modeled [23]. These spurious effects are generally tolerable for low-index-contrast structures, but can be serious for high-index-contrast structures. An example of the inaccuracy of the standard stair-case method for high-index-contrast waveguides is shown in Fig. 2.2. The waveguide path was made up four circular arcs of  $10^\circ$  extent and 1800- $\mu\text{m}$  radius joined smoothly. The TE fundamental mode of a waveguide of width 1.2  $\mu\text{m}$  with core and cladding indices of 1.98 and 1.448 at wavelength 1.55  $\mu\text{m}$  was launched into the waveguide at the bottom of the figure and propagated through the structure [23]. As seen in the figure, the sudden changes in dielectric constant resulting from the stair-stepping procedure have generated nonphysical ripples in the waveform and have led to a spurious radiation loss of up to 25%.

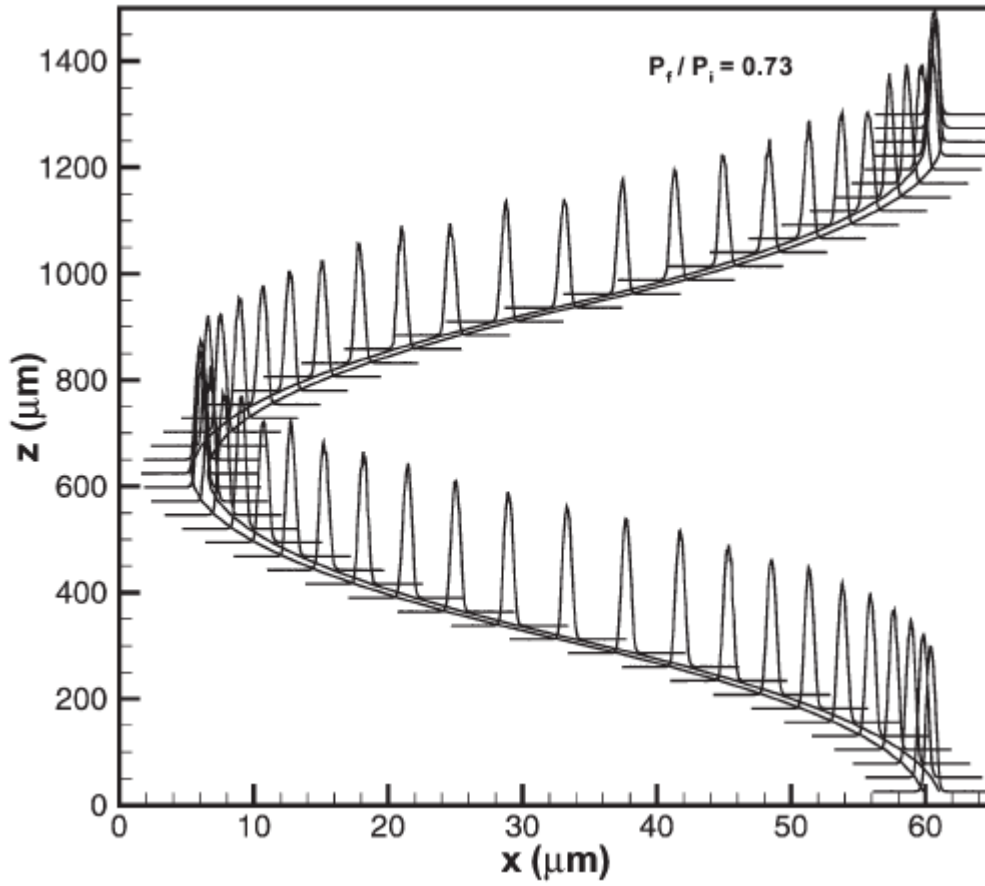


Figure 2.2: Intensity profiles along a moving waveguide calculated by the standard wide-angle beam propagation method using a fixed grid. Source file from [23].

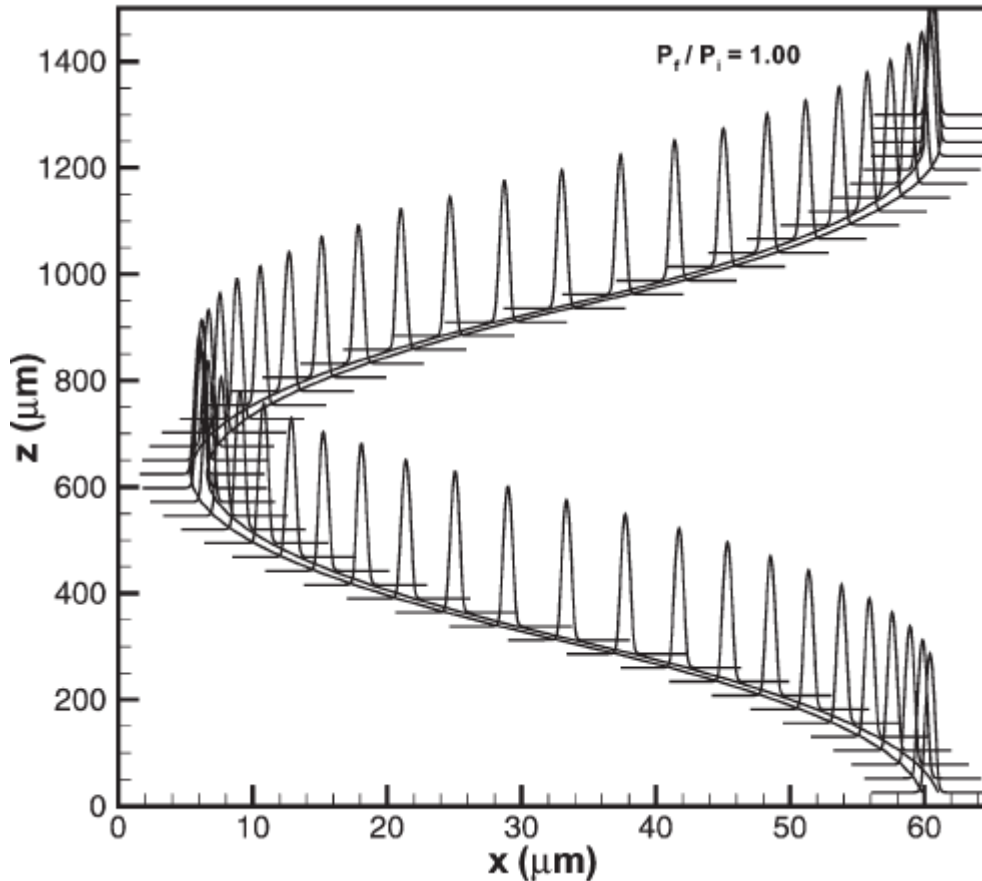


Figure 2.3: Propagation for same problem in Fig. 2.2 but using the slanted-wall algorithm. Source file from [23].

Several works have been performed to address this issue. Among those are the use of coordinate transformations, either to tapered [24] or oblique [25-27] coordinates, some combination of these [28] or a more general nonorthogonal coordinate system [29-30]. The form of the coordinate transformation is generally accurate for structures of sufficient regularity that can be described in a transformed coordinate system using simple differentiable functions. This approach has been successfully applied to model curved waveguide couplers [30]. However, its use requires the construction of an analytic function describing the waveguide structure, together with its derivatives. Thus, the simulation of certain classes of irregular structures requires a significant expenditure of effort in finding a suitable solution. In addition, grid-size dependence on propagation distance is specified by the same function that defines the structure. This is sometimes a benefit but can also be a disadvantage for the cases of expanding or collapsing waveguide structures, and the insertion or deletion of grid points may require an interpolation [23].

To circumvent this problem, the slanted-wall beam propagation method has been developed [23]. It provides a general finite-difference algorithm that can be able to model structures with slanted walls without resorting to stair-case approximations or no coordinate transformations being employed. It allows each grid point to move from one plane to the next in a manner that is arbitrary and independent of other grid points so that definition of the structure as well as the grid resolution is arbitrary and uncoupled. Furthermore, the insertion or deletion of grid points can be done inside the algorithm without the need for interpolation. Figure 2.3 shows the corresponding profiles of the waveguide in Fig. 2.2 but this time for the slanted-wall method. In contrast to the previous case, all profiles are smooth and uniform. No radiation loss was predicted.

The formulation of slanted-wall wide-angle beam propagation is based on the simplest Padé(1,1) approximant operator but the resulting algorithm is very impressive, particularly for those interested in curved waveguide structures. The method allows the modeling of an extremely wide variety of high-index-contrast waveguide structures with excellent phase accuracy and energy conservation. For simplification purposes, details of the derivation of the algorithm are not presented in this thesis. They can be easily found in Ref. [23].

### **II.3. Time-domain BPMs**

While WA-BPMs are popular for the study of forward propagating waves in longitudinally varying optical waveguide devices, they can never be extended to handle simultaneous backward propagating waves. This can be done only by treating the backward traveling waves as a separate, though coupled, part of the problem in frequency-domain BPMs. Various bidirectional BPM (Bi-BPM) techniques have been developed to address this issue with most focusing on the coupling that occurs via reflection of a wave incident on an interface along the propagation direction [31-32]. However, one can handle simultaneously both forward and backward propagating waves in reflective waveguide structures by introducing time-domain BPMs [33-34]. Such methods can also be adapted to model effectively ultrashort pulses propagating in wide-angle structures [35].

The formulation of time-domain BPMs is done by considering a two-dimensional (2D) scalar wave equation where the computational domain is on the  $xz$ -plane [36]:

$$\frac{\partial^2 \Psi}{\partial z^2} + \frac{\partial^2 \Psi}{\partial x^2} = \frac{n^2}{c^2} \frac{\partial^2 \Psi}{\partial t^2}. \quad (2.29)$$

where  $n$  is a refractive index profile and  $c$  is the speed of light in free space. This equation can be used as a starting point for two different models: dealing with reflected waves and modeling of ultrashort pulse propagation in wide-angle structures.

### II.3.1. Time-domain BPMs for treating reflected waves

The formal solution of Eq. (2.29) with a slowly varying complex amplitude is given by

$$\Psi(x, z, t) = \psi(x, z, t) \exp(i\omega_0 t). \quad (2.30)$$

(It is obviously seen that only waves propagating forward in time are considered; the method is still fully reflective since no approximation is made in the propagation direction). By substituting Eq. (2.30) into Eq. (2.29), the following equation is obtained

$$\frac{\partial^2 \psi}{\partial t^2} + 2i\omega_0 \frac{\partial \psi}{\partial t} = P \psi, \quad (2.31)$$

where  $P = \frac{c^2}{n^2} \left( \frac{\partial^2}{\partial x^2} + \frac{\partial^2}{\partial z^2} \right) + \omega_0^2$  and  $\omega_0$  is the center angular frequency. The solution of Eq.

(2.31) gives us transmission and reflection properties of waves propagating in reflective structures.

### II.3.2. Time-domain BPMs for modeling ultrashort pulses in wide-angle structures

Apart from being successful in treating reflected waves, these time-domain BPMs have also found a wide-range application in the analysis of ultrashort pulses propagating in wide-angle waveguides. To do so, the formal solution of the time domain wave equation is rewritten under the slowly varying envelope approximation as follows [35]:

$$\Psi(x, z, t) = \psi(x, z, t) \exp(ikz) \exp(i\omega_0 t), \quad (2.32)$$

with  $k = k_0 n_{ref}$ ,  $n_{ref}$  the reference refractive index,  $k_0$  the vacuum wavevector. Here, only waves that are propagating forward in space are retained.

By substituting Eq. (2.32) into Eq. (2.29), the following equation is obtained

$$\frac{\partial^2 \psi}{\partial z^2} + 2ik \frac{\partial \psi}{\partial z} + \frac{\partial^2 \psi}{\partial x^2} - \frac{n^2}{c^2} \left( \frac{\partial^2 \psi}{\partial t^2} + 2i\omega_0 \frac{\partial \psi}{\partial t} \right) + k_0^2 (n^2 - n_{ref}^2) \psi = 0 \quad (2.33)$$

In order to calculate this efficiently, a moving time window is needed. Since a pulse will eventually disappear from the window after a certain number of propagation steps, the computational window should move along with the pulse at the group velocity of the pulse envelope. Therefore, a moving time coordinate  $\tau = t - v_g^{-1}z$  with arbitrary  $v_g$  should be used and Eq. (2.33) can be expressed in the following form [35]:

$$\frac{\partial^2 \psi}{\partial z^2} + 2ik \frac{\partial \psi}{\partial z} = Q \psi, \quad (2.34)$$

with  $Q = \frac{n^2}{c^2} \frac{\partial^2}{\partial \tau^2} + 2ik_0 n^2 \left( \frac{1}{c} - \frac{1}{v_g} \right) \frac{\partial \psi}{\partial \tau} - \frac{\partial^2}{\partial x^2} - k_0^2 (n^2 - n_{ref}^2)$  and  $k_0 = \omega_0/c$ . It is easy to see that Eq.

(2.34) is in the same form as Eq. (2.31). Such an equation is the well-known wide-angle propagation equation for which a lot of solution techniques have been developed.

## II.4. Conclusion

In this chapter, various versions of the beam propagation method have been briefly reviewed. The focus is on the wide-angle beam propagation methods and the time-domain beam propagation methods. The development of such beam propagation methods in this project has been carried out by the improvement of those based on conventional Padé approximant operators. In addition, the well-known multistep algorithm for dealing with higher order Padé operators based WA-BPMs associated with advanced boundary conditions have been reviewed. The significant advance is dedicated to the version of WA-BPMs for treating slanted waveguides based on the simplest Padé(1,1) operator. Apart from the widespread use of conventional Padé operators based WA-BPMs, there still remain some limitations. This will be addressed in the next chapter.

# References

1. C. L. Xu, and W. P. Huang, "Finite-difference beam propagation method for guided-wave optics," *Progress in Electromagnetics Research, PIER* **11**, 1-49 (1995).
2. K. Okamoto, *Fundamentals of optical waveguides*, (Elsevier, MA, USA, 2006).
3. M. D. Feit, and J. A. Fleck Jr., "Light propagation in graded-index optical fibers," *App. Opt.* **17**, 3990-3998 (1978).
4. L. Yuan, and Y. Y. Lu, "An efficient bidirectional beam propagation method based on Dirichlet-to-Neumann maps," *IEEE Photon. Technol. Lett.* **18**, 1967-1969 (2006).
5. Y. Tsuji, and M. Koshiba, "A finite element beam propagation method for strongly guiding and longitudinally varying optical waveguides," *J. Lightwave Technol.* **14**, 217-222 (1996).
6. W. H. Press, B. P. Flannery, S. A. Teukolsky, and W. T. Vetterling, *Numerical recipes: The art of scientific computing*, (Cambridge University Press, New York, 1986).
7. F. A. Milinazzo, C. A. Zala, and G. H. Brooke, "Rational square root approximations for parabolic equation algorithms," *J. Acoust. Soc. Amer.* **101**, 760-766 (1997).
8. T. Anada, T. Hokazono, T. Hiraoka, J. P. Hsu, T. M. Benson, and P. Sewell, "Very-wide-angle beam propagation methods for integrated optical circuits," *IEICE Trans. Electron.* **E82-C**, 1154-1158 (1999).
9. G. R. Hadley, "Wide-angle beam propagation using Padé approximant operators," *Opt. Lett.* **17**, 1426-1428 (1992).
10. S. Sujecki, "Wide-angle, finite-difference beam propagation in oblique coordinate system," *J. Opt. Soc. Am. A* **25**, 138-145 (2007).
11. P. C. Lee and E. Voges, "Three-dimensional semi-vectorial wide-angle beam propagation method," *J. Lightwave Technol.* **12**, 215-225, (1994).
12. Y. Y. Lu and P. L. Ho, "Beam propagation method using a  $[(p-1)/p]$  Padé approximant of the propagator," *Opt. Lett.* **27**, 683-685 (2002).
13. A. Sharma and A. Agrawal, "New method for nonparaxial beam propagation," *J. Opt. Soc. Am. A* **21**, 1082-1087 (2004).
14. A. Sharma and A. Agrawal, "A new finite-difference-based method for wide-angle beam propagation," *IEEE Photonics Tech. Lett.* **18**, 944-946 (2006).

15. G. R. Hadley, "Multistep method for wide-angle beam propagation," *Opt. Lett.* **17**, 1743-1745 (1992).
16. R. Scarmozzino, A. Gopinath, R. Pregla, and S. Helfert, "Numerical techniques for modeling guided-wave photonic devices," *IEEE J. Sel. Top. Quantum Electron.* **6**, 150-161 (2000).
17. G. R. Hadley, "Transparent boundary condition for the beam propagation method," *Opt. Lett.* **28**, 624-626 (1992).
18. G. R. Hadley, "Transparent boundary condition for the beam propagation method," *J. Quantum Electron.* **28**, 363-370 (1992).
19. C. Vassalo and F. Collino, "Highly efficient absorbing boundary condition for the beam propagation method," *J. Lightwave Technol.* **14**, 1570-1577 (1996).
20. W. P. Huang, C. L. Xu, W. Lui, and K. Yokoyama, "The perfectly matched layer (PML) boundary condition for the beam propagation method," *Photon. Technol. Lett.* **8**, 649-651 (1996).
21. Y. P. Chiou and H. C. Chang, "Complementary operators method as the absorbing boundary condition for the beam propagation method," *Photon. Technol. Lett.* **8**, 976-979 (1998).
22. D. Jimenez and F. Perez-Murano, "Comparison of highly absorbing boundary conditions for the beam propagation method," *J. Opt. Soc. Am. A* **18**, 2015-2025 (2001).
23. G. R. Hadley, "Slanted-wall beam propagation," *J. Lightwave Technol.* **25**, 2367-2375 (2007).
24. P. Sewell, T. M. Benson, P. C. Kendall, and T. Anada, "Tapered beam propagation," *Electron. Lett.* **32**, 1025-1026 (1996).
25. J. Yamauchi, J. Shibayama, and H. Nakano, "Finite-difference beam propagation method using the oblique coordinate system," *Electron. Commun. Jpn.* **78**, 20-27 (1995).
26. P. Sewell, T. M. Benson, T. Anada, and P. C. Kendall, "Bi-oblique propagation analysis of symmetric and asymmetric Y-junctions," *J. Lightwave Technol.* **15**, 688-696 (1997).
27. Y.-P. Chiou and H.-C. Chang, "Beam propagation method for analysis of z-dependent structures that uses a local oblique coordinate system," *Opt. Lett.* **23**, 998-1000 (1998).

28. S. Sujecki, P. Sewell, T. M. Benson, and P. C. Kendall, "Novel beam propagation algorithms for tapered optical structures," *J. Lightwave Technol.* **17**, 2379–2388 (1999).
29. T. M. Benson, P. Sewell, S. Sujecki, and P. C. Kendall, "Structure related beam propagation," *Opt. Quantum Electron.* **31**, 689–703 (1999).
30. D. Z. Djurdjevic, T. M. Benson, P. Sewell, and A. Vukovic, "Fast and accurate analysis of 3-D curved optical waveguide couplers," *J. Lightwave Technol.* **22**, 2333–2340 (2004).
31. P. Kaczmariski and P. E. Lagasse, "Bidirectional beam propagation method," *Electron. Lett.* **24**, 675–676 (1988).
32. H. Rao, R. Scarmozzino, and R. M. Osgood Jr., "A bidirectional beam propagation method for multiple dielectric interfaces," *Photon. Technol. Lett.* **11**, 830–832 (1999).
33. R. Y. Chan and J. M. Liu, "Time-domain wave propagation in optical structures," *IEEE Photon. Technol. Lett.* **6**, 1001-1003 (1994).
34. M. Koshiba, J. Tsuji and M. Kikari, "Time-domain beam propagation method and its application to photonic crystal circuits," *J. Lightwave Technol.* **18**, 102-110 (2000).
35. H. M. Masoudi, "A novel nonparaxial time-domain beam propagation method for modeling ultrashort pulses in optical structures," *J. Lightwave Technol.* **25**, 1-10 (2007).
36. T. Fujisawa and M. Koshiba, "Time-domain beam propagation method for nonlinear optical propagation analysis and its application to photonic crystal circuits," *J. Lightwave Technol.* **22**, 684-691 (2004).

# Chapter III

## New Padé approximant operators for WA-BPMs

In this chapter, two novel approximant methods developed for WA-BPMs will be presented. The first one is called the modified Padé approximant method. The second one is called the KP approximant method, which can be used for WA-BPM without having to make the slowly varying envelope approximation. We will first address the limitation of conventional Padé operators and then introduce our modified operators. The sections after that are used to present the generalized rectangular WA-BPMs using these new modified operators and to demonstrate the usefulness of these operators for time-domain BPMs, respectively. Then, we present a comparative assessment of time-domain models for nonlinear optical propagation. This work was done in collaboration with Trevor Benson's group in the University of Nottingham. Finally, we introduce the KP approximant method for WA-BPMs.

### III.1. Modified Padé approximant operators

The introduction of the slanted-wall beam propagation using the Padé(1,1) approximant operator has undoubtedly benefited the community that is working on design and simulation of guided-wave photonic devices. The widespread use of such a powerful tool again shows the advantage of using Padé approximant operators. However, there is still a significant remaining issue for Padé operators that needs to be overcome since they fail to address evanescent modes. Indeed, it can be seen that as the denominator of Padé approximant operators gradually approaches zero, its absolute value approaches  $\infty$  as shown in Fig. 3.1. Physically this means that the standard Padé operators incorrectly propagate the evanescent modes. To circumvent this problem, we proposed modified Padé approximant operators [1], which are a key novel result of the first part of this dissertation.

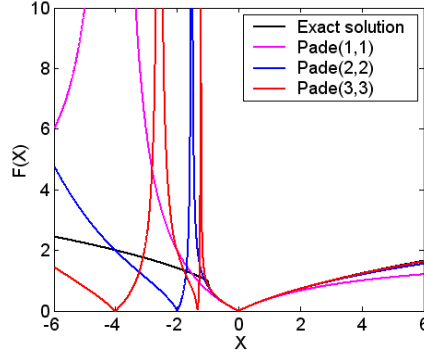


Figure 3.1: The absolute values of  $F(X) = (1+X)^{1/2}-1$  and the most useful low-order Padé approximants of  $(1+X)^{1/2}-1$ .

### III.1.1. Formulation

First of all, following [2], by multiplying both sides of Eq. (2.19) with  $-\frac{i}{k}$ , we obtain:

$$-\frac{i}{k} \frac{\partial}{\partial z} = \frac{\frac{P}{k^2}}{2 - \frac{i}{k} \frac{\partial}{\partial z}}. \quad (3.1)$$

Eq. (3.1) can be rewritten as follows

$$f(X) = \frac{X}{2 + f(X)}, \quad (3.2)$$

where  $f(X) = -\frac{i}{k} \frac{\partial}{\partial z}$ . Eq. (3.2) suggests the recurrence relation

$$f_{n+1}(X) = \frac{X}{2 + f_n(X)} \quad \text{for } n=0,1,2,\dots \quad (3.3)$$

Y. Y. Lu [2] has proved that Eq. (3.3) can provide a good approximation to  $\sqrt{1+X} - 1$  with the initial value of

$$f_0(X) = i\beta \quad \text{where } \beta > 0. \quad (3.4)$$

Subsequently, we use this fact to go back to the original recurrence relation (2.20) and construct modified Padé approximant operators by using a different initial value of  $\left. \frac{\partial}{\partial z} \right|_0 = -k\beta$ .

For  $\left. \frac{\partial}{\partial z} \right|_2$ , the first-order modified Padé(1,1) approximant operator is given as follows:

$$\frac{\partial \Phi}{\partial z} \approx i \frac{\frac{P}{2k}}{1 + \frac{P}{4k^2(1 + \frac{i\beta}{2})}} \Phi. \quad (3.5)$$

The most useful low-order modified Padé approximant operators are shown in table 3.1. The absolute value of the standard and modified Padé(1,1) approximant of  $\sqrt{1+X} - 1$  are depicted in Fig. 3.2. It is seen that the modified Padé approximant operator (with  $\beta = 2$ ) allows more accurate approximations to the true Helmholtz equation than the standard Padé approximant operator. Furthermore, the standard rational Padé approximant operators incorrectly propagate the evanescent modes as their denominator gradually approaches zero while the modified Padé approximant operators give the waves propagating in the evanescent region the desired damping as clearly seen in Fig. 3.3.

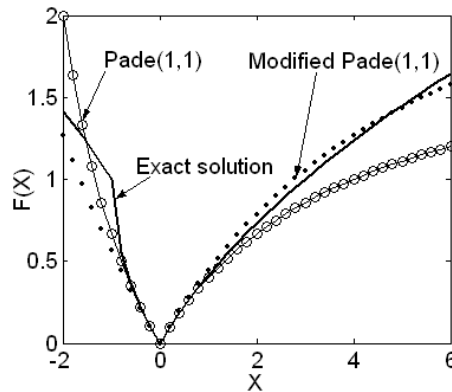


Figure 3.2. The absolute values of  $(1+X)^{1/2}-1$  (solid line), its first-order standard Padé approximant (solid line with circles) and modified Padé approximant (dotted line).

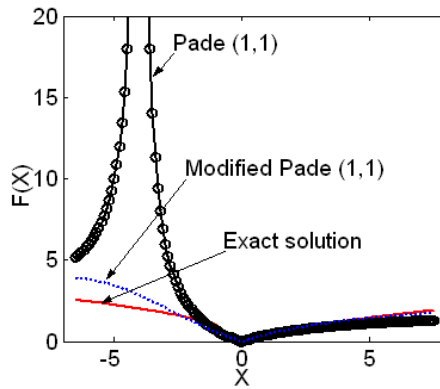


Figure 3.3. The absolute value of  $(1+X)^{1/2}-1$  (solid line), the first-order standard (solid line with circles) and modified (dotted line) Padé approximant of  $(1+X)^{1/2}-1$  with respect to  $X$ .

Table 3.1

Most useful low-order modified Padé approximants of  $\sqrt{1+X}-1$  in terms of the operator X

Order	Expression
(1,0)	$\frac{X}{2\left(1+\frac{j\beta}{2}\right)}$
(1,1)	$\frac{\frac{X}{2}}{1+\frac{X}{4\left(1+\frac{j\beta}{2}\right)}}$
(2,2)	$\frac{\frac{X}{2} + \left(1 + \frac{1}{1+\frac{j\beta}{2}}\right)\frac{X^2}{8}}{1 + \left(2 + \frac{1}{1+\frac{j\beta}{2}}\right)\frac{X}{4} + \frac{X^2}{16\left(1+\frac{j\beta}{2}\right)}}$
(3,3)	$\frac{\frac{X}{2} + \left(3 + \frac{1}{1+\frac{j\beta}{2}}\right)\frac{X^2}{8} + \left(1 + \frac{2}{1+\frac{j\beta}{2}}\right)\frac{X^3}{32}}{1 + \left(4 + \frac{1}{1+\frac{j\beta}{2}}\right)\frac{X}{4} + \left(3 + \frac{3}{1+\frac{j\beta}{2}}\right)\frac{X^2}{16} + \left(\frac{1}{1+\frac{j\beta}{2}}\right)\frac{X^3}{64}}$

### III.1.2. Example

As an example to demonstrate the accuracy of the modified Padé approximant operators for the solution of WA beam propagation problems, a propagation of an initial Gaussian beam having a  $45^\circ$  tilt through a uniform medium [3] is performed. In Ref. [3], the accuracy of the propagation of this Gaussian beam performed by the conventional Padé approximant operators compared to the analytical result was demonstrated. Here, a comparison is done between those obtained by the modified and conventional operators. Figure 3.4 shows the intensity profile of the Gaussian beam after propagating  $10 \mu\text{m}$  calculated by the modified and conventional Padé(1,1) operator. It is seen that the output results are in very good agreement as means to confirm an accuracy of the modified operator.

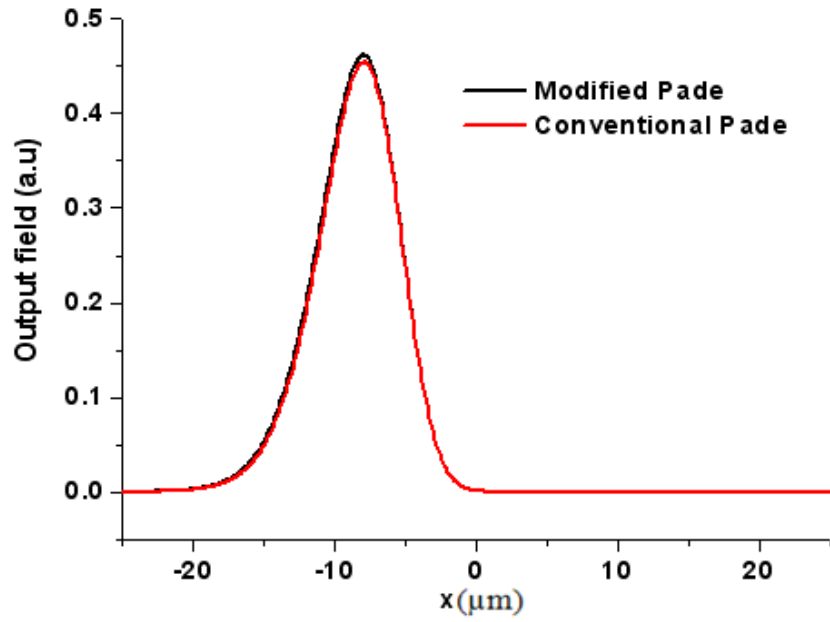


Figure 3.4. Intensity profiles of an initial Gaussian beam with a  $45^\circ$  tilt after propagating  $10\ \mu\text{m}$  in a uniform medium calculated by WA-BPM based on the modified and conventional Padé(1,1) operator.

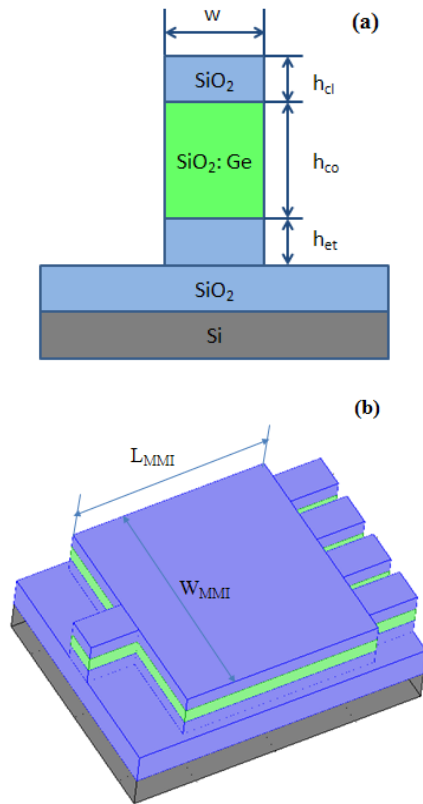


Figure 3.5. Cross section of the deeply-etched  $\text{SiO}_2$  ridge input waveguide (a) and geometry of  $1 \times 4$  MMI coupler (b).

In order to demonstrate the usefulness of modified Padé approximant operators for the solution of WA beam propagation problems, an analysis of a 1x4 multimode interference (MMI) coupler is carried out. The calculated results are compared to those based on conventional Padé approximant operators. The MMI coupler is based on a deeply etched SiO<sub>2</sub> ridge waveguide [4-5]. The main section of such a device allows the propagation of many modes, excited by the field entering the MMI through the input waveguide. The different propagation constants of the excited modes and the respective interferences lead to the formation of multi-fold self-images of the input field at certain distances. The cross section of the input waveguide is shown in Fig. 3.5 (a) where  $h_{co} = 6 \mu\text{m}$ ,  $h_{cl} = 3 \mu\text{m}$ ,  $h_{et} = 3 \mu\text{m}$  and  $w = 6 \mu\text{m}$ . The geometry of the MMI coupler is sketched in Fig. 3.5 (b) where the length  $L_{MMI}$  and the width  $W_{MMI}$  of the device is  $245 \mu\text{m}$  and  $32 \mu\text{m}$ , respectively. The refractive index of the SiO<sub>2</sub> substrate is 1.46 and the refractive index contrast between the Ge doped core (SiO<sub>2</sub>:Ge) and the substrate is 0.75%. The excited field is the fundamental mode of the input ridge waveguide at  $\lambda = 1.55 \mu\text{m}$  and is depicted in Fig. 3.6.

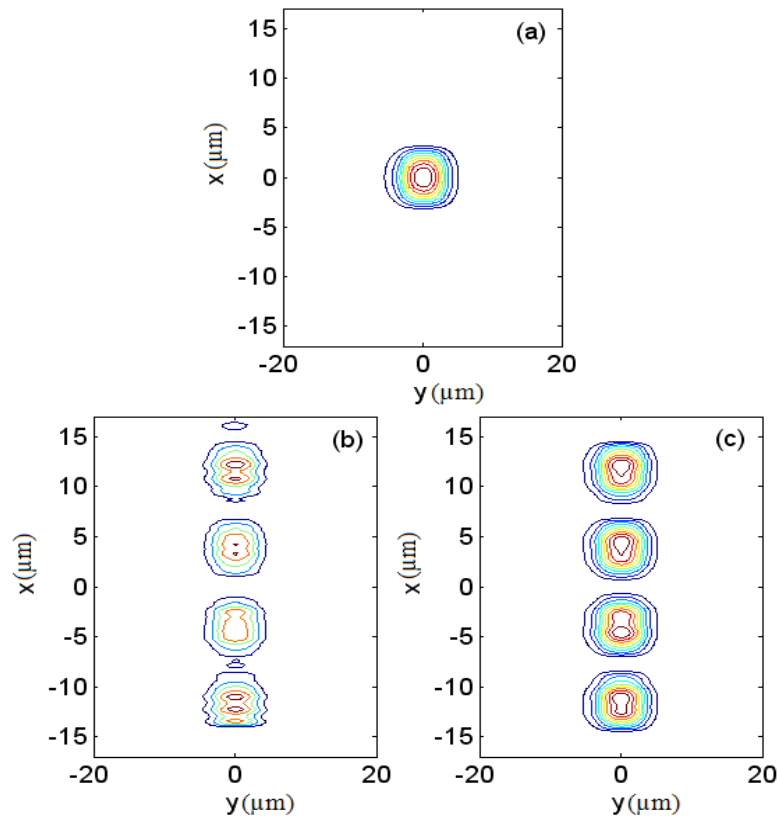


Figure 3.6. Input field (a) and output fields on the exit plane of MMI calculated by WA-BPMs based on the conventional (b) and the modified (c) Padé(1,1) approximant operator.

The same figure shows the field after propagating 245  $\mu\text{m}$  calculated by the BPM based on the conventional and the modified Padé(1,1) operator, respectively. It illustrates the self-imaging of the input field and the field at the exit face of the MMI coupler. It can be seen that the results of the conventional method are much more noisy compared to those of the modified method. In order to quantify the relative error (RE) and to show the benefits of the modified Padé(1,1) approximant operator, the following formula is used:

$$RE = \left[ \frac{\iint |\psi^{\Delta z} - \psi^{0.02 \mu\text{m}}|^2 dx dy}{\iint |\psi^{0.02 \mu\text{m}}|^2 dx dy} \right]^{\frac{1}{2}}, \quad (3.6)$$

where  $\psi^{\Delta z}$  are the output fields at the exit face of the MMI coupler obtained for various propagation steps and  $\psi^{0.02 \mu\text{m}}$  is the reference output field obtained with the smallest propagation step resolution used of 0.02  $\mu\text{m}$ . The computational window used of 34x40  $\mu\text{m}$  is discretized by  $\Delta x = \Delta y = 0.2 \mu\text{m}$ . Table 3.2 shows these relative errors for fields calculated by the conventional and the modified Padé-based WA-BPM with various propagation step resolutions (0.2  $\mu\text{m}$ , 0.1  $\mu\text{m}$ , 0.05  $\mu\text{m}$ ). It is clearly seen that the relative errors obtained by the modified Padé-based BPM are much smaller than those obtained by the conventional one for the same propagation step. Thus, WA-BPMs based on the modified Padé operators can offer the advantage of using larger propagation steps than the conventional method for the same accuracy, with an associated reduction in computational effort.

Table 3.2.

Relative error (%) of output fields calculated by the modified and conventional Padé-based BPM with various propagation steps using an output field modeled with 0.02  $\mu\text{m}$  step as a reference.

Grid size ( $\mu\text{m}$ )	0.2	0.1	0.05
Operators			
Modified Padé	0.36	0.08	0.02
Conventional Padé	7.26	3.81	1.93

### III.1.3. Generalized rectangular WA-BPMs using modified operators

The simplest and most widely used technique to deal with the Padé approximant operators based WA-BPMs is the finite difference discretization of the propagation equation, hereafter referred as the standard WA-BPMs (S-WA-BPMs). However, the efficiency and accuracy of this method is limited by several factors resulting from either the approximation of partial derivatives with finite differences or the staircase approximation of the structures studied. In many cases the staircase approximation can be eliminated by using coordinate systems which accurately describe the geometry of the devices. In particular, the nonorthogonal coordinate systems were employed for this purpose with particular success [6-7]. Nevertheless, they still suffer from the staircase approximation problem when applying the finite difference BPM for analysis of beam propagation in high index contrast structures. Recently, a solution for this problem was suggested in [8]. The proposed algorithm results in the so-called slanted-wall beam propagation as briefly presented in the previous chapter, which is well-suited for studying wide-angle propagation through a general class of optical-waveguide structures defined by dielectric interfaces that may be slanted with respect to the propagation direction. When used with an appropriate grid-generation algorithm, the method allows the modeling of an extremely wide variety of high-index-contrast structures with good phase accuracy and energy conservation. However, this method is limited to 2D beam propagation problems.

In addition, it was shown that the oblique coordinate system not only reduces the staircasing problem but also allows for arbitrary selection of the proper direction of propagation [9]. This results in the relaxation of computational efforts in comparison with the S-WA-BPM in the rectangular coordinate. However, the oblique coordinate system is not orthogonal. Consequently, the power conservation cannot be guaranteed in general.

Recently, by introducing a generalized envelope function it was shown that these problems can be overcome [10]. It results in the so-called generalized rectangular WA-BPM, hereafter referred to as the GR-WA-BPM. The proposed algorithm keeps all the advantages of the standard WA-BPM in the rectangular coordinate system while adding flexibility in the selection of the preferred propagation direction. Here, the adaptation of the modified Padé approximant operators for the GR-WA-BPM is presented. It not only allows even more accurate approximations to the true generalized rectangular Helmholtz equation but also gives the evanescent modes the desired damping [11].

By introducing the generalized envelope function [10]

$$\Psi(x, y, z) = \Phi(x, y, z) \exp[ik \cos(\theta)z + ik \sin(\theta)x] \quad (3.7)$$

where  $k=k_0n_{\text{ref}}$ ,  $n_{\text{ref}}$  is the reference refractive index and by inserting it into Eq. (2.9), the following equation is obtained

$$\frac{\partial^2 \Phi}{\partial z^2} + 2jk \cos \theta \frac{\partial \Phi}{\partial z} + P\Phi = 0, \quad (3.8)$$

where operator P is given by

$$P = \frac{\partial^2}{\partial y^2} + \frac{\partial^2}{\partial x^2} + 2jk \sin \theta \frac{\partial}{\partial x} + k_0^2 (n^2 - n_{\text{ref}}^2). \quad (3.9)$$

The generalized envelope function introduces two parameters, namely  $k$  and  $\theta$ . These parameters can be freely chosen to match best the requirements of the problem studied. It is known that the standard envelope function used in BPMs so far has only one adjustable parameter, which is typically referred to as the reference refractive index. This parameter has a major impact on the accuracy of the calculations and should be carefully selected. By adding another parameter to the envelope function an additional degree of freedom is gained that allows for decoupling the preferred direction of propagation of BPMs from the coordinate system used.

Eq. (3.8) can be rearranged as follows:

$$\frac{\partial \Phi}{\partial z} - \frac{j}{2k \cos \theta} \frac{\partial^2 \Phi}{\partial z^2} = \frac{jP}{2k \cos \theta} \Phi \quad (3.10)$$

which can be formally rewritten as

$$\frac{\partial \Phi}{\partial z} = \frac{\frac{iP}{2k \cos \theta}}{1 - \frac{i}{2k \cos \theta} \frac{\partial}{\partial z}} \Phi. \quad (3.11)$$

Eq. (3.11) suggests the recurrence relation

$$\left. \frac{\partial}{\partial z} \right|_{n+1} = \frac{\frac{iP}{2k \cos \theta}}{1 - \frac{i}{2k \cos \theta} \left. \frac{\partial}{\partial z} \right|_n} \Phi. \quad (3.12)$$

By using the initial value of  $\left. \frac{\partial}{\partial z} \right|_0 = 0$ , this gives us the well-known Padé(m,n) approximant-

based WA beam propagation formula as follows:

$$\frac{\partial \Phi}{\partial z} \approx ik \cos(\theta) \frac{N(m)}{D(n)} \Phi \quad (3.13)$$

where  $N(m)$  and  $D(n)$  are polynomials in  $X = \frac{P}{k^2 \cos^2(\theta)}$ . However, as we addressed earlier [1],

Padé(m,n) approximants incorrectly propagate evanescent modes. To overcome this problem a modified Padé(m,n) approximant is used here. It not only allows more accurate approximations to the true generalized rectangular Helmholtz equation but also gives the evanescent modes the desired damping. It is obtained by using the same recurrence formulation of standard Padé(m,n) approximants but with again another different initial value. Here, by following the same steps as in case of the S-WA-BPM based on modified Padé(m,n) approximants, it was found that the initial value for the recurrence relation (3.12) in the GR-WA-BPM based on modified Padé(m,n) approximants is  $\left. \frac{\partial}{\partial z} \right|_0 = -k \cos(\theta) \beta$ , where  $\beta$  is a damping parameter, which can be chosen as well, which is typically set to 2.

As an example to show the benefits of the modified Padé(1,1) approximant operator for the GR-WA-BPMs, an analysis of a 5-degree tilted waveguide is carried out. In the tilted waveguide the fundamental mode for the slab of width  $w = 1 \mu\text{m}$  with cladding indexes of 3.17 is propagated through  $10 \mu\text{m}$  at wavelength  $\lambda = 1.55 \mu\text{m}$  in a medium of refractive index  $n = 3.4$  and with the propagation step size of  $\Delta z = 0.05 \mu\text{m}$ . The resulting intensity profile for the standard WA-BPM is shown in Fig. 3.7 (a). The intensity peaks of a beam propagating along a tilted waveguide calculated by the S-WA-BPM and GR-WA-BPM are shown in Fig. 3.8. As shown in the figures, the sudden changes in dielectric constant resulting from the stair-stepping procedure have generated nonphysical ripples in the waveform and have led to a spurious radiation loss. This effect is sensitive to index contrast. Low index contrast problems have been successfully addressed in the past using this standard method. However, high index contrast problems can often generate sufficient scattering as to render the method completely useless. The corresponding intensity profile for the GR-WA-BPM is depicted in Fig. 3.7 (b). In contrast to the previous case, all profiles are relatively uniform and smoother than those based on the S-WA-BPM as clearly seen in Fig. 3.8. It is worth mentioning that a previous work [10] already confirmed that the GR-WA-BPM could be performed with a low loss of accuracy in terms of energy conservation.

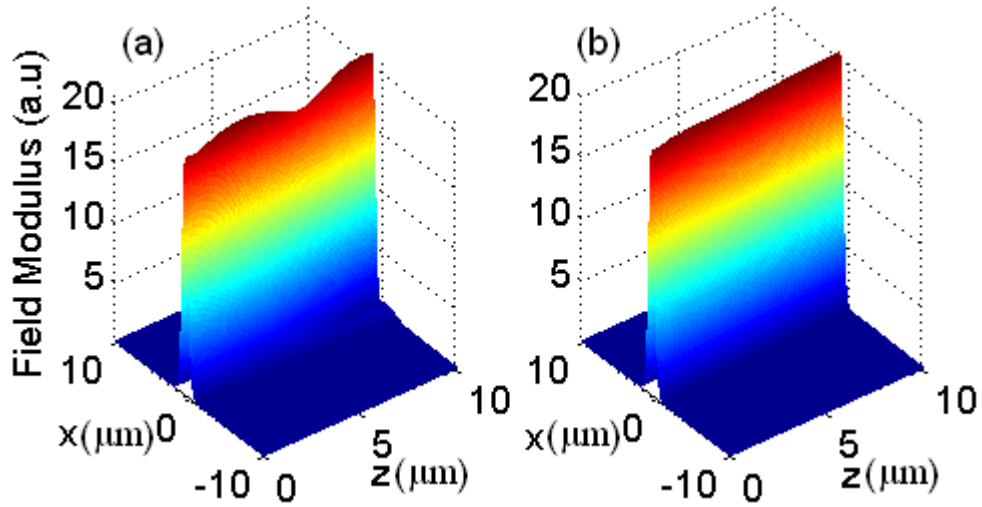


Figure 3.7. Intensity profiles along a tilted waveguide for (a) the standard and (b) the generalized rectangular wide-angle propagation.

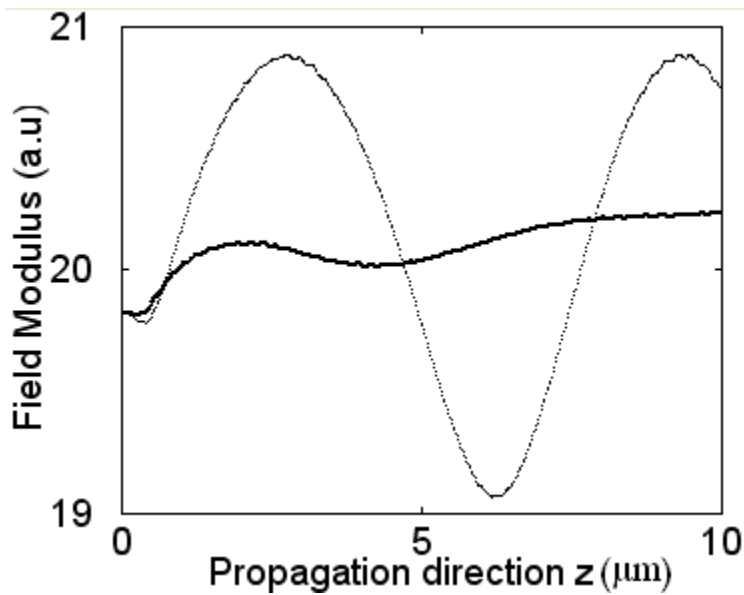


Figure 3.8. Intensity peaks along a tilted waveguide for the standard (dotted line) and the generalized rectangular (solid line) wide-angle propagation.

### III.1.4. Application of modified Padé approximant operators for time-domain BPMs

In this section, the usefulness of the modified Padé approximant operators for the solution of time-domain beam propagation problems is demonstrated. This is shown both for a wideband method which can take reflections into account and for a split-step method for modeling of ultrashort unidirectional pulses. The resulting approaches achieve high-order accuracy not only in space but also in time, as we published in [12]. This work was done in collaboration with Trevor Benson's group in the University of Nottingham, UK.

As mentioned in Chapter II, time-domain BPMs come in two flavours. The first one is used for treating reflected waves and the second one is used for modeling ultrashort pulses propagating in wide-angle structures. Now, we will present the derivation of the modified Padé approximant operators for these two time-domain methods.

#### III.1.4.1. Time-domain BPMs for treating reflected waves

The formal solution of Eq. (2.31) can be rewritten in the following well-known form [13]:

$$\frac{\partial \psi}{\partial t} = -i\omega_0 \left(1 - \sqrt{1 - X}\right) \psi \quad (3.14)$$

with  $X = P/\omega_0^2$ . In addition, to allow numerical methods to solve Eq. (2.31) effectively, its approximate solution is usually obtained by the conventional Padé approximant method. The conventional Padé propagators are well-known and result from the recurrence relation with the initial value of  $\left. \frac{\partial}{\partial t} \right|_0 = 0$  in the following form:

$$\left. \frac{\partial}{\partial t} \right|_{n+1} = -i\omega_0 \frac{\frac{X}{2}}{1 - \frac{j}{\omega_0} \left. \frac{\partial}{\partial t} \right|_n} \quad (3.15)$$

For  $\left. \frac{\partial}{\partial t} \right|_2$ , this results in the well-known Padé(1,1) approximant-based wideband beam propagation formula:

$$\frac{\partial \psi}{\partial t} \approx -i\omega_0 \frac{\frac{X}{2}}{1 - \frac{X}{4}} \psi \cdot \quad (3.16)$$

If Eq. (3.16) is compared to the formal solution of wave equation given in (3.14), the approximation formula is obtained as follows:

$$1 - \sqrt{1 - X} \approx \frac{\frac{X}{2}}{1 - \frac{X}{4}}. \quad (3.17)$$

However, as already mentioned, as the denominator of the Padé (1,1) approximant gradually approaches zero its absolute value approaches  $\infty$ . Physically this means that the conventional Padé approximant incorrectly propagates the evanescent modes. To circumvent this problem the modified Padé approximant using a different initial value is proposed. To apply the modified operators for the time-domain wave equation in this work, the initial value is set at  $\left. \frac{\partial}{\partial t} \right|_0 = -\omega_0 \beta$  where  $\beta$  is a damping parameter, which is typically set to 2. For  $\left. \frac{\partial}{\partial t} \right|_2$ , the first-order modified Padé(1,1) approximant operator is given as follows:

$$\frac{\partial \psi}{\partial t} \approx -i\omega_0 \frac{\frac{X}{2}}{1 - \frac{X}{4(1 + i\frac{\beta}{2})}} \psi. \quad (3.18)$$

To demonstrate the benefits of using the modified operators for time-domain BPMs to treat reflected waves, we perform an analysis of waves propagating in a highly reflective structure. The structure investigated in this work is an optical grating as shown in Fig. 3.9, where the number of grating periods is eight and the guiding core thickness is 0.3  $\mu\text{m}$ . Obviously, reflections are important in such a structure, so we use the method we just described. The input pulse has a transverse profile  $\psi_0(x)$  corresponding to the fundamental mode of the planar waveguide and a Gaussian profile in the longitudinal direction. At time  $t = 0$ , it is given as

$$\psi(x, z, t = 0) = \psi_0(x) \exp\left[-\left(\frac{z - z_0}{w_0}\right)^2\right] \exp[-ik_{\text{eff}}(z - z_0)] \quad (3.19)$$

where  $k_{\text{eff}}$  is the effective propagation constant,  $z_0$  is the center position of the input pulse and  $w_0$  is the spot size. Here,  $z_0 = 1 \mu\text{m}$ ,  $w_0 = 0.5 \mu\text{m}$  and carrier center wavelength  $\lambda = 1.5 \mu\text{m}$  is chosen, respectively. The spatial distribution of the pulse at time  $t = 0$  is superimposed on Fig. 3.9.

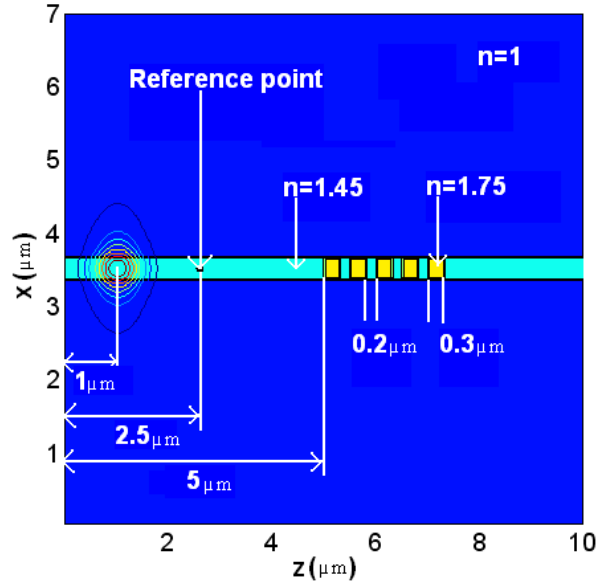


Figure 3.9. Optical grating with modulated refractive index with input pulse at time  $t = 0$  superimposed.

The reflected pulse is monitored inside the waveguide at a certain reference point which is indicated in the same figure. In order to show the benefits of the modified Padé(1,1) approximant operator, the relative error (RE) of the field profile as a function of time is calculated at the reference point and defined as:

$$RE = \left[ \frac{|\psi_p^{\Delta t} - \psi_p^{0.1 fs}|^2}{|\psi_p^{0.1 fs}|^2} \right]^{\frac{1}{2}}, \quad (3.20)$$

where  $\psi_p^{\Delta t}$  is the field profile at the reference point obtained with various time step resolutions and  $\psi_p^{0.1 fs}$  is the reference solution obtained with the smallest time step resolution used of  $0.1 fs$ .

Figure 3.10 shows this error both for the conventional Padé (cPade) and the modified one (mPade) with various time step resolutions ( $0.5 fs$ ,  $1 fs$ ,  $2 fs$ ). The relative errors obtained by TD-BPM based on the modified Padé(1,1) operator are much smaller than those obtained by the conventional one. This is attributed to more accurate approximations to the wave equation of the modified operator. It leads to the conclusion that using the modified Padé operator allows for propagation with larger time steps for a given accuracy, which is beneficial for computational speed.

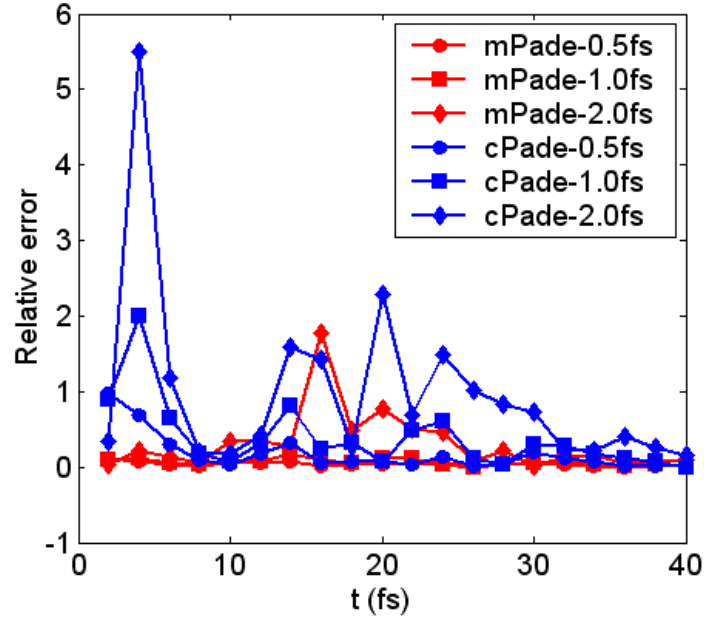


Figure 3.10. Relative error of the field monitored at the reference point calculated by the modified (red lines) and conventional (blue lines) Padé-based TD-BPM with various time steps using the field at 0.1 fs as a reference. The relative error approaches zero for longer time since the field moves far away from the reference point where the intensity profile decreases to zero.

### III.1.4.2. Time-domain BPMs for modeling ultrashort pulses in wide-angle structures

Apart from being successful in treating reflected waves, these time-domain BPMs have also found an application in the analysis of ultrashort pulses propagating in wide-angle waveguides. The method used for such an analysis is the method 2 presented in Section II.3.2 of Chapter II. Since Eq. (2.34) there, the main equation for analysis of ultrashort pulses, has a form similar to Eq. (2.31), the equation for treating reflected waves, one can easily obtain the modified Padé approximation to the time-domain wave equation for analysis of ultrashort pulse propagation by following the same steps as described above.

As an example to illustrate this method, the simulation of ultrashort pulse propagation in a Y-branch waveguide structure is carried out. Here, reflections are negligible, but the problem is wide-angle. In this waveguide the initial waveguide is split into two 10-degree tilted waveguides. The guiding core has an index of 3.6 and has a thickness  $0.25 \mu\text{m}$  while the refractive index of the cladding is 3.24, as shown in Fig. 3.11, and the wavelength is  $\lambda=1.55 \mu\text{m}$ .

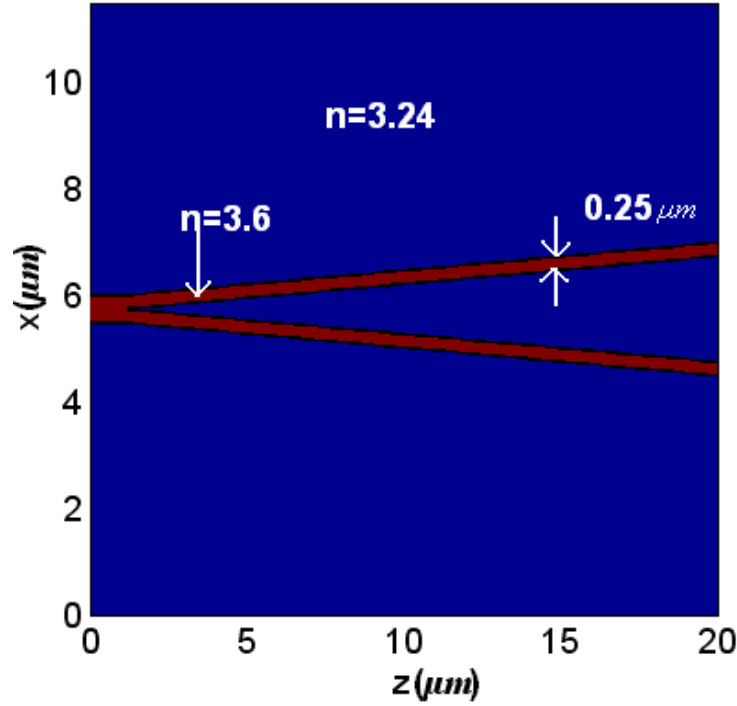


Figure 3.11. 2D Y-branch waveguide

The input source is given by

$$\psi(x, \tau) = \psi_0(x) \exp \left[ - \left( \frac{\tau - \tau_0}{T} \right)^2 \right], \quad (3.21)$$

with  $\psi_0(x)$  being the fundamental mode of the planar waveguide and  $\tau_0 = 60$  fs,  $T = 20$  fs as shown in Fig. 3.12 (a). The same figure shows the ultrashort pulse after propagating  $20 \mu\text{m}$  calculated by the TD-BPM based on the conventional (b) and the modified (c) Padé(1,1) operator. It can be seen that the results of the conventional method are much more noisy compared to those of the modified method. To quantify the relative error this time the following formula is used:

$$RE = \left[ \frac{\iint |\psi^{\Delta z} - \psi^{0.02 \mu\text{m}}|^2 dx d(c\tau)}{\iint |\psi^{0.02 \mu\text{m}}|^2 dx d(c\tau)} \right]^{\frac{1}{2}}, \quad (3.22)$$

where  $\psi^{\Delta z}$  are the output pulses obtained for various propagation steps and  $\psi^{0.02 \mu\text{m}}$  is the reference pulse obtained at a propagation step of  $0.02 \mu\text{m}$ .

In table 3.3 these relative errors for pulses calculated by the conventional and the modified Padé-based TD-BPM with various propagation step resolutions (0.2  $\mu\text{m}$ , 0.1  $\mu\text{m}$ , 0.05  $\mu\text{m}$ ) are shown. It is clearly seen that the relative errors obtained by the modified Padé-based TD-BPM are much smaller than those obtained by the conventional one for the same propagation step. Thus, TD-BPMs based on the modified Padé operators can offer the advantage of using larger propagation steps than the conventional method for the same accuracy, with an associated reduction in computational effort.

Table 3.3.

Relative error (%) of ultrashort pulses calculated by the modified and conventional Padé-based TD-BPM with various propagation steps using a pulse modeled with 0.02  $\mu\text{m}$  step as a reference.

Grid size ( $\mu\text{m}$ )	0.2	0.1	0.05
Operators			
Modified Padé	47.9	4.78	3.22
Conventional Padé	69.1	22.81	8.61

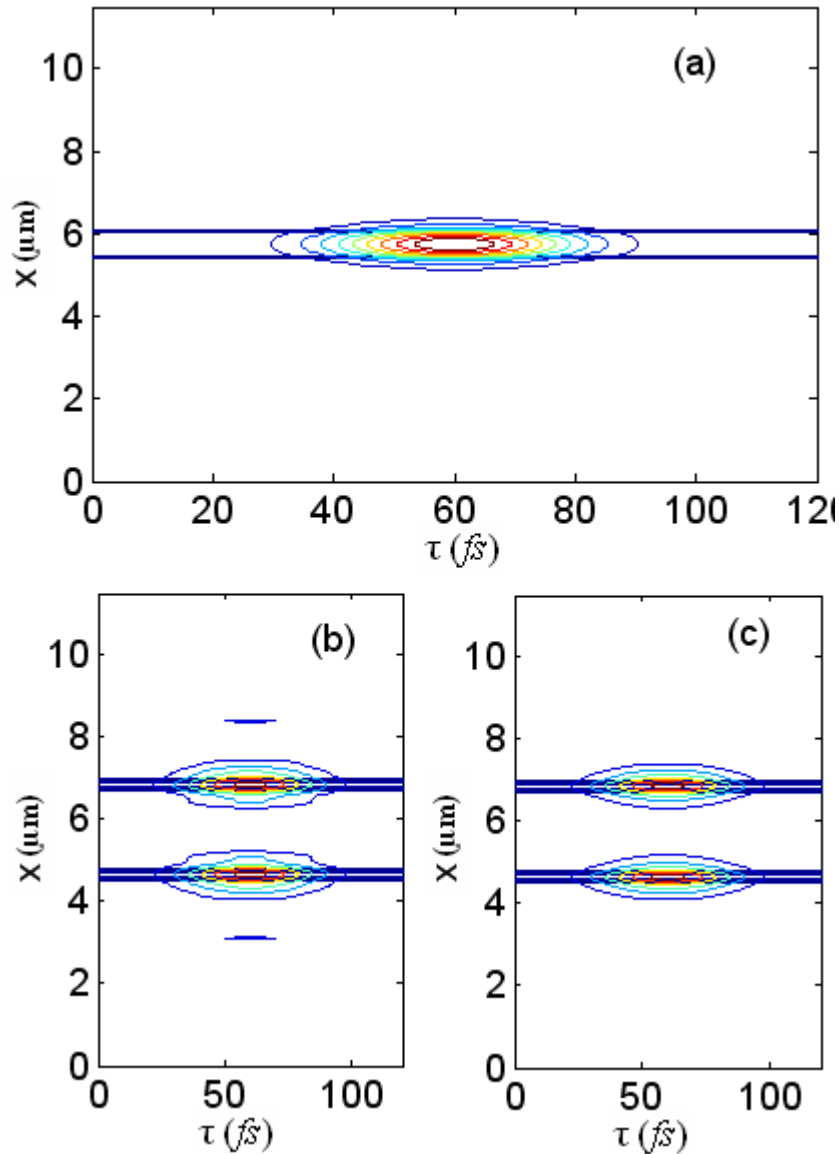


Figure 3.12. Time evolution of transverse input field (a) and output fields after propagating  $20 \mu\text{m}$  calculated by TD-BPM based on the conventional (b) and the modified (c) Padé(1,1) approximant operator in the Y-branch waveguide. Each part of the figure shows the moving time window of width 120 fs used to monitor the pulse. The local waveguide geometry has been superimposed as a guide to the reader.

### III.1.5. Comparative assessment of time-domain models of nonlinear optical propagation

In this section, the TD-BPM developed above is extended to study beam propagation in nonlinear waveguides. The feasibility of the method is shown through a comparison with the rigorous transmission line modeling (TLM) method. The comparative assessment is carried out on the basis of reflection and transmission of non-stationary light beams propagating through the junction of linear and nonlinear waveguides. This result was presented in [14] within a collaboration with Trevor Benson's group as well.

The availability of laser sources generating high-intensity femtosecond optical pulses has recently inspired tremendous research interest in the study of novel guiding structures and materials for nonlinear optics applications. In order to study the spatiotemporal dynamics of femtosecond laser pulses propagating in a Kerr-type nonlinear medium, various treatments have been proposed including those based on the generalized nonlinear Schrodinger equation (GNLSE), the finite-difference time-domain (FDTD) method and the TLM method [15].

A GNLSE-based method is usually feasible when modelling the propagation of optical pulses whose duration is more than several periods of oscillations of the carrier frequency. However, the main limitation of the method lies in the paraxial approximation to the wave equation under the slowly varying envelope approximation (SVEA) where the second-order derivatives in the wave equation are ignored.

The FDTD and TLM methods are well-known rigorous time-domain techniques providing reliable conduits for comparisons. The main difference between these two widely used time-domain techniques is the layout of the time-stepping and the unit cell process. In the TLM method, the fields are solved at the same time instant at the centre of the TLM cell resulting in a straightforward solution of nonlinear equations, whereas in the FDTD method there is a separation of half a space step and half a time step between the electric and magnetic fields. However, these methods require a very small time step size to fulfil the stability criterion. This leads to a substantial increase in the computational resources required, especially for the analysis of long lengths of optical waveguides.

Recently, simple and efficient BPMs in time domain have been developed [16-17]. These methods deal with reflected waves, and have been successfully employed for the analysis of both

TE and TM-modes propagating in photonic crystal structures. The time-domain BPM allows higher time step size than TLM and FDTD (thus resulting in reduced computational efforts) and achieve high-order accuracy not only in space but also in time. However, this TD-BPM was based on the conventional Padé(1,1) approximant operator. As shown in the previous section, those based on the modified operator may offer much more benefits. In this section, a comparative assessment between time-domain BPMs based on the modified Padé(1,1) operator and the other existing time-domain methods is done by investigating the reflection and transmission of the non-stationary light beams propagating through the junction of linear and nonlinear waveguides.

A detailed description of GNLSE-based and TLM methods was already presented in [15]. For TD-BPMs, since the assessment is done on the basis of reflection and transmission of non-stationary light beams, the method 1 presented in Section II.3.1 of Chapter II which can deal with reflection problems is used. There, the refractive index of a material having an instantaneous Kerr nonlinearity can be expressed as  $n = n(x,z,t;|\psi|^2)$ . Since it depends on the intensity of the field, an iterative algorithm is included for efficiently evaluating the nonlinear refractive index. The solution at the forward step is recalculated with the modified nonlinear refractive index, and the scheme is continued until the solution at the forward step converges.

The structure examined is shown in Fig. 3.13 where the linear and nonlinear waveguides of the junction have the same core thickness  $d$  and linear refractive index profile. The problem is reduced to the consideration of a TE-polarized non-stationary light beam and instantaneous Kerr nonlinearity. The initial spatiotemporal distribution in the linear waveguide is taken as a Gaussian pulse in time multiplied with a linear fundamental mode in the transverse plane at wavelength  $\lambda_0 = 1.53 \mu\text{m}$ .

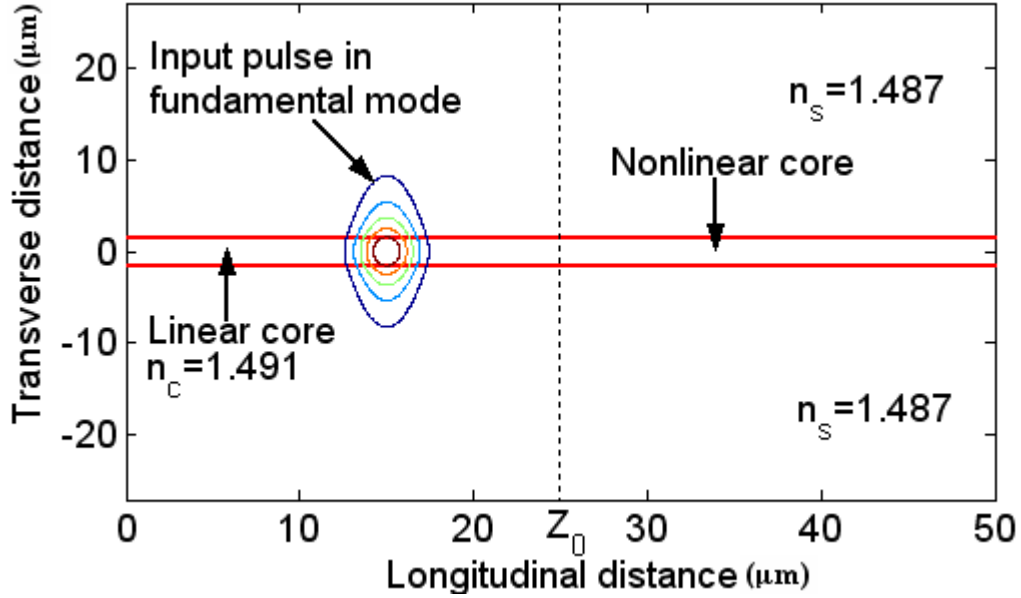


Figure 3.13. Junction of linear and nonlinear planar waveguides.

As a reference parameter to quantify the amount of nonlinear propagation,  $n_K I_0$  is used where  $I_0$  is the peak intensity of the input pulse and  $n_K$  is Kerr nonlinear coefficient. This parameter is dimensionless and combines both nonlinear material properties and the highest beam intensity. It determines the maximum value of the nonlinear part of the real refractive index induced by the high-intensity light beam in the nonlinear material with Kerr nonlinearity.

In the comparative assessment, only short propagation distances in the nonlinear waveguide are considered and material dispersion effects are ignored. The non-stationary light beam is simulated by employing a uniform transverse computational grid over the space  $(-X_2: X_2)$  so that the spatial distribution of the electric field at a given moment is calculated. As an output parameter the normalized energy of the pulse propagating in the nonlinear waveguide is evaluated as:

$$R_n(t), T_n(t) = \frac{\int_{Z_1}^{Z_2} \int_{-X_2}^{X_2} dz dx |\psi(x, z, t)|^2}{\int_{Z_1}^{Z_2} \int_{-X_2}^{X_2} dz dx |\psi(x, z, 0)|^2}; n=1,2 \quad (3.23)$$

where for reflection ( $R_n$ )  $Z_1=0$  and  $Z_2=Z_0$  and for transmission ( $T_n$ )  $Z_1=Z_0$  and  $Z_2=\infty$ . The transverse integration is taken over the waveguide core ( $x < |X_1|$ ), or the full range ( $x < |X_2|$ ) within the moving computational frame.

In this work, results are calculated for two pulse durations (18 and 36 fs) and are shown in Figs. 3.14 and 3.15. The pulse is launched in the linear waveguide at time  $t=0$ , and centred 15  $\mu\text{m}$  away from the linear and nonlinear boundary. The reflected and transmitted energies are evaluated when the transmitted pulse just resides fully in the nonlinear waveguide.

From the numerical simulations, we observed that low intensity pulses propagate in the cladding at different angles to the waveguide axis in the backward and forward directions. Some part of the reflected radiation is confined in the linear waveguide and propagates in the backward direction in the core, the pulse duration being less than that of the initial pulse. The reflection coefficient calculated (the total normalized energy reflected by the junction  $R_2$ ) increases with  $n_{\kappa}I_0$  and does not depend on pulse duration within each method as seen in Fig. 3.14 (a). The set of results calculated by wideband TD-BPM and TLM show a slight difference because of the low order Padé(1,1) approximant operator of the TD-BPM. The agreement between results could be improved by using higher order Padé approximant operators [16]. The distribution of the reflected radiation in the core depends on both  $n_{\kappa}I_0$  and the pulse duration, as shown in Fig. 3.14 (b). The slight dependency in this reflection coefficient on pulse duration is due to the fact that with an increase in pulse duration a greater part of the initial pulse energy is scattered into the cladding.

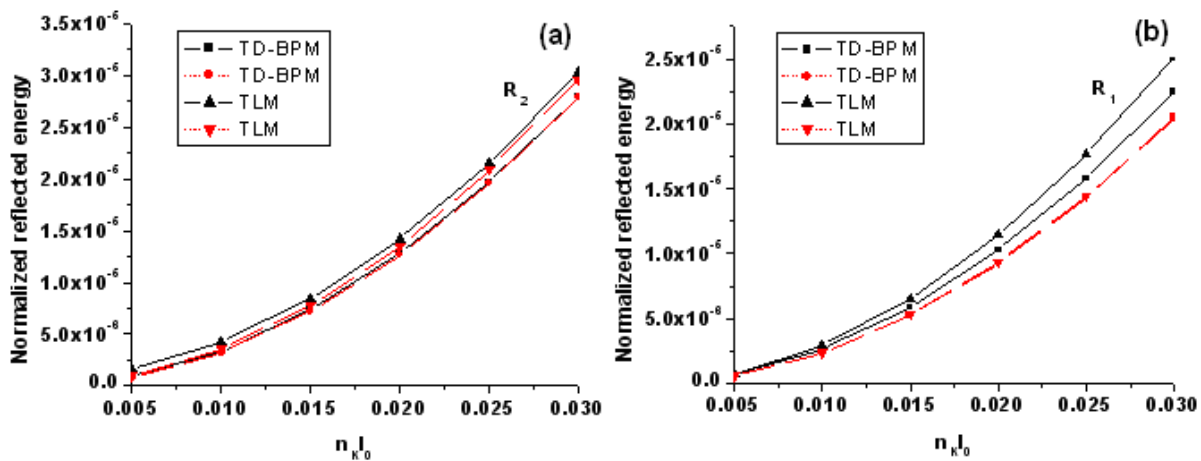


Figure 3.14. (a) Total reflected energy  $R_2(t)$  and (b) reflected energy in the core  $R_1(t)$ . Pulse durations 18 fs (solid lines) and 36 fs (dashed lines).

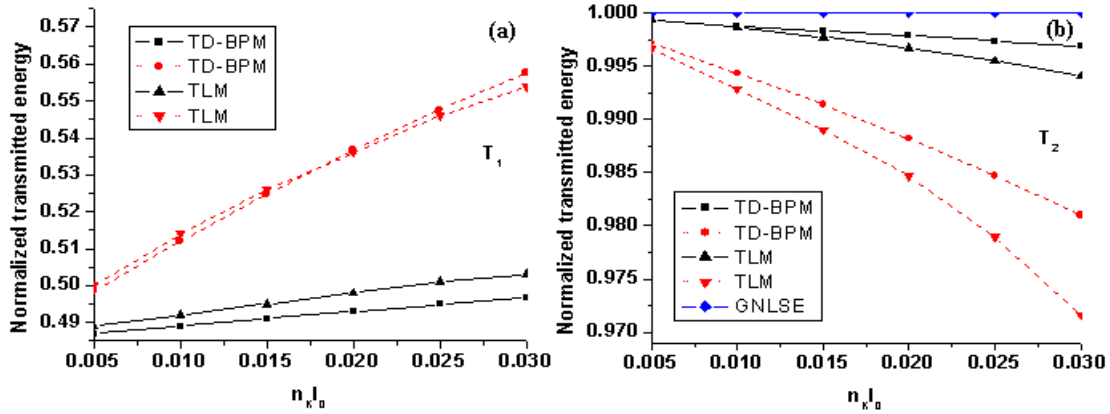


Figure 3.15. (a) Transmitted energy in the core and (b) total transmitted energy. Pulse durations 18 fs (solid lines) and 36 fs (dotted lines).

The energy  $T_1$  of the forward propagating pulse in the core of the nonlinear waveguide increases with an increase in  $n_k I_0$  due to the self-focusing effect (Fig. 3.15 (a)). This is accompanied by a decrease of the total transmitted energy  $T_2$  due to radiative (or scattering) losses, as seen in Fig. 3.15 (b). This loss is caused by the difference of refractive index of the nonlinear core compared to the linear core. For a given value of  $n_k I_0$  the normalized transmitted energy in the core decreases with an increase in initial pulse duration. This may be explained by the fact that there is a difference in the initial pulses' energy. In Fig. 3.15 the dotted lines correspond to a pulse duration twice that of the solid lines; this means a two-fold increase of the initial energy. In general, the TLM results show greater spatial variations of the light beam in the process of self-focusing in comparison with the TD-BPM results. There exists a small difference between the transmitted energies calculated by the TD-BPM and TLM methods. Again, this is due to the low order approximation in bandwidth of the Padé(1,1) TD-BPM method used. The GNLSE scheme used is not a reflective one and total forward propagating energy remains constant.

In summary, numerical time-domain techniques have been employed to study the excitation of a nonlinear planar waveguide by a non-stationary light beam. TLM is already established as a rigorous technique to model transmitted and reflected beams. However, it requires a very small time step (Courant condition) and thus significant computational effort is needed. The TD-BPM provides an attractive alternative numerical technique for nonlinear optical analysis and even with a Padé(1,1) approximation in time gives a good improvement over the GNLSE-based approach.

## III.2. KP approximant operators for WA-BPMs without using slowly varying envelope approximation

In this section, yet another new class of approximant operators, hereafter referred as KP approximant operators for WA-BPMs, is developed. We published this in [18]. Unlike the previous well-known WA-BPM based on Padé operators, the resulting formulations allow direct solution of the second-order scalar wave equation without having to make slowly varying envelope approximations so that the WA formulations are completely general. The accuracy and improvement of this approximate calculation of the propagator is demonstrated in comparison with the exact result and existing approximate approaches. The method is employed to simulate 2D and 3D optical waveguides and is compared with the results obtained by the existing approach.

### III.2.1. Formulation

The scalar wave equation Eq. (2.9) is rewritten as follows:

$$\frac{\partial^2 \Psi}{\partial z^2} = -P\Psi, \quad (3.24)$$

with  $P = \nabla_{\perp}^2 + k_0^2 n^2 = \frac{\partial^2}{\partial x^2} + \frac{\partial^2}{\partial y^2} + k_0^2 n^2$ . Note that there is no reference refractive index included in operator P.

By multiplying both sides of Eq. (3.24) with  $-\frac{i}{2k}$  and then adding  $\frac{\partial \Psi}{\partial z}$  on each side, we get

$$-\frac{i}{2k} \frac{\partial^2 \Psi}{\partial z^2} + \frac{\partial \Psi}{\partial z} = \frac{iP}{2k} \Psi + \frac{\partial \Psi}{\partial z}, \quad (3.25)$$

where  $k = k_0 n_{\text{ref}}$ ,  $n_{\text{ref}}$  is the reference refractive index.

Eq. (3.25) can be formally written in the form

$$\frac{\partial \Psi}{\partial z} = \frac{\frac{iP}{2k} + \frac{\partial}{\partial z}}{1 - \frac{i}{2k} \frac{\partial}{\partial z}} \Psi, \quad (3.26)$$

Eq. (3.26) suggests the recurrence relation

$$\left. \frac{\partial}{\partial z} \right|_{n+1} = \frac{\frac{iP}{2k} + \left. \frac{\partial}{\partial z} \right|_n}{1 - \frac{i}{2k} \left. \frac{\partial}{\partial z} \right|_n}. \quad (3.27)$$

By using the initial value of  $\left. \frac{\partial}{\partial z} \right|_0 = 0$ , this gives us the KP(m,n) approximant-based WA beam propagation formula as follows:

$$\frac{\partial \Psi}{\partial z} \approx ik \frac{N(m)}{D(n)} \Psi \quad (3.28)$$

where  $N(m)$  and  $D(n)$  are polynomials in  $X = \frac{P}{k^2}$ . The most useful low-order KP approximant operators are shown in table 3.4.

Table 3.4

Most useful low-order KP approximants of  $\sqrt{X}$  in terms of the operator X

Order	Expression
(1,1)	$\frac{X}{1 + \frac{X}{4}}$
(2,2)	$\frac{2X + \frac{X^2}{2}}{1 + \frac{3X}{2} + \frac{X^2}{16}}$
(3,3)	$\frac{3X + \frac{5X^2}{2} + \frac{3X^3}{16}}{1 + \frac{15X}{4} + \frac{15X^2}{16} + \frac{X^3}{64}}$

### III.2.2. Analytical assessment

If Eq. (3.28) is compared with a formal solution of Eq. (3.24) written in the well-known form

$$\frac{\partial \Psi}{\partial z} = i\sqrt{P}\Psi = ik\sqrt{X}\Psi \quad (3.29)$$

the approximation formula is given by

$$\sqrt{X} \approx \frac{N(m)}{D(n)}. \quad (3.30)$$

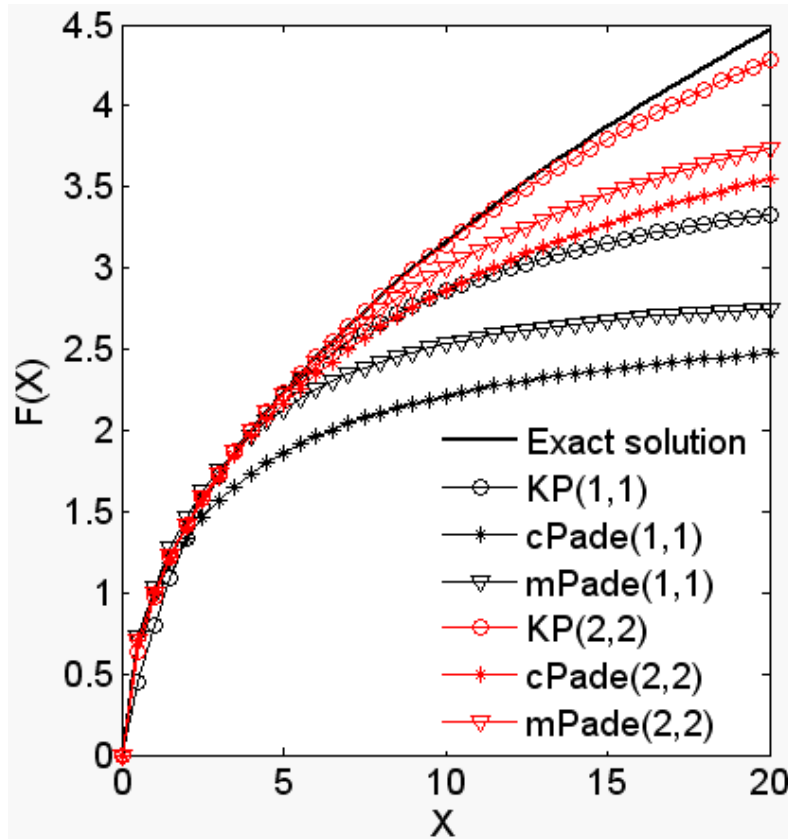


Figure 3.16. The absolute values of  $X^{1/2}$  (solid line), the most useful low-order conventional (cPade) and modified (mPade) Padé(m,n) approximants, and KP(m,n) of  $X^{1/2}$  (dotted lines).

Since the operator  $X$  has a real spectrum, it is useful to consider the approximation of  $\sqrt{X}$  by the KP approximant operators. Figure 3.16 shows the absolute values of  $\sqrt{X}$  and the most useful low-order KP(m,n) approximant operators with respect to  $X$ . It is shown that the approximations KP(m,n) are a good fit to the exact solution of the scalar Helmholtz equation. Furthermore, it is clearly seen that the higher the order of the approximation KP(m,n) is, the more accurate approximation to Helmholtz propagator is. The same figure also shows the approximant of this propagator using the conventional [3] and modified Padé approximant operators [1].

It is obvious that the resulting method allows more accurate approximation to the Helmholtz propagator in a wide range of  $X$  than the previous approaches even with the modified Padé operators. However, if the denominator of the approximation KP(m,n) formula approaches zero, its absolute value approaches  $\infty$  as clearly seen in Fig. 3.17. Physically, the resulting method correctly models waves propagating in the propagating region where  $X \geq 0$  whereas it incorrectly

models waves propagating in the evanescent region where  $X < 0$ . To circumvent this problem, the rotation technique of the square-root operator in the complex plane to address the evanescent waves proposed by Milinazzo *et al.* [19] is employed. The rotation technique is done using a rotation angle of  $\theta$  as follows:

$$\sqrt{X} = \sqrt{Xe^{-j\theta}e^{j\theta}} = e^{j\theta/2}\sqrt{Z}. \quad (3.31)$$

where  $Z=Xe^{-j\theta}$ . From Fig. 3.17, it is clearly shown that the rotated KP(1,1) with  $\theta=\pi/4$  could give the evanescent wave the desired damping and allow a good approximation to the true Helmholtz equation.

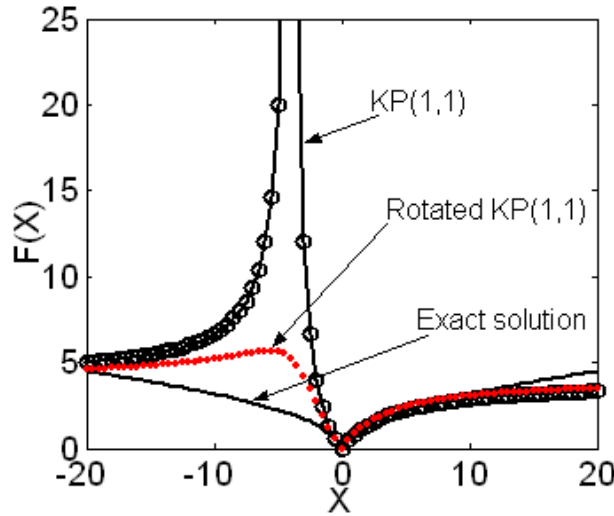


Figure 3.17. The absolute values of  $X^{1/2}$  (solid line), the first-order (solid line with circles) and rotated (dotted line) KP(1,1) approximant of  $X^{1/2}$ .

### III.2.3. Example

In order to prove the applicability and the accuracy of this method, it is employed to study 2D and 3D optical waveguide problems whereby the wide-angle beam propagation is needed. We compare the results with those obtained by the existing approach. For the 2D case, a Y-junction waveguide is considered. The parameters needed for calculations are same as in [20]. The fundamental mode for the slab of width  $w = 0.2 \mu\text{m}$  after propagating through  $21 \mu\text{m}$  at wavelength  $\lambda = 0.633 \mu\text{m}$  calculated by Padé-based and our approach is depicted in Fig. 3.18.

For the 3D case, we investigate the guided-mode propagation in the Y-branch rib waveguide from [1]. The initial rib waveguide is split into two 10-degree tilted waveguides. The fundamental mode of the ridge waveguide of width  $w = 2 \mu\text{m}$  for polarization TE mode at  $0.633\text{-}\mu\text{m}$  wavelength is used as the excited field at  $z = 0$ . The field pattern at  $z = 3 \mu\text{m}$  calculated by

Padé-based and our approach is depicted in Fig. 3.19. It is seen that the calculated results by the resulting method are in good agreement with those obtained by the Padé-based approach. Although for modeling these structures the improvement of the resulting approach compared to the Padé-based one in terms of accuracy is not too much, in terms of execution speed it can show a significant improvement. To implement WA propagation based on these operators, we used the recently introduced complex Jacobi iterative (CJI) method. The reason of choice is due to the rapid convergence of CJI compared to other state-of-the-art matrix solvers. Details of benchmark tests will be presented in Chapter V. The execution speed of CJI is dominated by the amount of effective absorption (or medium loss) in the propagation equation. If the medium loss is high, the convergence rate is thus fast. Since the medium loss occurred in the propagation equation based on KP(1,1) is higher than that of the conventional Padé(1,1) but smaller than the modified Padé-based one for a small propagation step size, the CJI method for KP(1,1)-based BPM offers more rapid convergence than the conventional Padé(1,1)-based one but slower than the modified one. For details of this, we refer the reader to Ref. [18].

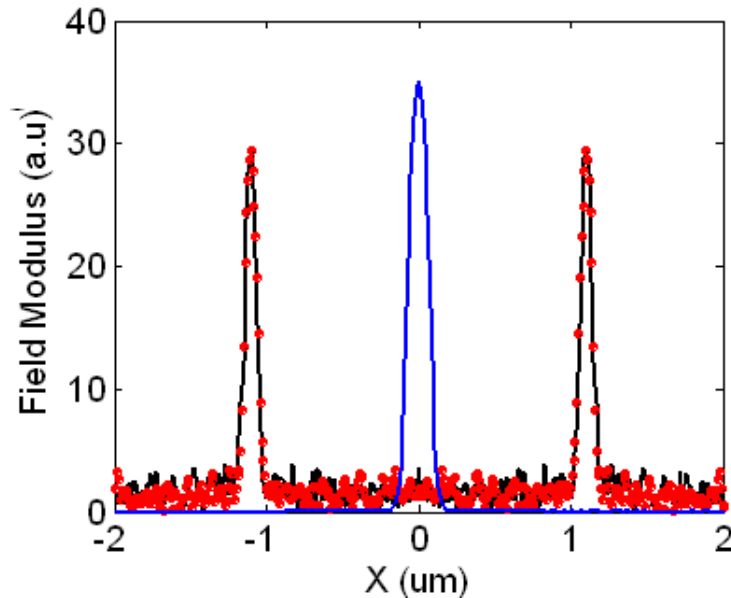


Figure 3.18. Input beam at  $z = 0$  (blue solid line) and output beam at  $z = 21 \mu\text{m}$  in 2D Y-branch rib waveguide calculated by WA-BPM based on KP(1,1) (black solid line) and conventional Padé(1,1) (red circles).

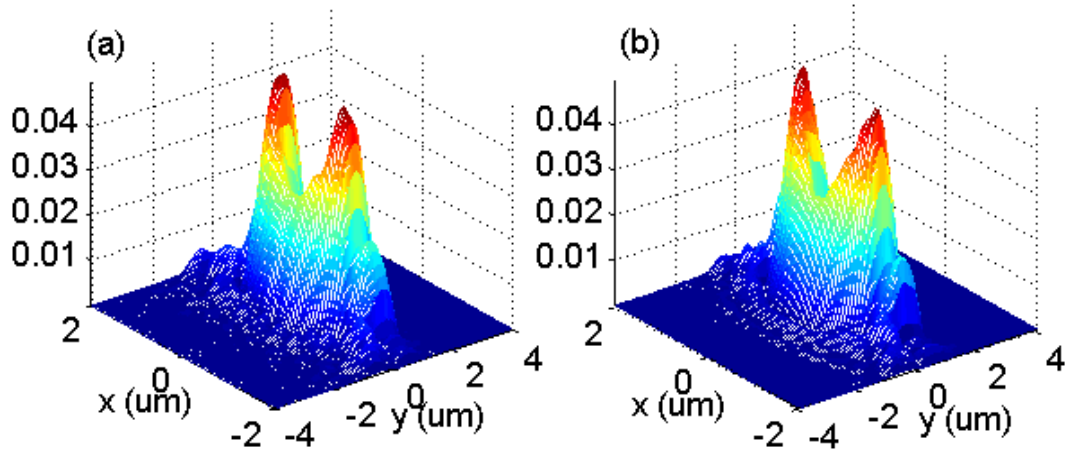


Figure 3.19. Magnitude of TE fundamental mode after propagating  $3 \mu\text{m}$  in 3D Y-branch rib waveguide calculated by WA-BPM based on (a) KP(1,1) and (b) conventional Padé(1,1).

### III.3. Conclusion

In this chapter, new approximant operators resulting in the so-called modified Padé operators for WA-BPMs have been presented. The resulting operators not only allow more accurate approximations to the true Helmholtz equation, but also give evanescent modes the desired damping. To demonstrate the benefits of using the modified operator, an example of analysis of a  $1 \times 4$  MMI coupler has been done. It was shown that the modified operator can offer the advantages of using larger propagation step sizes with an associated reduction of computational efforts compared to the conventional operator. The modified Padé operators have also been applied for the recently introduced generalized rectangular WA-BPMs. The resulting method could be performed with a lower loss of accuracy in terms of energy conservation than the standard finite difference WA-BPM.

Furthermore, the modified Padé operators have been extended to the solution of wideband time-domain wide-angle beam propagation methods. These modified propagators are promising for more accurate approximation to the time-domain wave equation than conventional approximant operators. Via certain examples chosen here, we showed this both for the propagation of an optical beam in a grating, as well as for the propagation of ultrashort pulses in wide-angle waveguides. In both cases, similar accuracy as compared to the traditional method was obtained, but with much larger step size.

In addition, the resulting TD-BPM based on the modified Padé(1,1) operator combined with other existing time-domain techniques including TLM and GNLSE have been employed to study the excitation of a nonlinear planar waveguide by a non-stationary light beam. TLM was already established as a rigorous technique to model transmitted and reflected beams. However, it requires a very small time step (Courant condition) and thus significant computational effort is needed. The TD-BPM provides an attractive alternative numerical technique for nonlinear optical analysis and even with a Padé(1,1) approximation in time gives a good improvement over the GNLSE-based approach.

Apart from the modified Padé operators for solution of WA-BPMs under SVEA, new approximant operators towards WA-BPMs without using the SVEA have been proposed. The resulting method allows more accurate approximations to the true Helmholtz equation than the conventional and modified Padé approximant-based approach in a wide range of operator. In contrast to existing methods, no slowly varying field approximations are assumed, so that WA formulations are completely general.

# References

1. Khai Q. Le, R. G. Rubio, P. Bienstman, and G. R. Hadley, "The complex Jacobi iterative method for three-dimensional wide-angle beam propagation," *Opt. Express* **16**, 17021-17030 (2008).
2. Y. Y. Lu, "A complex coefficient rational approximation of  $\sqrt{1+x}$ ," *Appl. Numer. Math.* **27**, 141-156 (1998).
3. G. R. Hadley, "Wide-angle beam propagation using Padé approximant operators," *Opt. Lett.* **17**, 1426-1428 (1992).
4. Y. Shi and D. Dai, "Design of a compact multimode interference coupler based on deeply etched SiO<sub>2</sub> ridge waveguides," *Opt. Commun.* **271**, 404-407 (2007).
5. T. V. Yioultsis, G. D. Ziogos, and E. E. Kriezis, "An explicit finite-difference vector beam propagation method based on the iterated Crank-Nicolson scheme," *J. Opt. Soc. Am. A* **26**, 2183-2191 (2009).
6. D. Z. Djurdjevic, T. M. Benson, P. Sewell, and A. Vukovic, "Fast and accurate analysis of 3D curved optical waveguide couplers," *J. Lightwave Technol.* **22**, 2333-2340 (2004).
7. T. M. Benson, P. Sewell, S. Sujecki, and P. C. Kendall, "Structure related beam propagation," *Opt. Quantum Electron.* **31**, 689-793 (1999).
8. G. R. Hadley, "Slanted-wall beam propagation," *J. Lightwave Technol.* **25**, 2367-2375 (2007).
9. S. Sujecki, "Wide-angle, finite-difference beam propagation in oblique coordinate system," *J. Opt. Soc. Am. A* **25**, 138-145 (2007).
10. S. Sujecki, "Generalized rectangular finite difference beam propagation," *Appl. Opt.* **47**, 4280-4286 (2008).
11. Khai Q. Le and P. Bienstman, "Fast three-dimensional generalized rectangular wide-angle BPM using complex Jacobi iteration," *J. Opt. Soc. Am. B* **26**, 1469-1472 (2009).
12. Khai Q. Le, T. M. Benson, and P. Bienstman, "Application of modified Padé approximant operators to time-domain beam propagation methods," *J. Opt. Soc. Am. B* **26**, 2285-2289 (2009).
13. J. J. Lim, T. M. Benson, E. C. Larkins and P. Sewell, "Wideband finite-difference-time-domain beam propagation method," *Opt. Microwave Technol. Lett.* **34**, 243-246 (2002).

14. Khai Q. Le, H. G. Dantanarayana, E. A. Romanova, T. M. Benson, and P. Bienstman, "Comparative Assessment of Time-Domain Models of Nonlinear Optical Propagation," 3<sup>rd</sup> ICTON-MW, France, (2009).
15. E. A. Romanova, V. Janyani, A. Vukovic, P. Sewell, and T. M. Benson, "Models of nonlinear waveguide excitation by non-stationary light beam," *Opt. Quantum. Electron.* **39**, 813-823 (2007).
16. J. Shibayama, A. Yamahira, T. Mugita, J. Yamauchi, and H. Nakano, "A finite-difference time-domain beam-propagation method for TE- and TM-wave analyses," *J. Lightwave Technol.* **21**, 1709-1715 (2003).
17. T. Fujisawa, and M. Koshiba, "Time-domain beam propagation method for nonlinear optical propagation analysis and its application to photonic crystal circuits," *J. Lightwave Technol.* **22**, 684-691 (2004).
18. Khai Q. Le and P. Bienstman, "Wide-angle beam propagation method without using slowly varying envelope approximation," *J. Opt. Soc. Am. B* **26**, 353-356 (2009).
19. F. A. Milinazzo, C. A. Zala, and G. H. Brooke, "Rational square root approximations for parabolic equation algorithms," *J. Acoust. Soc. Am.* **101**, 760-766 (1997).
20. Z. Ju, J. Fu and E. Feng, "A simple wide-angle beam-propagation method for integrated optics," *Microwave Opt. Technol. Lett.* **14**, 345-347 (1997).

# Chapter IV

## Iterative Helmholtz solvers for solution of beam propagation

The Helmholtz equation has found many applications in several important fields including acoustics and electromagnetics. It occurs repeatedly in the description of all problems involving the propagation of sound waves in water, and the propagation of light through a dielectric medium. Therefore, the ability to solve the Helmholtz equation efficiently is very important. Practical problems commonly require to be simulated in three-dimensional (3D) structures with complicated material geometries and/or problem boundaries. However the grid size for such problems is restricted to some fraction of the wavelength, and thus 3D problems usually result in matrix equations too large to be solvable by traditional direct matrix inversion (DMI). Indeed, DMI is very slow and requires a large amount of memory. Alternative techniques for DMI have thus been the subject of intense research. The traditional counterpart for direct methods is iterative methods, which have low memory requirements. Among modern iterative methods are the collection of Krylov subspace iterative methods, multigrid methods and domain decomposition methods [1-2]. These techniques aim at minimizing some function of the residual vector in an optimal manner. For Krylov subspace methods there exist two well-known methods including the generalized minimum residual (GMRES) [3] and bi-conjugate gradient stabilized (Bi-CGSTAB) method [4]. While these two techniques are very efficient and fast, and require less memory than the traditional DMI, they tend to be complicated and difficult to implement. In many cases seeking a good preconditioner is a requirement for convergence. Even with a suitable preconditioner they are not always guaranteed to result in a satisfactory convergence. This therefore adds substantially to the burden of the modeler.

Recently, the complex Jacobi iterative (CJI) method, a new iterative technique for solution of the indefinite Helmholtz equation, was introduced [5]. It is based on a complex generalization of the point relaxation technique proposed by Jacobi in 1845, and has been shown to converge at a rate dependent only upon the grid size and effective absorption coefficient.

In this chapter, these advanced iterative methods aimed at solving the Helmholtz problems are reviewed. Subsequently, we present the adaptation of these methods for a solution of one of the most widely used propagation techniques for the study of light propagation in optical waveguide devices.

## IV.1. The Helmholtz equation

The formulation of the Helmholtz equation is done by considering the general time-dependent wave equation [6]:

$$\frac{\partial^2 u(r, t)}{\partial t^2} - \frac{1}{c^2} \nabla^2 u(r, t) = 0, \quad (4.1)$$

where  $c$  is the speed of light in free space. By assuming waves that are periodic in time according to an  $\exp(-i\omega t)$  dependency we obtain the following equation:

$$-\nabla^2 u(r) - k^2 u(r) = 0, \quad (4.2)$$

where  $k = \omega/c$  is the wavenumber,  $\omega = 2\pi f$  is the angular frequency, and  $f$  is the frequency in Hertz. The resulting Eq. (4.2) is called the Helmholtz equation. In a more general formulation, a source term can be included in the right-hand side of Eq. (4.1). In this case, with the time-harmonic wave assumption the relevant Helmholtz equation is given by

$$-\nabla^2 u(r) - k^2 u(r) = g(r), \quad (4.3)$$

with  $g(r)$  being the source term. From this equation, many numerical solution techniques have been proposed. In this work, only the iterative Krylov subspace methods and the recently developed complex Jacobi iterative method are considered.

For discretization of the Helmholtz equation either finite difference or finite element schemes can be used. They result in a linear system as follows:

$$Au = g, \quad A \in \mathbb{C}^{N \times N} \quad (4.4)$$

where  $N$  is the number of unknowns. In some cases of absorbing boundary conditions (like PML) included in the computation domain the matrix  $A$  is complex-valued but also in the presence of loss or gain.

In the following sections, some iterative methods used to solve the linear system (4.4) are briefly reviewed.

## IV.2. The iterative Krylov subspace methods

The main idea of the Krylov subspace iteration methods is to generate a basis of the Krylov subspace  $\text{Span}\{r^0, Ar^0, A^2r^0, \dots, A^{m-1}r^0\}$  and iteratively seek an approximate solution to the original problem from this subspace in the form

$$K^m(A, r^0) = \text{Span}\{r^0, Ar^0, A^2r^0, \dots, A^{m-1}r^0\}, \quad (4.5)$$

where  $r^0 := g - Au^0$  is the initial residual related to the initial guess  $u^0$ . The dimension of  $K^m$  is equal to  $m$  and increases by one at each step of the approximation process. More specifically, the idea of Krylov subspace methods can be outlined as follows [6]:

- + Choose an initial solution  $u^0$
- + Compute an approximate solution  $u^m$  of the form

$$u^m \in u^0 + K^m(A, r^0), \quad m > 1 \quad (4.6)$$

+ Construct the subspace  $K^m$  by the basis  $V^m = [v^1, v^2, \dots, v^m] \in K^m$ . With residual  $r^m := g - Au^m$ , from (4.6) an expression for the residual at the  $m^{\text{th}}$  step is given by

$$r^m = r^0 - AV^m y^m, \quad \text{where } y^m \in \mathbb{C}^N \text{ and } u^m = u^0 + V^m y^m. \quad (4.7)$$

It is seen that the Krylov subspace methods are based on a construction of the basis  $V^m$  and the vector  $y^m$ . Depending on how the basis  $V^m$  and the vector  $y^m$  are constructed, several Krylov subspace methods can be distinguished. Among those methods are well-known methods such as Conjugate Gradients (CG), Bi-CGSTAB, GMRES and minimal residual (MINRES) method [7]. In this chapter, the emphasis is on two well-known methods GMRES and Bi-CGSTAB.

### IV.2.1. GMRES

In the GMRES (generalized minimum residual) the basis of the Krylov subspace  $K^m(A, r^0)$  is obtained using Arnoldi's method [8]. This is a modified Gram-Schmidt method [9] to compute an  $l_2$ -orthonormal basis  $\{v^1, v^2, \dots, v^m\}$  of the Krylov subspace  $K^m(A, r^0)$  and can be described as follows [7]:

1. Start: Choose an initial vector  $v^1$  with  $\|v^1\|=1$
2. Iterate: For  $j=1, 2, \dots, m$  do:

$$\text{Compute } w^j := Av^j$$

For  $i=1, 2, \dots, j$  do

$$h^{ij} := (w^j, v^i)$$

$$w^j := w^j - h^{ij}v^i$$

Enddo

$h^{j+1,j} = \|w^j\|_2$ , if  $h^{j+1,j} = 0$ , stop

$v^{j+1} = w^j / h^{j+1,j}$

Enddo.

Prior to revisiting the GMRES algorithm we should notice that if  $V^m$  is the  $(N \times m)$  matrix whose columns are the  $l_2$ -orthonormal basis  $\{v^1, v^2, \dots, v^m\}$ , then  $H^m = (V^m)^T A V^m$  is the upper  $(m \times m)$  Hessenberg matrix whose entries are the scalars  $h^{ij}$  generated by Arnoldi's method. After  $m$  steps of this method we obtain an  $l_2$ -orthonormal system  $V^{m+1}$  and a  $[(m+1) \times m]$  matrix  $G^m$  whose only nonzero entries are the elements  $h^{ij}$ . It is seen that  $G^m$  is the same as  $H^m$  except for an additional row whose only nonzero element is  $h^{m+1,m}$  in the  $(m+1, m)$  position. Furthermore, the following relation between the vector  $V^m$  and the matrix  $G^m$  holds:

$$A V^m = V^{m+1} G^m. \quad (4.8)$$

The implementation of the GMRES algorithm can be outlined as follows. For an initial value  $u^0$ , any vector  $u$  in  $u^0 + K^m$  can be written as

$$u = u^0 + V^m y, \quad (4.9)$$

where  $y$  is an  $m$ -vector. For seeking a final solution, the following least squares problem will be solved:

$$\min \|g - A(u^0 + V^m y)\| = \min \|r^0 - A V^m y\|, \text{ with } V^m y \in K^m. \quad (4.10)$$

By defining the norm as the following function of  $y$ , we can see it to be minimized

$$\begin{aligned} J(y) &= \|g - Au\|_2 = \|g - A(u^0 + V^m y)\|_2 \\ &= \|r^0 - A V^m y\|_2. \end{aligned} \quad (4.11)$$

The relation (4.8) results in

$$J(y) = \|\beta v^1 - V^{m+1} G^j y\|_2 = \|V^{m+1} (\beta e^1 - G^m y)\|_2 \quad (4.12)$$

where  $\beta = \|r^0\|$  and  $e^1$  is the first column of the  $[(m+1) \times (m+1)]$  identity matrix. Since the column-vectors of  $V^{m+1}$  are  $l_2$ -orthonormal, the following formula is obtained

$$J(y) = \|(\beta e^1 - G^m y)\|_2. \quad (4.13)$$

The GMRES approximation is the unique vector of  $u^0 + K^m$  which minimizes the function  $J(y)$ . Hence the solution of the least squares problem (4.10) is given by

$$u^m = u^0 + V^m y^m \quad (4.14)$$

where  $y^j$  minimizes the function  $J(y)$ . This leads to the GMRES algorithm as follows [3]:

1. Start: Choose an initial  $u^0$  and compute  $r^0 = g - Au^0$ ,  $\beta = \|r^0\|$ ,  $v^1 = r^0 / \beta$ .

Define the  $(m+1) \times m$  matrix  $G^m = \{h^{ij}\}_{1 \leq i \leq m+1, 1 \leq j \leq m}$ . Set  $G^m = 0$ .

2. Iterate: For  $j=1, 2, \dots, m$  do:

Compute  $w^j := Av^j$

For  $i=1, 2, \dots, j$  do:

$h^{ij} := (w^j, v^i)$

$w^j := w^j - h^{ij}v^i$

Enddo

$h^{j+1,j} = \|w^j\|_2$ , if  $h^{j+1,j} = 0$ , set  $m:=j$  and go to step 3

$v^{j+1} = w^j / h^{j+1,j}$

Enddo.

3. Form the approximate solution:

Compute  $y^m$  the minimizer of  $\|(\beta e^1 - G^m y)\|_2$  and  $u^m = u^0 + V^m y^m$ .

## IV.2.2. Bi-CGSTAB

One of the competitive methods with the GMRES method to solve nonsymmetric systems is Bi-CGSTAB (bi-conjugate gradient stabilized). It is an improved variant of the conjugate gradients-squared (CG-S), another attractive variant of the bi-conjugate gradients (Bi-CG) method [4]. The CG-S algorithm is based on squaring the residual polynomial, and, in case of irregular convergence, this may lead to substantial build-up of rounding errors, or possibly even overflow. In order to overcome this difficulty the Bi-CGSTAB algorithm was developed. In the following text, we try to briefly present the algorithm and further information can be found in [4].

Instead of computing the CG-S sequence of iterates whose residual norms  $r^i = [P_i(A)]^2 r^0$ , the Bi-CGSTAB computes

$$r^i = Q_i(A)P_i(A)r^0, \quad (4.15)$$

where  $P_i(A)$  is the residual polynomial associated with the Bi-CG algorithm, which satisfies the recurrence relation

$$P_i(A)r^0 = [P_{i-1}(A) - \alpha_i A T_{i-1}(A)]r^0 \quad (4.16)$$

with

$$T_i(A)r^0 = [P_i(A) + \beta_{i+1} T_{i-1}(A)]r^0, \quad (4.17)$$

and  $Q_i(A)$  is a new polynomial which is defined recursively at each step aimed at stabilizing or smoothing the convergence behavior of the Bi-CG algorithm as:

$$Q_i(A) = (1 - \omega_1 A)(1 - \omega_2 A) \dots (1 - \omega_i A) \quad (4.18)$$

with  $\omega_i$  suitable constants to be selected. At each  $i^{\text{th}}$  step it is an obvious possibility to select  $\omega_i$  to minimize  $r^i$ .

With (4.18) and the Bi-CG relation for the factor  $P_i(A)$  and  $T_i(A)$  in (4.16) and (4.17), we obtain

$$\begin{aligned} Q_i(A)P_i(A)r^0 &= (1 - \omega_i A)Q_{i-1}(A)[P_{i-1}(A) - \alpha_i A T_{i-1}(A)]r^0 \\ &= [Q_{i-1}(A)P_{i-1}(A) - \alpha_i A Q_{i-1}(A)T_{i-1}(A)]r^0 - \omega_i A [Q_{i-1}(A)P_{i-1}(A) - \alpha_i A Q_{i-1}(A)T_{i-1}(A)]r^0. \end{aligned} \quad (4.19)$$

Obviously, in order to compute (4.19) a relation for the following product is needed

$$\begin{aligned} Q_i(A)T_i(A)r^0 &= Q_i(A)[P_i(A) + \beta_{i+1} T_{i-1}(A)]r^0 \\ &= Q_i(A)P_i(A)r^0 + \beta_{i+1}(1 - \omega_i A)Q_{i-1}(A)T_{i-1}(A)r^0, \end{aligned} \quad (4.20)$$

as well as the Bi-CG constants  $\alpha_i$  and  $\beta_i$  need to be recovered. According to the Bi-CG algorithm, we have  $\beta_i = \rho_{i+1}/\rho_i$  with  $\rho_i = (P_i(A)r^0, P_i(A^T)\check{r}^0) = (P_i(A)^2 r^0, \check{r}^0)$ .

However, since none of the vectors  $P_i(A)r^0$ ,  $P_i(A^T)\check{r}^0$  or  $P_i(A)^2 r^0$  are available,  $\rho_i$  is not computable. Fortunately,  $\rho_i$  can be related to the scalar

$$\tilde{\rho}_i = (P_i(A)r^0, Q_i(A^T)\check{r}^0) \quad (4.21)$$

which is computable via  $\tilde{\rho}_i = (P_i(A)r^0, Q_i(A^T)\check{r}^0) = (Q_i(A)P_i(A^T)r^0, \check{r}^0) = (r^0, \check{r}^0)$ .

To relate the two scalars  $\rho_i$  and  $\tilde{\rho}_i$ , expand  $Q_i(A^T)\check{r}^0$  explicitly in the power basis to obtain

$$\tilde{\rho}_i = (P_i(A)r^0, \eta_1^{(i)}(A^T)^i \check{r}^0 + \eta_2^{(i)}(A^T)^{i-1} \check{r}^0 + \dots). \quad (4.22)$$

Since  $P_i(A)r^0$  is orthogonal to all vectors  $(A^T)^k \check{r}^0$  with  $k < i$ , only the leading power is relevant in the expansion on the right hand side of (4.22). In particular, if  $\gamma_1^{(i)}$  is the leading power coefficient for the polynomial  $P_i(A)$ , then

$$\tilde{\rho}_i = (P_i(A)r^0, [\eta_1^{(i)}/\gamma_1^{(i)}]P_i(A^T)\check{r}^0) = [\eta_1^{(i)}/\gamma_1^{(i)}] \rho_i, \quad (4.23)$$

where leading coefficients are found to satisfy the following relations:

$$\eta_1^{(i+1)} = -\omega_i \eta_1^{(i)}, \quad \gamma_1^{(i+1)} = -\alpha_i \gamma_1^{(i)}, \quad (4.24)$$

and it results in

$$\frac{\tilde{\rho}_{i+1}}{\tilde{\rho}_i} = \frac{\omega_i}{\alpha_i} \frac{\rho_{i+1}}{\rho_i} \quad (4.25)$$

and

$$\beta_i = \frac{\tilde{\rho}_{i+1}}{\tilde{\rho}_i} \frac{\alpha_i}{\omega_i}. \quad (4.26)$$

Similarly, a recurrence relation for the constant  $\alpha_i$  can be derived. By defining  $p^i = Q_i(A)T_i(A)r^0$  associated with  $r^i$  in (4.15), these vectors can be updated from a double recurrence with provided  $\alpha_i$  and  $\beta_i$ . This recurrence is

$$\begin{aligned} r^{i+1} &= (1 - \omega_i A)(r^i - \alpha_i A p^i), \\ p^{i+1} &= r^{i+1} + \beta_i(1 - \omega_i A) p^i. \end{aligned} \quad (4.27)$$

With the leading coefficients for  $P_i(A^T)\tilde{r}^0$  and  $T_i(A^T)\tilde{r}^0$  are identical, the constant  $\alpha_i$  is defined by

$$\alpha_i = \tilde{\rho}_i / (A p^i, \tilde{r}^0). \quad (4.28)$$

Next, the parameter  $\omega_i$  must be chosen to minimize  $r^i$  in (4.15). Equation (4.27) can be rewritten as

$$r^{i+1} = (1 - \omega_i A)s^i \text{ with } s^i = r^i - \alpha_i A p^i \quad (4.29)$$

Then the optimal value of  $\omega_i$  is given by

$$\omega_i = \frac{(As^i, s^i)}{(As^i, As^i)}. \quad (4.30)$$

With the constants  $\alpha_i$  and  $\beta_i$  and the parameter  $\omega_i$  is computed, we can obtain a formula to update the approximate solution  $u^{i+1}$  from  $u^i$  as follows.

Equation (4.27) can be rewritten as

$$r^{i+1} = s^i - \omega_i A s^i = r^i - \alpha_i A p^i - \omega_i A s^i \quad (4.31)$$

which results in

$$u^{i+1} = u^i + \alpha_i p^i + \omega_i s^i. \quad (4.32)$$

Finally, with the above relations the Bi-CGSTAB algorithm can be given as follows [4]:

1. Start: Choose an initial guess  $u^0$  and an arbitrary vector  $\tilde{r}^0$ .

Compute  $r^0 = g - Au^0$ .

Set  $\rho_0 = \alpha = \omega_0 = 1$ ;  $v^0 = p^0 = 0$ ;

2. Iterate: For  $j=1, 2, \dots$ , until convergence do:

$\rho_j = (\tilde{r}^0, r^{j-1})$ ;  $\beta = (\rho_j / \rho_{j-1}) / (\alpha / \omega_{j-1})$ ;

$p^j = r^{j-1} + \beta(p^{j-1} - \omega_{j-1}v_{j-1})$ ;

$v_j = Ap^j$ ;

$$\begin{aligned} \alpha &= \rho_j / (\tilde{r}^0, v_j); \\ s &= r^{j-1} - \alpha v_j; \\ t &= A s; \\ \omega_j &= (t, s) / (t, t); \\ u^j &= u^{j-1} + \alpha p^j + \omega_j s; \\ \text{if } u^j &\text{ is accurate enough then quit;} \\ r^j &= s - \omega_j t; \end{aligned}$$

Enddo.

### IV.2.3. Application in beam propagation

In order to implement the WA beam propagation method based on Padé approximant operators, an implicit finite-difference method based on the well-known Crank-Nicholson scheme has become the most commonly used approach. In this implementation, the field in the transverse ( $xy$ ) plane is represented by discrete points on a grid, and discrete planes along the propagation direction ( $z$ ) (see figure 4.1). Given the discretized field at a certain discrete plane  $z$ , the goal is to derive numerical equations to determine the field at the next discrete plane  $z + \Delta z$ . The elementary propagation step is then repeated to calculate the field throughout the waveguide structure.

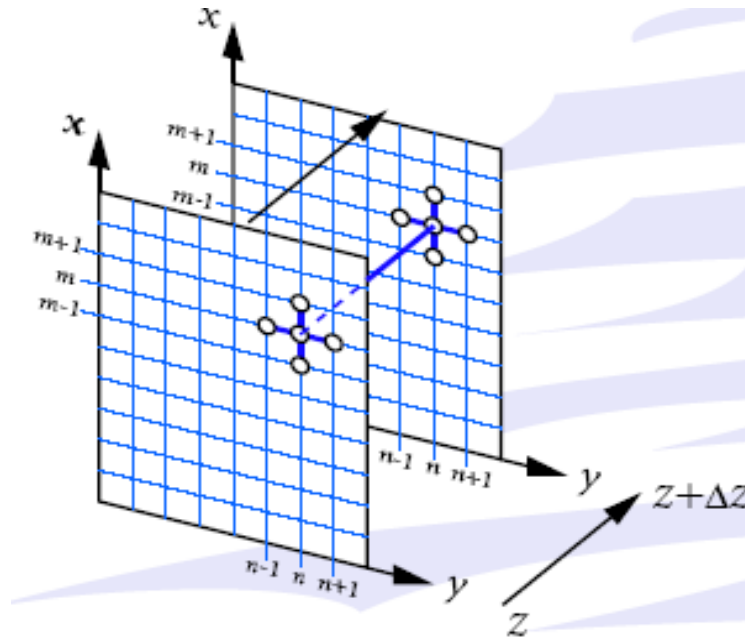


Figure 4.1. Discrete planes along propagation direction.

As an example to show how GMRES and Bi-CGSTAB can be employed in beam propagation, the most widely used WA-BPM based on the simplest Padé(1,1) operator is considered. Then, the scalar 3D propagation equation is given by [10]

$$(1 + \xi P)\phi^{n+1} = (1 + \xi^* P)\phi, \quad (4.33)$$

where  $\xi = 1/4k^2 - i\Delta z/4k$ ,  $\xi^*$  is the complex conjugate of  $\xi$  and  $\Delta z$  is the propagation step.

By discretizing Eq. (4.33), the following matrix system is obtained

$$\begin{aligned} A_{n+1}\phi_{i+1,j}^{n+1} + B_{n+1}\phi_{i-1,j}^{n+1} + C_{n+1}\phi_{i,j}^{n+1} + D_{n+1}\phi_{i,j-1}^{n+1} + E_{n+1}\phi_{i,j+1}^{n+1} \\ = A_n\phi_{i+1,j}^n + B_n\phi_{i-1,j}^n + C_n\phi_{i,j}^n + D_n\phi_{i,j-1}^n + E_n\phi_{i,j+1}^n \end{aligned} \quad (4.34)$$

where

$$\begin{aligned} A_{n+1} = B_{n+1} &= \frac{1}{\Delta x^2}, & D_{n+1} = E_{n+1} &= \frac{1}{\Delta y^2}, \\ C_{n+1} &= k_o^2(n^2 - n_{ref}^2) + \frac{1}{\xi} - 2\left(\frac{1}{\Delta x^2} + \frac{1}{\Delta y^2}\right), \\ A_n = B_n &= \frac{\xi^*}{\xi} \frac{1}{\Delta x^2}, & D_n = E_n &= \frac{\xi^*}{\xi} \frac{1}{\Delta y^2}, \\ C_n &= \frac{\xi^*}{\xi} \left( k_o^2(n^2 - n_{ref}^2) + \frac{1}{\xi^*} - 2\left(\frac{1}{\Delta x^2} + \frac{1}{\Delta y^2}\right) \right) \end{aligned} \quad (4.35)$$

This equation is a  $M^2$  by  $M^2$  matrix equation for a M by M mesh grid. However, each row of the coefficient matrix has no more than five non-zero values. As a result, this sparse matrix equation can be efficiently solved using GMRES and Bi-CGSTAB. More results and benchmarks on these methods will be presented in the next chapter.

## IV.3. CJI

### IV.3.1. Formulation

As stated in the beginning of this chapter, the CJI method was introduced by Hadley in 2005 [5]. Before going to the formulation of this method, it is better to look back to the basic iterative method for solving the linear system (4.4) which is fixed-point iteration based on the splitting of the system matrix:

$$A = F - G, \quad F, G \in \mathbb{C}^{N \times N}. \quad (4.36)$$

Substituting this equation into Eq. (4.4) results in

$$(F - G)u = g \iff Fu = g + Gu. \quad (4.37)$$

Eq. (4.37) suggests a basic iteration scheme to find the new approximation  $u^j$  after the  $(j-1)^{\text{th}}$  iteration with a given  $u^{j-1}$  as follows:

$$Fu^j = g + Gu^{j-1} \implies u^j = F^{-1}(g + Gu^{j-1}). \quad (4.38)$$

Thus, the matrix form of Eq. (4.38) can be given by

$$\begin{aligned} u^j &= F^{-1}g + (I - F^{-1}A)u^{j-1} \\ &= u^{j-1} + F^{-1}r^{j-1}, \end{aligned} \quad (4.39)$$

with  $r^{j-1} = g - Au^{j-1}$  being the residual after the  $(j-1)^{\text{th}}$  iteration and  $I$  being the identity matrix. Eq. (4.39) is called the basic iterative method, and it is convergent if  $u^j = u^{j-1}$ , meaning that  $r^{j-1} = 0$  [6].

Depending on the system matrix is split, we can distinguish different types of methods. If the splitting is done by  $A = D - E$ , with  $D = \text{diag}(A)$ , we obtain the Jacobi iterative method:

$$u^j = u^{j-1} + D^{-1}r^{j-1}. \quad (4.40)$$

To improve the convergence of the fixed-point iteration, a relaxation factor  $\alpha$  was introduced in [11]. It results in the standard Jacobi iteration given by

$$u^j = u^{j-1} + \alpha^{-1}D^{-1}r^{j-1}. \quad (4.41)$$

However, for indefinite Helmholtz problems the standard Jacobi iteration is not convergent. It is seen by analyzing the amplitude of Fourier modes between two successive iterations that there are no values of  $\alpha$  for which the residual error is reduced during the iterations. This can be remedied by using pairs of Jacobi steps with two difference relaxation factors  $\alpha$ , which also have a complex value. The resulting complex Jacobi iterative method is given by

$$\begin{aligned} u^{j-1/2} &= u^{j-1} + \alpha_1^{-1}D^{-1}r^{j-1}, \\ u^j &= u^{j-1/2} + \alpha_2^{-1}D^{-1}r^{j-1/2}. \end{aligned} \quad (4.42)$$

where  $\alpha_2 = -\alpha_1^*$ . To satisfy the convergent criteria it is required that  $\text{Im}(\alpha_1) < 0$ . It is found that the highest convergence rate is obtained if  $\alpha_1 = \sqrt{3} - 1i$  [5].

### IV.3.2. Example

In recent years, the CJI method has been employed to study guided-wave devices. It is applied to investigate light propagation in planar waveguides and grating couplers in the SOI platform. The field distribution in such waveguide structures is shown in Fig. 4.2. The waveguide consists of 220 nm silicon core embedded on 1  $\mu\text{m}$  silica ( $\text{SiO}_2$ ) cladding. They are integrated on top of silicon substrate. The grating has an etched deep of 70 nm and the filling factor (or duty cycle) of 0.5. The grating period is set to 0.6117  $\mu\text{m}$ . Simulations in Fig. 4.2 are done in 2D.

In addition, the CJI method has been extended to study propagation in nonlinear media. It can allow simulating structures with the instantaneous Kerr nonlinear effect in a straight forward manner by simply using an extra step to update the refractive index profile of the nonlinear

media at each iteration step [12]. While the CJI method is very simple and easy to implement, the convergence rate is however still considered to be somewhat slow. For non trivial 2D waveguide structures, it can be very slow in comparison with other existing methods such as BPM, finite-difference time-domain (FDTD) methods or eigenmode expansion (EME) methods. In some cases, it is however very useful for study of waves propagating in lossy media. It is found that the higher loss, the quicker the convergence of CJI will be. Based on this property, the CJI method has found an excellent combination with WA-BPM to result in a powerful tool to study 3D waveguide structures. In the next chapter, the adaptation of CJI for WA-BPMs and the benefits of such a combination are presented.

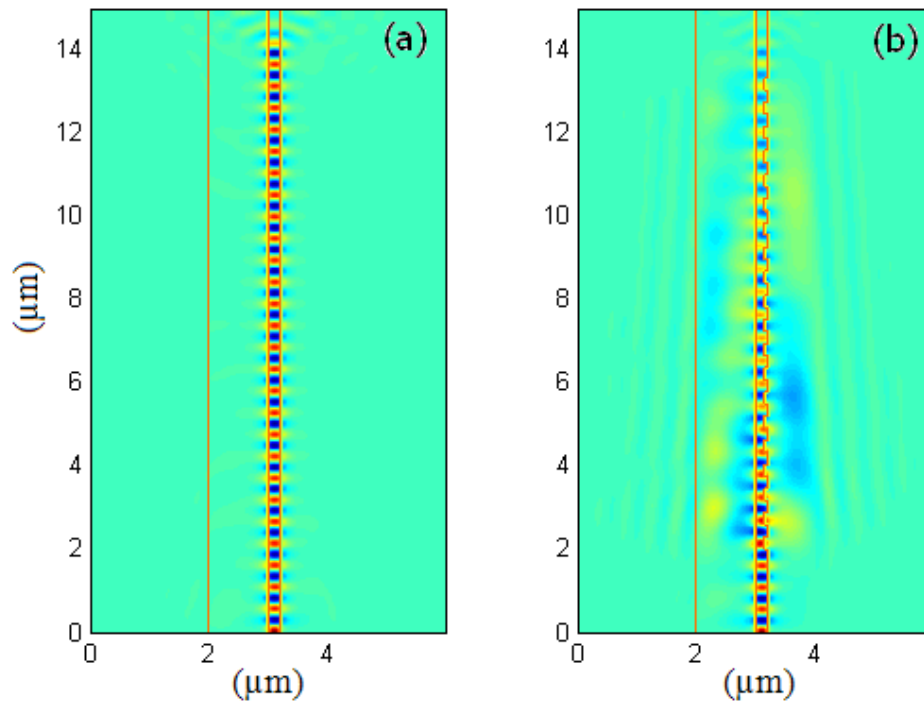


Figure 4.2. Field distribution in planar waveguide (a) and grating coupler (b) in SOI calculated by CJI.

## IV.4. Conclusion

In this chapter, various state-of-the-art iterative methods including GMRES, Bi-CGSTAB and CJI for the solution of the Helmholtz equation have been briefly reviewed. While GMRES and Bi-CGSTAB seem to be very complicated, CJI is very simple and easy to implement. In the next chapter, such methods will be adapted for implementation of beam propagation problems. In order to show the benefits of each method, benchmark tests will be performed.

# References

1. A. Bayliss, C. I. Goldstein, and E. Turkel, "An iterative method for Helmholtz equation," *J. Comput. Phys.* **49**, 443-457 (1983).
2. J. D. Benamou, and B. Despres, "Domain decomposition method for the Helmholtz equation and related optimal control problems," *J. Comput. Phys.* **136**, 62-88 (1997).
3. Y. Saad and M.H. Schultz, "GMRES: A generalized minimal residual algorithm for solving nonsymmetric linear systems", *SIAM J. Sci. Stat. Comput.* **7**, 856-869 (1986).
4. H. A. Van der Vorst, "Bi-CGSTAB: A fast and smoothly converging variant of Bi-CG for the solution of nonsymmetric linear systems," *SIAM J. Sci. Stat. Comput.* **13**, 631-644 (1992).
5. G. R. Hadley, "A complex Jacobi iterative method for the indefinite Helmholtz equation," *J. Comp. Phys.* **203**, 358-370 (2005).
6. Y. A. Erlangga, "Advances in iterative methods and preconditioners for the Helmholtz equation," *Arch. Comput. Methods Eng.* **15**, 37-66 (2008).
7. H. A. Van der Vorst, "Iterative Krylov subspace methods for linear systems," Cambridge University Press, New York (2003).
8. W. E. Arnoldi, "The principle of minimized iteration in the solution of the matrix eigenvalue problem," *Quart. Appl. Math.* **9**, 17-29 (1951).
9. G. W. Stewart, "Introduction to matrix computations," Academic Press, New York (1973).
10. Khai Q. Le, R. G. Rubio, P. Bienstman, and G. R. Hadley, "The complex Jacobi iterative method for three-dimensional wide-angle beam propagation," *Opt. Express* **16**, 17021-17030 (2008).
11. A. Brandt, "Multi-level adaptive solutions to boundary value problems," *Math. Comput.* **31**, 333-390 (1977).
12. P. Vandersteegen, B. Maes, P. Bienstman, and R. Baets, "Using the complex Jacobi method to simulate Kerr non-linear photonic components," *Opt. and Quantum. Electron.* **38**, 35-44 (2006).

# Chapter V

## Three dimensional wide-angle beam propagation using CJI

It was stated earlier that there is lack of efficient BPM tools for design and simulation of 3D waveguide structures. While the Padé-approximant-based WA-BPM is commonly used for modeling 2D optical waveguide structures, it is limited for practical 3D structures due to the lack of efficient solvers.

Several efforts have been done to overcome this issue. A 3D WA-BPM based on Hoekstra's scheme was developed using the efficient Thomas algorithm and the splitting of the 3D Fresnel wave equation into three 2D wave equations [1]. The alternating-direction implicit (ADI) WA-BPM has also recently been developed by E. L. Bekker *et al.* in 2009 [2]. However, this may cause splitting errors. Recently, C. Ma *et al.* [3] presented a new 3D WA-BPM also based on Hoekstra's scheme that does not require the splitting of the Fresnel wave equation or the use of the ADI method. By using a technique for shifting the simulation window to reduce the dimension of the numerical equation and a threshold technique to further ensure its convergence, this approach shows accuracy and effectiveness.

However, the resultant propagation scheme can be very slow with the traditional direct matrix inversion (DMI) methods if the problem size is large. This can be remedied with GMRES or Bi-CGSTAB. However if the structure or the boundary conditions are changing as the propagation proceeds, frequent reinversions of the propagation matrix are required, leading to a very numerically intense solver. Thus, it is imperative to find more efficient solution methods for 3D WA-BPMs.

With the convergence rate depending only upon the grid size and the effective absorption coefficient (or medium loss), the CJI method will be very competitive for demanding problems. As we will see, for beam propagation of waveguide profiles with a 2D cross section, the wide angle beam propagation equation can be recast in terms of a Helmholtz equation with a source

term, and the effective absorption coefficient appearing in this equation is very high, leading to rapid convergence of the CJI method.

In this chapter, the adaptation of the CJI method for beam propagation is done and it is shown to be highly efficient for the solution of large problems, compared to existing matrix solvers. Then, this CJI-WA-BPM is extended to nonlinear propagation problems. Furthermore, higher accuracy of the CJI-WA-BPM is obtained by an implementation of the wide-angle propagation based on higher order Padé operators. Then, the scalar property of CJI-WA-BPM is improved for semivectorial situations in which polarization effects are taken into account. However, for high-index-contrast waveguides the semivectorial CJI-WA-BPM is unstable. This can however be overcome by using an extra algorithm, the iterated Crank-Nicholson method. Finally, the integration of the CJI-WA-BPM into the LightPy framework is presented.

## V.1. Adaptation of CJI for 3D wide-angle beam propagation

### V.1.1. Formulation

By dividing both sides of the 3D beam propagation equation (4.33) by  $\xi$ , it can be written as an inhomogeneous Helmholtz equation

$$(\nabla_{\perp}^2 + k_0^2(n^2 - n_{ref}^2) + \frac{1}{\xi})\phi^{n+1} = (\frac{\xi^*}{\xi}P + \frac{1}{\xi})\phi^n, \quad (5.1)$$

or

$$(\nabla_{\perp}^2 + k_0^2(n^2 - n_{ref}^2) + 4k_0^2n_{ref}^2 \frac{1 + ik\Delta z}{1 + k^2\Delta z^2})\phi^{n+1} = source\ term. \quad (5.2)$$

Thus the 3D propagation equation can be recast as a 2D Helmholtz equation with source term in an effective medium with loss of  $4k_0^2n_{ref}^2 \frac{k\Delta z}{(1 + k^2\Delta z^2)}$ . This loss is high for a typical choice of  $k\Delta z$ , and this is a condition that favors rapid convergence for the CJI method.

Eq. (5.2) is derived using the conventional Padé(1,1) approximant operator. As shown in chapter III, the modified Padé operator can offer much more benefits than the conventional one. In the subsequent section, the usefulness of the modified operator in CJI-WA-BPMs is demonstrated. In this case, the recast Helmholtz equation based on the modified Padé(1,1) operator is given by [4]

$$(\nabla_{\perp}^2 + k_0^2(n^2 - n_{ref}^2) + 4k_0^2 n_{ref}^2 \frac{1 + i[k\Delta z + (1 + k\Delta z\beta/2)\beta/2]}{(1 + k\Delta z\beta/2)^2 + k^2\Delta z^2})\phi^{n+1} = source\ term \quad (5.3)$$

with the corresponding effective medium loss of  $4k_0^2 n_{ref}^2 \frac{k\Delta z + (1 + k\Delta z\beta/2)\beta/2}{(1 + k\Delta z\beta/2)^2 + k^2\Delta z^2}$ .

### V.1.2. Convergence studies of CJI

In this section, the convergence rate of the CJI method for 3D WA-BPM based on the modified and the conventional Padé(1,1) approximant operator is investigated. The simulation of the propagation of a 3D Gaussian beam through a symmetric Y-branch waveguide is carried out. The structure parameters of the Y-branch waveguide are the same as in [5] with  $d_1 = 2 \mu\text{m}$  and  $d_2 = 1 \mu\text{m}$ .

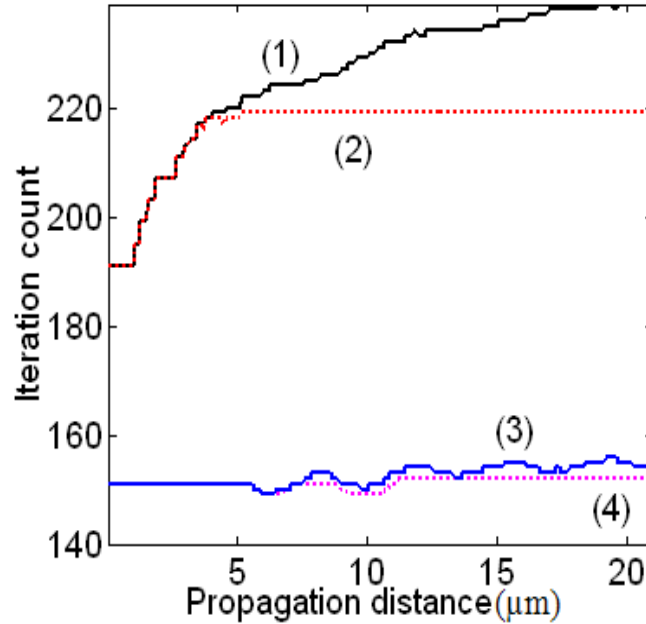


Figure 5.1. The iteration count per propagation step for propagation through a symmetric Y-branch waveguide obtained using the CJI method for standard Padé approximant-based WA BPM without (1) and with (2) PML and the CJI method for the modified Padé without (3) and with (4) PML.

In Fig. 5.1 it is shown that the CJI method requires fewer iterations with WA-BPM based on the modified Padé(1,1) operator than that of the conventional one. This is attributed to the fact that the modified operator gives higher medium loss than the conventional one as seen in Fig. 5.2. However, it suffers from the fact that the iteration count between two successive 2D cross

sections increases throughout the propagation direction. To overcome this problem, we use a perfectly matched layer (PML) as boundary condition, which can absorb incident radiation without any additional parasitic reflections, regardless of wavelength, incident angle or polarization [6-7]. The use of a PML better absorbs scattered radiation and thus lowers the amount of high-spatial-frequency noise scattered back into the problem region. These high spatial frequency components primarily limit the convergence rate of the method, and Fig. 5.1 shows that the CJI technique becomes more stable with the use of a PML.

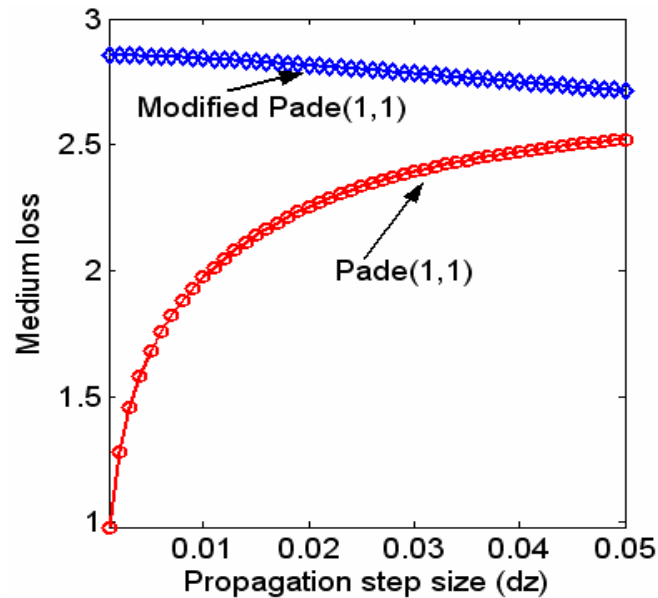


Figure 5.2. Amount of effective absorption in propagation equation with respect to propagation step resolution.

### V.1.3. Benchmark results

This section is dedicated to performing benchmark tests on both 2D and 3D optical waveguide structures employing the WA-BPM using the new CJI, the traditional DMI, GMRES and Bi-CGSTAB method. The simulations were all run on a notebook PC using Matlab. For the 2D case, we consider a 10-degree tilted waveguide [8] and Y-branch waveguide [5]. In the tilted waveguide the fundamental mode for the slab of width  $w = 0.2 \mu\text{m}$  is propagated through  $30 \mu\text{m}$  at wavelength  $\lambda = 1.55 \mu\text{m}$  in a medium of refractive index  $n = 3.4$  with the propagation step size of  $\Delta z = 0.1 \mu\text{m}$ . With a strict propagation error tolerance of  $10^{-6}$  the CJI method only took 34.5 seconds, the GMRES and Bi-CGSTAB took 41.8 and 37.6 seconds, respectively, whereas the DMI method took 241.5 seconds.

In the Y-branch waveguide the parameters needed for calculation are the same as in [5]. With a small propagation step size  $\Delta z = 0.01 \mu\text{m}$  (requiring frequent matrix inversion) the DMI method performed the propagation in 4882 seconds, those for GMRES and Bi-CGSTAB in 982.8 and 1280.1 seconds, respectively, while the CJI method took only 243.5 seconds, more than 4 times faster than these methods. It is obvious that for these 2D waveguide structures the CJI method is faster than DMI, GMRES and Bi-CGSTAB.

For the 3D case, we consider Gaussian beam propagation in a straight rib waveguide [9-10] and guided-mode propagation in a Y-branch rib waveguide. The width and height of the straight rib waveguide are  $w = 2 \mu\text{m}$  and  $h = 1.1 \mu\text{m}$ , as seen in figure 4 of [10]. The guiding core has an index  $n_f = 3.44$  and a thickness  $t = 0.2 \mu\text{m}$  while the refractive index of substrate and cover is  $n_s = 3.34$  and  $n_c = 1$ , respectively. The Gaussian beam with a waist radius  $w_0 = 0.3 \mu\text{m}$  has been injected into the rib waveguide at wavelength  $\lambda = 1.55 \mu\text{m}$ . Due to the large memory required for DMI, the small computational window used of  $2 \times 2 \mu\text{m}$  is discretized with a grid size of  $\Delta x = \Delta y = 0.1 \mu\text{m}$ , and the short path length of  $2 \mu\text{m}$  is discretized with a propagation step size  $\Delta z = 0.1 \mu\text{m}$ . The resulting runtime of DMI is 123 seconds while runtime for CJI is 2.7 seconds and those for GMRES and Bi-CGSTAB are only 0.6 and 0.4 seconds, respectively. This means that for waveguide structures whose refractive index does not change during the propagation direction GMRES and Bi-CGSTAB perform much quicker propagation than CJI and DMI.

For a Y-branch, the initial rib waveguide is split into two 20-degree tilted waveguides as shown in Fig. 5.3. The longitudinal dimension is  $h_1 = 1 \mu\text{m}$ . The other structure parameters are the same as the above straight rib waveguide. The fundamental TE mode of the ridge waveguide of width  $w = 2 \mu\text{m}$  at  $1.55 \mu\text{m}$  wavelength is used as the excited field at  $z = 0$ . The computational window used of  $16 \times 20 \mu\text{m}$  is discretized with a grid size of  $\Delta x = \Delta y = 0.05 \mu\text{m}$ , and the path length of  $6 \mu\text{m}$  is discretized with a propagation step size  $\Delta z = 0.02 \mu\text{m}$ . DMI required a huge memory usage, and is therefore unpractical. Since in such a Y-branch waveguide the refractive index changes as a function of  $z$  and frequent matrix inversions are required during the propagation direction, GMRES and Bi-CGSTAB performed the propagation in 1220.9 and 1185.2 seconds, respectively. The runtime of CJI is only 781.9 seconds due to the high effective loss in the propagation medium.

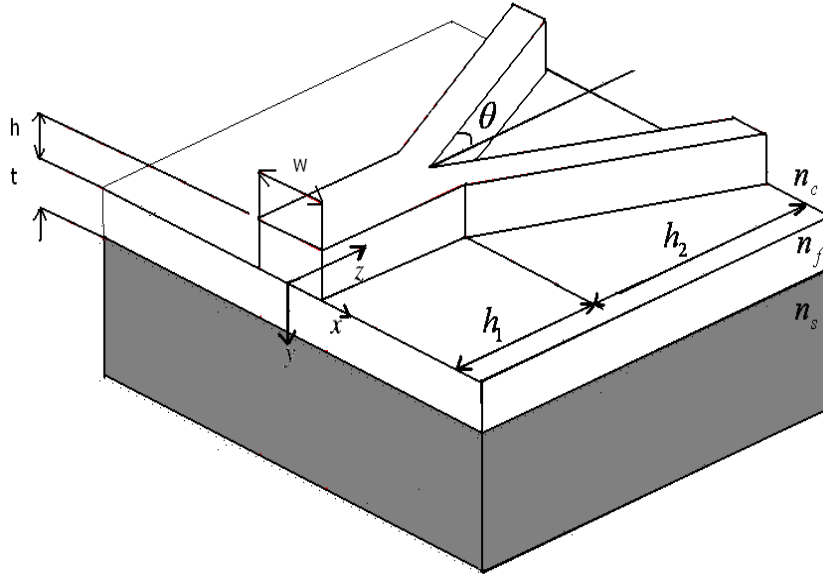


Figure 5.3. Y-branch optical rib waveguide

Table 5.1 summarises the performance of these methods for the optical waveguide structures chosen here. It is clearly seen that the runtime of the CJI method is substantially lower than that of the DMI, GMRES and Bi-CGSTAB method, except for 3D straight waveguides. For large problems requiring very large storage space and also for structures with a long path length with small propagation step size that require frequent matrix inversions, the DMI, GMRES and Bi-CGSTAB techniques are numerically very intensive. In contrast, for typical choices of  $k\Delta z$  the CJI technique offers rapid convergence and shorter runtimes in those cases.

Table 5.1

Quantitative comparison of runtimes of the iterative matrix solvers and the complex Jacobi iteration for WA beam propagation in waveguide (WG) structures

Structure \ Method	2D		3D	
	Tilted WG	Y-junction WG	Straight rib WG	Y-branch rib WG
DMI	241.5 s	4882 s	123 s	Out of memory
GMRES	41.8 s	982.8 s	0.6 s	1220.9 s
Bi-CGSTAB	37.6 s	1280.1 s	0.4 s	1185.2 s
CJI	34.5 s	243.5 s	2.7 s	781.9 s

## V.2. Efficient CJI-WA-BPMs for beam propagation in nonlinear waveguides

In chapter III, we discussed time-domain nonlinear BPMs based on modified Padé approximant operators. In this section, we are looking at frequency domain nonlinear BPMs and we present an extension of WA-BPMs using CJI (CJI-WA-BPMs) for nonlinear waveguide problems. An external excitation of a nonlinear waveguide was demonstrated to produce spatial multisoliton emission from the waveguide, in which a sequence of bright solitons could be emitted for sufficient input power [11]. For waveguides with a cladding consisting of nonlinear material where the refractive index depends on field intensity, it is difficult to obtain analytical solutions and thus, computational efforts are necessary for the design and modeling of these kinds of nonlinear optical waveguide devices. There are several methods developed to simulate the optical propagation in nonlinear waveguides in which the beam propagation method (BPM) has become one of the most powerful and efficient techniques.

A great number of BPM versions including the finite element-based and the finite difference-based BPM have been developed for these kinds of nonlinear problems [12-13]. We can modify our previously described CJI-WA-BPM method to deal with nonlinear Kerr effects by simply introducing an extra calculation step as in [7] where the CJI method has been successfully employed to simulate photonic components consisting of materials with nonlinear Kerr effects. The intensity dependent refractive index is given by

$$n^2 = n_l^2 + \gamma_l |\Psi|^2, \quad l = c, s, f, \quad (5.4)$$

with the subscripts c,s,f referring to the cladding, substrate and film, respectively. In the CJI-WA-BPM, this refractive index is easy to update at each propagation step.

The investigated nonlinear optical waveguide with a linear core bounded by linear and nonlinear claddings is shown in Fig. 5.4, where the refractive index  $n_s = n_c = 1.55$ ,  $n_l = 1.57$ ,  $\gamma_s = 0.01$ ,  $\gamma_c = \gamma_l = 0$ ,  $W = 5 \mu\text{m}$ ,  $Y = 50 \mu\text{m}$ ,  $d = 1 \mu\text{m}$  and the optical wavelength  $\lambda = 1.3 \mu\text{m}$ . The grid resolution is used of  $\Delta x = \Delta z = 0.05 \mu\text{m}$ . The fundamental TE mode as excitation is launched into the waveguide. The beam propagation in the linear optical waveguide is shown in Fig. 5.5 (a), while the evolution of the input beam in the nonlinear optical waveguide is depicted

in Fig. 5.5 (b). From the figure, it can be seen that a soliton is emitted through the film cladding interface into the nonlinear cladding and propagates away from it.

The calculated results are certainly in very good agreement with those obtained by the other authors [11-12] because the same equation is solved. However, the focus is on a performance of the CJI method in comparison with the DMI, GMRES and Bi-CGSTAB method. For a small propagation step size  $\Delta z = 0.05 \mu\text{m}$ , it is found that the amount of effective absorption is very high. This is a condition that favors rapid convergence of the CJI method. With a very strict propagation error tolerance of  $10^{-7}$ , the CJI method for the solution of the conventional Padé(1,1) approximant-based propagation equation required about 0.23 seconds to obtain a solution between two successive propagation steps, and 0.11 seconds for those based on the modified operator. This is attributed to the higher effective absorption as we stated earlier in Fig. 5.2. Since there is frequent matrix inversion required in this case too, the DMI method performed the propagation based on the conventional and the modified Padé(1,1) operator in 2.36 seconds and 2.34 seconds, respectively. The resulting runtimes of GMRES and Bi-CGSTAB for the propagation based on the conventional and the modified Padé(1,1) operator are (0.52, 0.45) seconds and (0.76, 0.53) seconds.

Table 5.2 summarises the performance of these methods for the nonlinear optical propagation here. It is seen that the CJI method performed much quicker propagation than these methods. Definitely, for large structures with a long path length required for a very small propagation step size that results in frequent matrix inversions, the DMI, GMRES and Bi-CGSTAB techniques are numerically very intensive. In contrast, for typical choices of  $k\Delta z$  the CJI technique offers rapid convergence and shorter runtimes.

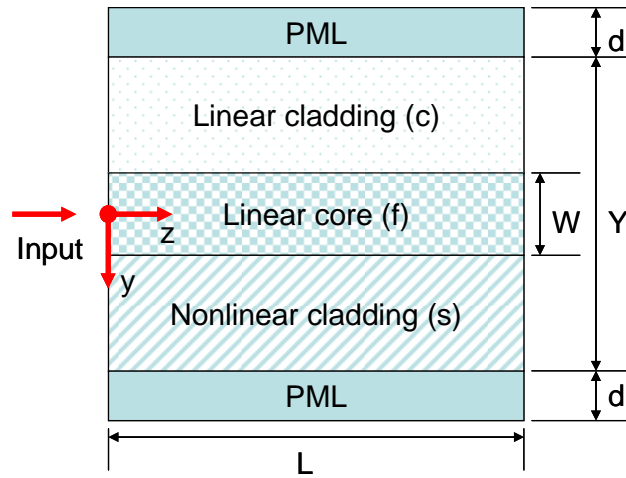


Figure 5.4. Nonlinear optical waveguide with a linear core bounded by linear and nonlinear claddings.

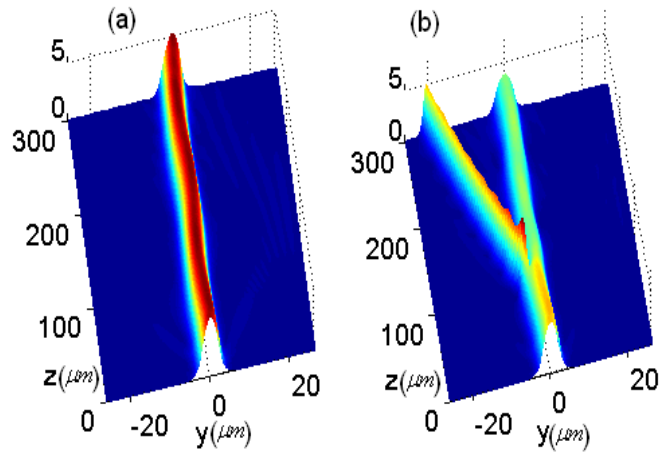


Figure 5.5. (a) TE mode propagating in linear waveguide and (b) soliton emission in nonlinear waveguide.

Table 5.2

Quantitative comparison of runtimes of the iterative matrix solvers and the CJI method for a beam propagation between two successive propagation steps based on the conventional and modified Padé(1,1) operator in the nonlinear waveguide

Operator	Conventional	Modified
DMI	2.36 s	2.34 s
GMRES	0.52 s	0.45 s
Bi-CGSTAB	0.76 s	0.53 s
CJI	0.23 s	0.11 s

### V.3. High order Padé approximant-based 3D WA-BPMs using CJI

For 3D waveguide problems that vary slowly in the propagation direction, an alternating-direction implicit (ADI) finite difference (FD) BPM is widely used. The ADI scheme is done by the splitting of the differential propagator into two directional components. However, this method is only first-order-accurate in the propagation step size and higher order methods are thus required for acceptable accuracy if wide-angle (WA) (i.e. non-paraxial) propagation is needed. Efforts have been made to relax the limitations for 3D WA simulations. A 3D multistep horizontal WA-BPM based on the generalized Douglas scheme, together with an ADI scheme was developed [15]. However, the WA propagator is only a Padé(1,1) approximant operator.

In this section, an improvement of CJI-WA-BPMs based on high order modified Padé(3,3) operator for 3D waveguide problems is achieved by using CJI to solve the propagation equation in partial steps [16]. The resulting method offers more accurate results than the one based on the simple Padé(1,1) approximant operator.

By employing the multistep algorithm for the propagation equation based on the modified Padé operator, we arrive at

$$\Phi^{m+\frac{i}{w}} = \frac{(1 + a_i P)}{(1 + a_i^* P)} \Phi^{m+\frac{i-1}{w}}. \quad (5.5)$$

This equation is of the same form as Eq. (2.28), but this time is based on modified operators. For an example, with the order of Padé operator  $N = 2$ , the coefficients  $a_i$  and  $a_i^*$  are given by

$$\begin{aligned}
 a_1 + a_2 &= \left(2 + \frac{1}{1 + \frac{i\beta}{2}}\right) \frac{1}{4k^2} - \frac{i\Delta z}{4k}, \\
 a_1 a_2 &= \frac{1}{16k^4 \left(1 + \frac{i\beta}{2}\right)} - \frac{i\Delta z}{16k^3} \left(1 + \frac{1}{1 + \frac{i\beta}{2}}\right), \\
 a_1^* + a_2^* &= \left(2 + \frac{1}{1 + \frac{i\beta}{2}}\right) \frac{1}{4k^2} + \frac{i\Delta z}{4k}, \\
 a_1^* a_2^* &= \frac{1}{16k^4 \left(1 + \frac{i\beta}{2}\right)} + \frac{i\Delta z}{16k^3} \left(1 + \frac{1}{1 + \frac{i\beta}{2}}\right).
 \end{aligned} \tag{5.6}$$

It is obvious that the modified Padé approximant reduces to the conventional Padé approximant as  $\beta = 0$ . From Eq. (5.5), it is clearly seen that each partial step is a simple Padé(1,1) approximant-based 3D WA beam propagation equation. For beam propagation of waveguide profiles with a 2D cross section, each 3D propagation equation can be recast in terms of a 2D Helmholtz equation with a source term and the effective absorption coefficients appearing in these equations are relatively high. That can lead to rapid convergence of the CJI method [16].

In order to demonstrate the efficiency of CJI compared to other existing methods including GMRES and Bi-CGSTAB, benchmark tests are carried out on the 3D Y-branch waveguide. The parameters needed for calculations can be found in Section V.1.3. With a small propagation step size  $\Delta z = 0.02 \mu\text{m}$  associated with frequent matrix inversion during the propagation direction, GMRES and Bi-CGSTAB took 4331.3 and 3976.6 seconds, respectively, whereas CJI took only 843.2 seconds due to very high effective medium loss caused by such a small propagation step size. Table 5.3 summarises the performance of these methods for the 3D Y-branch waveguide problem with 3-step and normal single-step algorithms. Interestingly, while the iterative matrix solvers performed propagation in the 3-step algorithm with runtimes of around 3 times of the normal single step, the CJI achieved almost similar runtimes for both cases. This is because of the much faster convergence of each of the substeps, which compensates for the fact that three steps need to be taken instead of one.

Table 5.3

Quantitative comparison of runtimes of the iterative matrix solvers and the CJI method for beam propagation in 3-step and normal single step algorithms

Algorithm	3-step	1-step
GMRES	4331.3 s	1220.9 s
Bi-CGSTAB	3976.6 s	1185.2 s
CJI	843.2 s	781.9 s

In summary, the CJI method has been adapted for the solution of wide-angle beam propagation with high order accuracy and it was shown to be highly competitive to other existing methods [16]. However, up to this point, the method has only been employed for scalar propagation problems where polarization effects and coupling between field components have been neglected. In the next section, polarization effects are taken into account to result in the semivectorial CJI-WA-BPMs.

#### **V.4. Stable semivectorial CJI-WA-BPM using the iterated Crank-Nicholson method**

In this section, an extension of 3D CJI-WA-BPM taking into account polarization effects is presented. It turns out that for 3D waveguides with constant refractive index profile the resulting iterative BPM still converges rapidly. However, for waveguides with varying index profile a straightforward implementation suffers from the fact that the iteration count between two successive cross-sections increases dramatically during the propagation direction. To overcome this problem, we proposed to use the iterated Crank-Nicholson method [17]. At each propagation step, the propagation equation is divided in multiple stages by the iterated Crank-Nicholson method and then each stage is recast in terms of a Helmholtz equation with source term, which is solved effectively by CJI.

### V.4.1. Formulation

As shown in Section II.2.2, the semivectorial Helmholtz equation for the quasi-TE and -TM mode are given by

$$\frac{\partial^2 \Psi_x}{\partial x^2} + \frac{\partial}{\partial x} \left( \frac{1}{n^2} \frac{\partial n^2}{\partial x} \Psi_x \right) + \frac{\partial^2 \Psi_x}{\partial y^2} + \frac{\partial^2 \Psi_x}{\partial z^2} + k_0^2 n^2(x, y, z) \Psi_x = 0 \quad (5.7a)$$

$$\frac{\partial^2 \Psi_y}{\partial x^2} + \frac{\partial}{\partial y} \left( \frac{1}{n^2} \frac{\partial n^2}{\partial y} \Psi_y \right) + \frac{\partial^2 \Psi_y}{\partial y^2} + \frac{\partial^2 \Psi_y}{\partial z^2} + k_0^2 n^2(x, y, z) \Psi_y = 0 \quad (5.7b)$$

where  $n$  is the refractive index profile and  $k_0$  is the vacuum wavevector. At any interface perpendicular to the x-direction, the refractive index and the electric field component are discontinuous. If we would ignore polarization by ignoring the second term in Eq. (5.7), the numerical evaluation of the derivatives would lead to large errors, especially in high-index-contrast waveguides.

Here, the numerical treatment of the quasi-TE mode is given. That for the quasi-TM mode is similar. Using the SVEA, in which the wave function  $\Psi_x(x, y, z)$  propagating in the z direction can be separated into a slowly varying envelope function  $\Phi(x, y, z)$  (for simplification purposes the subscript x is dropped) and a very fast oscillating phase term  $\exp(ikz)$ , the Helmholtz equation is given by:

$$\frac{\partial \Phi}{\partial z} - \frac{i}{2k} \frac{\partial^2 \Phi}{\partial z^2} = \frac{iP}{2k} \Phi, \quad (5.8)$$

where  $P = \nabla_{\perp}^2 + k_0^2(n^2 - n_{ref}^2) = \frac{\partial^2}{\partial x^2} + \frac{\partial}{\partial x} \left( \frac{1}{n^2} \frac{\partial n^2}{\partial x} \right) + \frac{\partial^2}{\partial y^2} + k_0^2(n^2 - n_{ref}^2)$  with  $k = k_0 n_{ref}$ . The finite difference

discretization of the term  $\frac{\partial}{\partial x} \left( \frac{1}{n^2} \frac{\partial n^2}{\partial x} \Phi \right)$  is given as follows:

$$\frac{\partial}{\partial x} \left( \frac{1}{n^2} \frac{\partial n^2}{\partial x} \Phi \right) = \frac{1}{\Delta x^2} \left[ \frac{n^2(i+1, j) - n^2(i, j)}{n^2(i+1, j) + n^2(i, j)} (\Phi_{i+1, j} + \Phi_{i, j}) - \frac{n^2(i, j) - n^2(i-1, j)}{n^2(i, j) + n^2(i-1, j)} (\Phi_{i, j} + \Phi_{i-1, j}) \right]. \quad (5.9)$$

From Eq. (5.8), different treatments of WA-BPM can be developed. In this work, the modified Padé(1,1) approximant operator for a wide-angle propagator is used and leads to a beam propagation equation as follows:

$$(1 + \xi P)\Phi^{n+1} = (1 + \xi^* P)\Phi^n, \quad (5.10)$$

where  $\xi = \frac{1}{4k^2(1+i)} - \frac{i\Delta z}{4k}$ ,  $\xi^* = \frac{1}{4k^2(1+i)} + \frac{i\Delta z}{4k}$  and  $\Delta z$  the propagation step size.

The adaptation of the CJI method for the solution of Eq. (5.10) is given as follows:

By dividing both sides of this equation by  $\xi$ , it may be written as an inhomogeneous Helmholtz equation

$$[\nabla_{\perp}^2 + k_0^2(n^2 - n_m^2) + \frac{1}{\xi}]\Phi^{n+1} = (\frac{\xi^*}{\xi}P + \frac{1}{\xi})\Phi^n, \quad (5.11)$$

or

$$[\nabla_{\perp}^2 + k_0^2(n^2 - n_{ref}^2) + \frac{1}{\xi}]\Phi^{n+1} = source\ term, \quad (5.12)$$

It is clearly seen that the beam propagation equation is recast as a Helmholtz equation with source term in an effective medium with loss determined by the imaginary part of  $1/\xi$ . Thus, it is easy to solve this equation effectively by the CJI method. Its convergence rate is mostly dominated by the amount of effective absorption (or medium loss). If the loss is high, rapid convergence is obtained.

However, for waveguides with refractive index profiles varying through the propagation direction the iteration count between two successive cross-sections increases dramatically. This problem can be remedied, however, by considering multistage solving of Eq. (5.10) by the iterated Crank-Nicholson (ICN) method. In Ref. [18] the author proved that for dealing with the so-called advective equation when using the ICN method, one should use two stages. In this work, it is numerically shown in the next section that the complex Jacobi iterative solution of Eq. (5.10) using the ICN method is stable and results in significant advantages in terms of execution speed for semivectorial beam propagation over a very long path length. The implementation of the ICN method is described as follows:

Rather than solving Eq. (5.10) directly by the CJI method, it is divided in multiple stages.

First, we calculate the initial estimated field  $^{(1)}\Phi^{n+1}$  at the next propagation cross-section  $(n+1)$  using Eq. (5.10):

$$(1 + \xi P)^{(1)}\Phi^{n+1} = (1 + \xi^* P)\Phi^n, \quad (5.13)$$

Eq. (5.13) is solved by the iterative procedure described above. Then the field at the mid-step cross-section ( $n+1/2$ ) is made by weighting equally the newly predicted solution  ${}^{(1)}\Phi^{n+1}$  and the previous solution  $\Phi^n$ . This can be seen as the special case of a more generic averaging of the type

$${}^{(1)}\Phi^{n+1/2} = \theta {}^{(1)}\Phi^{n+1} + (1-\theta)\Phi^n, \quad (5.14)$$

where  $\theta$  is the ICN weight coefficient, here set to 0.1. Similarly, the final estimated field  $\Phi^{n+1}$  at the next propagation cross-section ( $n+1$ ) is recalculated by

$$(1+\xi P)\Phi^{n+1} = (1+\xi^* P) {}^{(1)}\Phi^{n+1/2}. \quad (5.15)$$

This happens again in an iterative way.

## V.4.2. Convergence study of semivectorial CJI-WA-BPM

That polarization effects in high-index-contrast waveguides play an important role in the accuracy of BPM was already shown in [19]. In this section, an investigation of how polarization effects affect the convergence rate of the CJI method is carried out. The Gaussian beam propagation in a 3D rib waveguide is considered [9]. The iteration count of the CJI method with respect to propagation steps through the propagation direction is shown in Fig. 5.6. From the figure, it is shown that due to polarization effects through discontinuous interfaces in the waveguide, the CJI method requires slightly more iterations than the method where these effects are ignored.

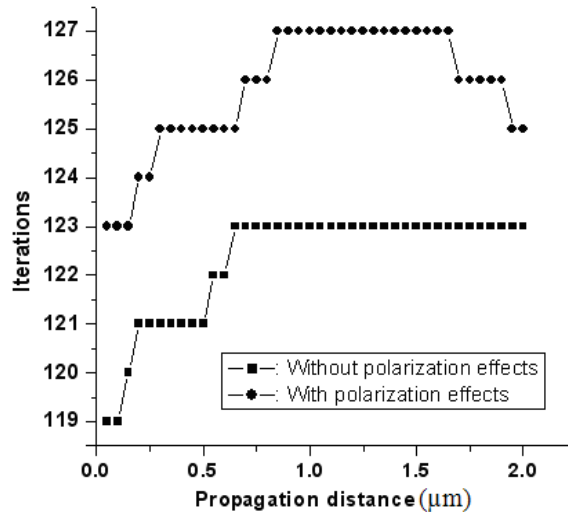


Figure 5.6. The iteration count per propagation step for a Gaussian beam propagation through a 3D rib waveguide with and without polarization effects.

In addition, as mentioned in previous sections, besides the polarization effects, varying refractive index profiles through the propagation direction also leads to an increase of iteration count between two successive cross-sections as shown in Fig. 5.7. In that figure, the iteration count between two successive cross-sections in a Y-junction waveguide of the semivectorial CJI-WA-BPM with and without ICN is shown. The initial rib waveguide is split into two 5-degree tilted waveguides as shown in Fig. 5.3, where the longitudinal dimension is  $h_1 = 1 \mu\text{m}$ , and the width and height of the straight rib waveguide are  $w = 2 \mu\text{m}$  and  $h = 1.1 \mu\text{m}$ . The guiding core has an index  $n_f = 3.44$  and a thickness  $t = 0.2 \mu\text{m}$  while the refractive index of substrate and cover is  $n_s = 1.44$  and  $n_c = 1$ , respectively. The fundamental TE mode of the ridge waveguide of width  $w = 2 \mu\text{m}$  at  $1.3 \mu\text{m}$  wavelength is used as the excited field at  $z = 0$ . The iterations were terminated when a field-weighted residual of  $10^{-7}$  was satisfied at each grid point.

For a grid size  $\Delta x = \Delta y = \Delta z = 0.05 \mu\text{m}$ , the iteration count between two successive cross-sections required for the CJI method without using ICN increases dramatically as can be seen in Figure 5.7. The same figure also shows that the iteration count of the ICN-CJI method is stable. Even though there are 2 ICN-CJI iterations needed per equivalent non-ICN-CJI iteration, this fact becomes quickly offset for larger propagation distances.

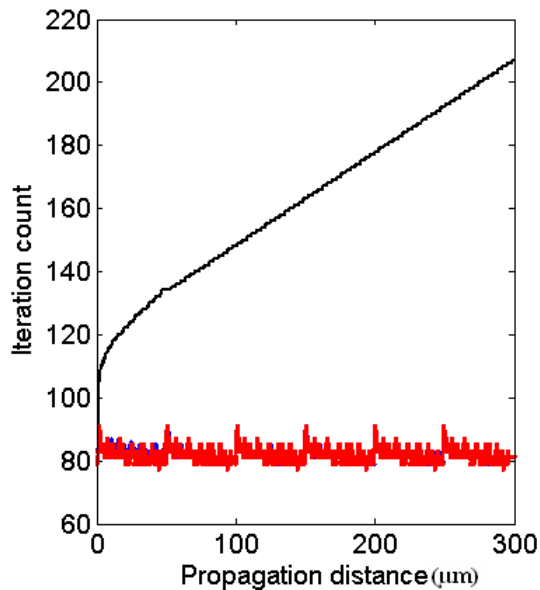
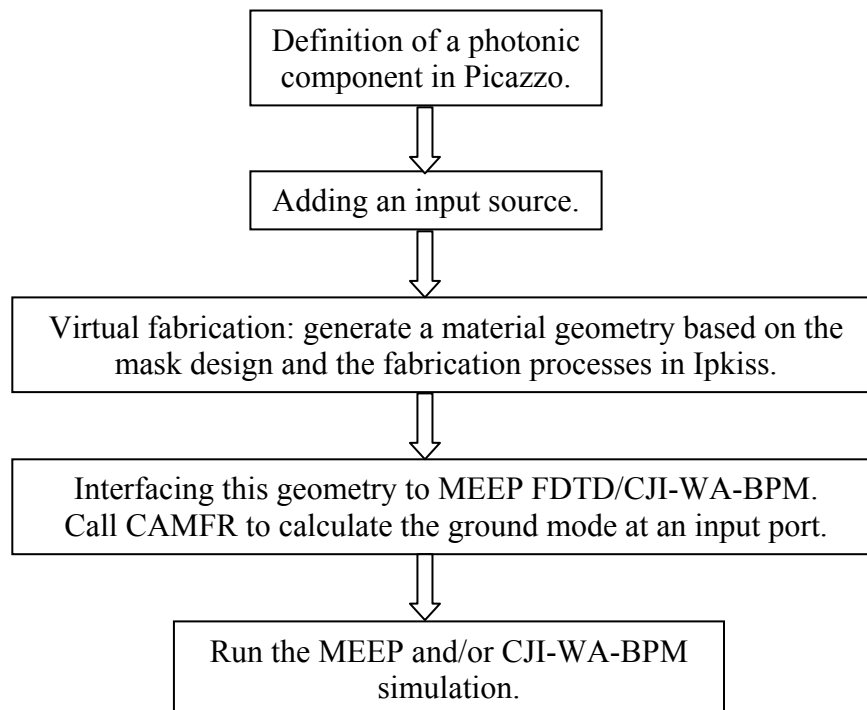


Figure 5.7. Iterations count per propagation step of the CJI method for beam propagation in a symmetric Y-branch waveguide with (blue and red lines for the iteration count of Eq. 5.13 and 5.15 respectively) and without (black line) using the ICN method.

## V.5. CJI-WA-BPMs: integrated in LightPy framework

In this section, the integration of the developed CJI-WA-BPM into the LightPy framework is presented. LightPy is a central framework for silicon photonic devices developed by the Photonics Research Group at Ghent University where Ipkiss/Picazzo and Pysimul software are integrated. Ipkiss is a flexible and powerful parametric design engine. It allows to generate any type of lithography mask and has a modular architecture which can load plug-ins: for design of photonic components, for simulation of the physical fabrication, and for integration with the simulation tool Pysimul. Picazzo is a library of photonic components which includes splitters, ring resonators, fiber couplers, AWGs and other components typically used in photonics. Pysimul is a simulation framework which tightly integrates Ipkiss and Picazzo with different simulation engines such as MEEP FDTD [20], CAMFR [21] and CJI-WA-BPMs. It aims to be an interface to connect virtually fabricated components with simulation engines. The flowchart of the simulation performed in LightPy can be sketched as follows [22]:



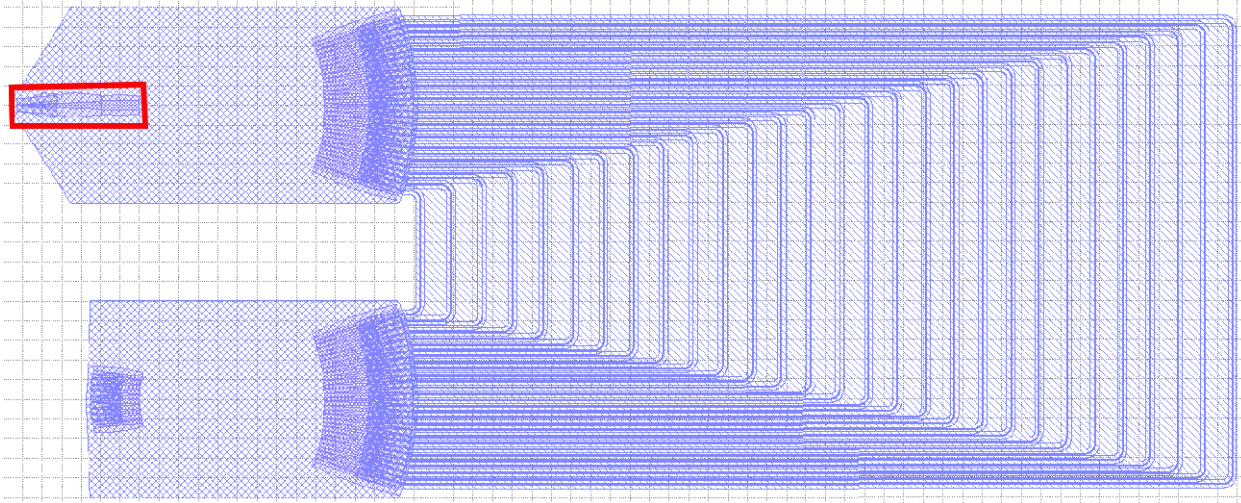


Figure 5.8. A simulated AWG in silicon-on-insulator platform.

As an example to show how LightPy simulates a photonic component, we look at a simulation of an AWG as depicted in Fig. 5.8. It is one of the vital components in wavelength division multiplexing (WDM) systems. An AWG is used to separate many wavelength channels into different waveguides. It consists of two star couplers and an array of waveguides with a linear increment of length. When a light beam is launched into the input start coupler, it is distributed over the waveguide array. Then the output start coupler separates different wavelengths with different phase shifts.

First, the definition of this component is done in Picasso. After adding an input source, e.g. a continuous source at  $1.55 \mu\text{m}$  wavelength, the virtual fabrication of this component is done to generate a material geometry. Then this geometry is interfaced to simulation engines including MEEP and/or CJI-WA-BPMs. Since it is very a big component to simulate completely with a single simulation technique, our group (a.o. PhD student Shibnath Pathak) has developed a hybrid semi-analytical model to simulate several subparts of it separately. Each subpart is simulated with a different simulation strategy. There, the transmission matrices (T-matrices) for the different subparts are calculated and then multiply these T-matrices to obtain the T-matrix of the entire AWG [23].

For example: the MMI aperture indicated in the red rectangular in Fig. 5.8 is simulated by CJI-WA-BPM or EME in CAMFR, and the propagation in the waveguide array is done analytically. A zoomed-in version of such a MMI aperture is depicted in Fig. 5.9.

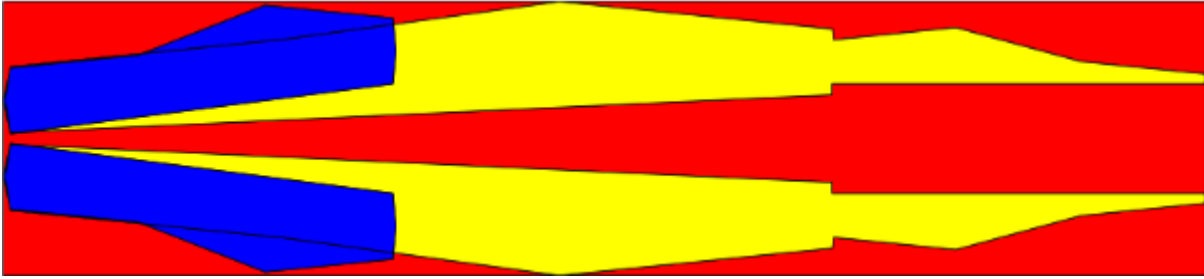


Figure 5.9. A simulated MMI aperture.

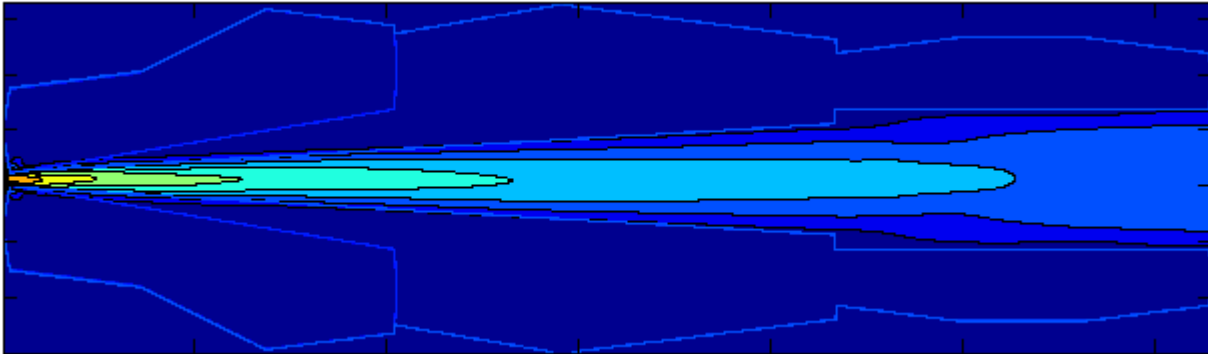


Figure 5.10. Field distribution in the simulated MMI aperture.

It is obvious that the simulation of this structure is easily done by CJI-WA-BPM or CAMFR. For 2D cases, the advantage of using CJI-WA-BPM is not much compared to CAMFR. However, the main benefit resides in simulating 3D structures, where FDTD simulations would be way too expensive to include in optimization loops. As an example, Fig. 5.10 shows the field distribution in this aperture calculated by CJI-WA-BPM. Then this part is combined with a T-matrix model of the arrayed waveguides and a simulation of the output start coupler to render a complete simulation of the AWG. Based on these tools, Shibnath Pathak will perform a detailed design study of the performance of these AWG devices.

## V.6. Conclusion

In this chapter, a new CJI method adapted for the solution of 3D wide-angle beam propagation has been presented. Through a quantitative comparison of runtimes between the traditional DMI, GMRES, Bi-CGSTAB and the new CJI method for both 2D and 3D wide-angle beam propagation it was demonstrated convincingly that the CJI method is very competitive for demanding problems. This solution technique has also enabled the development of 3D WA-BPMs based on higher orders of Padé approximant operators that offers an improvement in terms

of accuracy. The improved version of CJI-WA-BPMs has also performed faster propagation analysis than the above matrix solvers.

In addition, the resulting CJI-WA-BPM extended to model non-paraxial beam propagation in nonlinear optical waveguides has been presented. For a typical choice of propagation step size, the iterative method offers rapid convergence and is very competitive for demanding problems in comparison with the existing matrix solvers for nonlinear BPM.

Apart from CJI-WA-BPMs for scalar propagation where polarization effects are ignored, the method has been extended to take such polarization effects into account. This results in the semivectorial CJI-WA-BPM. However, the semivectorial iterative method is itself unstable for propagation in high-index-contrast waveguides with refractive index profiles varying during the propagation direction. In order to overcome this problem, the use of the iterated Crank-Nicholson method has been proposed. The resulting semivectorial method was stable and very well-suited for large structures with long path length.

Finally, the integration of CJI-WA-BPMs into LightPy framework has been presented. It certainly benefits the user who wants to design and model photonic devices.

# References

1. C. Ma and E. V. Keuren, "A simple three dimensional wide-angle beam propagation method," *Opt. Express* **14**, 4668-4674 (2006).
2. E. L. Bekker, P. Sewell, T. M. Benson, and A. Vukovic, "Wide-angle alternating-direction implicit finite-difference beam propagation method," *J. Lightwave Technol.* **27**, 2595-2604 (2009).
3. C. Ma and E. V. Keuren, "A three-dimensional wide-angle beam propagation method for optical waveguide structures," *Opt. Express* **15**, 402-407 (2007).
4. Khai Q. Le, R. G. Rubio, P. Bienstman, and G. R. Hadley, "The complex Jacobi iterative method for three-dimensional wide-angle beam propagation," *Opt. Express* **16**, 17021-17030 (2008).
5. Z. Ju, J. Fu and E. Feng, "A simple wide-angle beam-propagation method for integrated optics," *Microwave Opt. Technol. Lett.* **14**, 345-347 (1997).
6. J. P. Bérenger, "A perfectly matched layer for the absorption of electromagnetic waves," *J. Comput. Phys.* **114**, 185–200 (1994).
7. P. Vandersteengen, B. Maes, P. Bienstman and R. Baets, "Using the complex Jacobi method to simulate Kerr non-linear photonic components," *Opt. and Quantum Electron.* **38**, 35-44 (2006).
8. T. Anada, T. Hokazono, T. Hiraoka, J. P. Hsu, T. M. Benson, and P. Sewell, "Very-wide-angle beam propagation methods for integrated optical circuits," *IEICE Trans. Electron.* **E82-C**, 1154–1158 (1999).
9. P. C. Lee and E. Voges, "Three-dimensional semi-vectorial wide-angle beam propagation method," *J. Lightwave Technol.* **12**, 215–225 (1994)
10. Y. Tsuji, M. Koshiha, and T. Shiraishi, "Finite element beam propagation method for three-dimensional optical waveguide structures," *J. Lightwave Technol.* **15**, 1728-1734 (1997).
11. E. M. Wright, G. I. Stegeman, C. T. Seaton, J. V. Moloney, and A. D. Boardman, "Multisoliton emission from a nonlinear waveguide," *Phys. Rev. A* **34**, 4442-4444 (1986).
12. T. Yasui, M. Koshiha, and Y. Tsuji, "A wide-angle finite element beam propagation method with perfectly matched layers for nonlinear optical waveguides," *J. Lightwave Technol.* **17**, 1909-1915 (1999).

13. J. de-Oliva-Rubio, and I. Molina-Fernandez, "Fast semivectorial nonlinear finite-difference beam propagation method," *Microwave Opt. Technol. Lett.* **40**, 73-77 (2004).
14. Khai Q. Le and P. Bienstman, "The complex Jacobi iterative method for non-paraxial beam propagation in nonlinear optical waveguides," *Opt. and Quantum Electron.* **41**, 705-709 (2010).
15. J. Shibayama, T. Takahashi, J. Yamauchi, and H. Nakano, "A three-dimensional multistep horizontally wide-angle beam-propagation method based on the generalized Douglas scheme," *IEEE Photonics Tech. Lett.* **18**, 2535-2537 (2006).
16. Khai Q. Le and P. Bienstman, "Three-dimensional higher-order Padé approximant-based wide-angle beam propagation method using complex Jacobi iteration," *Electron. Lett.* **46**, 231-232 (2010).
17. Khai Q. Le and P. Bienstman, "A stable complex Jacobi iterative solution of 3D semivectorial wide-angle beam propagation using the iterated Crank-Nicholson method," *Opt. Quantum Electron.* **41**, 215-221 (2009).
18. S. A. Teukolsky, "Stability of the iterated Crank-Nicholson method in numerical relativity," *Phys. Rev. D* **61**, 087501-01-087501-02 (2000).
19. D. Bhattacharya and A. Sharma, "Finite difference split step method for non-paraxial semivectorial beam propagation in 3D," *Opt. and Quant. Electron.* **40**, 933-942 (2009).
20. MEEP FDTD, <http://ab-initio.mit.edu/wiki/index.php/Meep>.
21. CAMFR, <http://camfr.sourceforge.net/>.
22. M. Fiers, E. Lambert, S. Pathak, B. Maes, P. Bienstman and W. Bogaerts, "Improving the design cycle for nanophotonic components," to appear in *J. Comput. Sci.* (2011).
23. S. Pathak, W. Bogaerts, E. Lambert, P. Dumon and D. Van Thourhout, "Integrated design and simulation tools for silicon photonic arrayed waveguide gratings," 15<sup>th</sup> Annual Symposium of the IEEE Photonics Benelux Chapter, Netherlands, 41-44 (2010).

# Chapter VI

## New approximate solution for wave propagation in graded-index metamaterials

Electromagnetic (EM) metamaterials, a new class of artificial composite materials, have recently attracted intensive interest due to their potential for new applications such as negative refraction, inverse Doppler effect, and radiation tension instead of pressure [1,2], as well as electromagnetic cloaking of arbitrary shaped objects [3]. In addition, there has been a growing research interest in the propagation behavior of EM waves in metamaterials with material properties changing in the propagation direction. The WA-BPM as discussed so far is a very powerful tool for the design and simulation of guided-wave structures. However, it is not suited for addressing wave propagation in such graded-index metamaterials with indices increasing in the propagation direction since the approximations in traditional BPM ignore graded-index changes of the propagation medium.

There exist various analytical and numerical approaches to investigate wave propagation in optical structures incorporating metamaterials with graded-index profiles such as the invariant embedding method [4] and the finite difference time domain (FDTD) method [5,6]. While the analytical methods are currently limited to low-dimensionality problems, the FDTD method is well-known as a time-consuming method, especially for three dimensional structures. Efforts to find more efficient methods for large computational problems are thus imperative. This chapter is devoted to presenting such a new approximate solution for wave propagation whereby the exact wave propagation operator is approximated by any one of a sequence of higher-order  $(m,n)$  Padé approximant operators. The resulting formalism offers a substantial advantage as an accurate and efficient solution of high-dimensionality wave propagation problems. We published the results of this chapter in [7].

## VI.1. Formulation

For isotropic metamaterials we assume that their optical properties can be described by the effective dielectric permittivity and the effective magnetic permeability. Furthermore, with EM fields that are periodic in time according to a  $\exp(-i\omega t)$  dependency we can obtain the scalar wave equations for the electric field ( $E_y$ ) and the magnetic field ( $H_x$ ) components from Maxwell's equations as follows [8]:

$$\frac{\partial^2 E_y}{\partial z^2} + \frac{\partial^2 E_y}{\partial x^2} + \frac{\partial^2 E_y}{\partial y^2} - \frac{1}{\mu} \frac{\partial \mu}{\partial z} \frac{\partial E_y}{\partial z} + \omega^2 \mu \varepsilon E_y = 0 \quad (6.1)$$

or

$$\frac{\partial^2 H_x}{\partial z^2} + \frac{\partial^2 H_x}{\partial x^2} + \frac{\partial^2 H_x}{\partial y^2} - \frac{1}{\varepsilon} \frac{\partial \varepsilon}{\partial z} \frac{\partial H_x}{\partial z} + \omega^2 \mu \varepsilon H_x = 0 \quad (6.2)$$

where  $\varepsilon = \varepsilon(\omega, z)$  and  $\mu = \mu(\omega, z)$  are the frequency-dependent electric permittivity and magnetic permeability, respectively. These equations describe the propagation of EM waves through a medium of which the constitutive parameters vary along the propagation axis  $z$ . Here, we restrict ourselves to the case where the first derivative of both the permittivity and the permeability is non-zero.

Subsequently, a numerical solution of these equations is presented here and it is employed to investigate the propagation of EM waves through a graded-index metamaterial structure. The transition between negative and positive index media was ignored in this work. For simplification purposes, we only consider Eq. (6.1) as those for Eq. (6.2) are equivalent. Eq. (6.1) can be rewritten as:

$$Q \frac{\partial E_y}{\partial z} - \frac{\partial^2 E_y}{\partial z^2} = P E_y \quad (6.3)$$

where  $P = \nabla_{\perp}^2 + \omega^2 \mu \varepsilon = \frac{\partial^2}{\partial x^2} + \frac{\partial^2}{\partial y^2} + \omega^2 \mu \varepsilon$  and  $Q = \frac{1}{\mu} \frac{\partial \mu}{\partial z}$ .

Eq. (6.3) can formally be rewritten in the form

$$\frac{\partial E_y}{\partial z} = \frac{P}{Q - \frac{\partial}{\partial z}} E_y \quad (6.4)$$

Equation (6.4) suggests the following recurrence relation

$$\left. \frac{\partial}{\partial z} \right|_{n+1} = \frac{P}{Q - \left. \frac{\partial}{\partial z} \right|_n} \tag{6.5}$$

As we have seen before, a recurrence relation of this form can give rise to either real or modified Padé approximant operators depending on the initial value [9-11]. If Eq. (6.5) is used to replace the first derivative of fields with respect to  $z$  with an expression containing only the operator  $P$ , then a propagator of the following form is obtained:

$$\frac{\partial E_y}{\partial z} \approx \frac{N}{D} E_y \tag{6.6}$$

where  $N$  and  $D$  are polynomials in  $P$ .

### VI.1.1. Real Padé approximant operators

In case the initial value of  $\left. \frac{\partial}{\partial z} \right|_0 = 0$  is used, this gives us a real Padé( $m,n$ ) approximant-based wave propagation formula as follows:

$$\frac{\partial E_y}{\partial z} \approx Q \frac{A(m)}{B(n)} E_y \tag{6.7}$$

where  $A(m)$  and  $B(n)$  are polynomials in  $X = P/Q^2$ . The most useful low-order Padé( $m,n$ ) approximant operators are shown in Table 6.1.

Table 6.1

Most useful low-order Padé approximants for wave propagator in terms of the operator  $X = P/Q^2$

Order	Expression	
	Padé	Modified Padé
(1,1)	$\frac{X}{1-X}$	$\frac{X}{1 - \frac{1}{1+i\beta/2} X}$
(2,2)	$\frac{X - 2X^2}{1 - 3X + X^2}$	$\frac{X - \left(1 + \frac{1}{1+i\beta/2}\right) X^2}{1 - \left(2 + \frac{1}{1+i\beta/2}\right) X + \frac{1}{1+i\beta/2} X^2}$
(3,3)	$\frac{X - 4X^2 + 3X^3}{1 - 5X + 6X^2 - X^3}$	$\frac{X - \left(3 + \frac{1}{1+i\beta/2}\right) X^2 + \left(1 + \frac{2}{1+i\beta/2}\right) X^3}{1 - \left(4 + \frac{1}{1+i\beta/2}\right) X + \left(3 + \frac{3}{1+i\beta/2}\right) X^2 - \frac{1}{1+i\beta/2} X^3}$

If Eq. (6.7) is compared with a formal solution of Eq. (6.1) written in the well-known form

$$\frac{\partial E_y}{\partial z} = Q \left( \frac{1}{2} - \sqrt{\frac{1}{4} - X} \right) E_y, \quad (6.8)$$

the following formula is obtained

$$\frac{1}{2} - \sqrt{\frac{1}{4} - X} \approx \frac{A(m)}{B(n)}. \quad (6.9)$$

As mentioned in previous chapters, the real Padé approximant operators incorrectly propagate evanescent modes. To circumvent this problem, we introduce modified Padé approximant operators.

### VI.1.2. Modified Padé approximant operators

By sharing the same idea with the real Padé approximant operators but using a different initial value modified Padé approximant operators are obtained. Here, we give the derivation of this initial value for the specific problem that is being considered here.

From Eq. (6.4) the relevant form is written as follows:

$$-\frac{2}{Q} \frac{\partial}{\partial z} = \frac{-\frac{4P}{Q^2}}{2 - \frac{2}{Q} \frac{\partial}{\partial z}}. \quad (6.10)$$

This equation may be rewritten as

$$f(Y) = \frac{Y}{2 + f(Y)} \quad (6.11)$$

where  $f(Y) = -\frac{2}{Q} \frac{\partial}{\partial z}$  and  $Y = -\frac{4P}{Q^2}$ .

Eq. (6.11) suggests the recurrence relation

$$f_{n+1}(Y) = \frac{Y}{2 + f_n(Y)} \quad \text{for } n=0,1,2,\dots \quad (6.12)$$

Y. Y. Lu [12] has proved that Eq. (6.12) can provide a good approximation to  $\sqrt{1+Y} - 1$  with the initial value of

$$f_0(Y) = i\beta \quad \text{where } \beta > 0 \text{ is a damping parameter.} \quad (6.13)$$

Subsequently, the modified Padé approximant operators are obtained from the same recurrence formula (6.5) with a different initial value of  $\left. \frac{\partial}{\partial z} \right|_0 = -i \frac{\beta}{2} Q$ . The most useful low-order

modified Padé approximant operators are also shown in Table 6.1. As before, the modified Padé operator could give waves propagating in evanescent regions the desired damping.

### VI.1.3. Numerical implementation of Padé-based wave propagation

One of the most commonly used techniques to numerically deal with Eq. (6.7) is the finite difference method. Finite difference equations may be derived from Eq. (6.7) by clearing the denominator and centering with respect to  $z$  in the usual way:

$$B(E_y^{n+1} - E_y^n) = \frac{Q^n \Delta z}{2} A(E_y^{n+1} + E_y^n). \quad (6.14)$$

Eq. (6.14) can be solved effectively by a multistep method whereby each component step is treated by the traditional direct matrix inversion (DMI) [13]. However, as we have already seen, for large problems, requiring huge memory to establish matrix inversion, DMI is very slow. For the last decade alternative methods have been proposed to solve matrix inversion effectively by iteration techniques such as Bi-CGSTAB [14]. However, for large three-dimensional problems where the material properties change frequently and which therefore require frequent matrix inversions, this can still be a numerically intensive task. Just as in previous chapters, we use the complex Jacobi iterative (CJI) method [15]. There, the wave propagation equation is recast in terms of a Helmholtz equation with a source term. The usefulness of the CJI technique depends mostly upon its execution speed dominated by the amount of effective absorption (or medium loss). If the medium loss is high, the convergence rate is fast.

## VI.2. Example

In order to prove the applicability of this approximate method, we employ it to study wave propagation in an inhomogeneous negative index metamaterial where the effective permittivity and permeability vary according to a hyperbolic tangent function. Of course, the method works equally well for positive-index graded materials.

An investigation is carried out on an electric wave propagating in a medium where  $\epsilon$  and  $\mu$  are both always non-zero and are given by the following functions (see Fig. 6.1):

$$\epsilon = -\epsilon_0 \epsilon_{\text{eff}}(\omega) (\tanh(\rho z) + 2), \quad \mu = -\mu_0 \mu_{\text{eff}}(\omega) (\tanh(\rho z) + 2). \quad (6.15)$$

where  $\rho$  ( $=10^{+6}$ ) is a positive parameter ensuring index profiles to be graded and the first derivative of  $\epsilon$  and  $\mu$  are therefore non-zero. We assume a wave with wavelength of  $\lambda_0 = 1 \mu\text{m}$  propagating in such medium of  $\epsilon_{\text{eff}}(\lambda_0) = \mu_{\text{eff}}(\lambda_0) = 1$ . Figure 6.2 shows the comparison of the calculated results obtained by the solution from the real Padé operator, the modified Padé

operator and the true wave equation (as solved directly by the finite element method in the commercial software-COMSOL multiphysics [16]). The input field is excited at  $-1.5 \mu\text{m}$ . It is seen that the result obtained from the modified Padé operator allows a better agreement to the true wave equation than that of the real one. The remaining discrepancies are probably due to the low order of the Padé approximant.

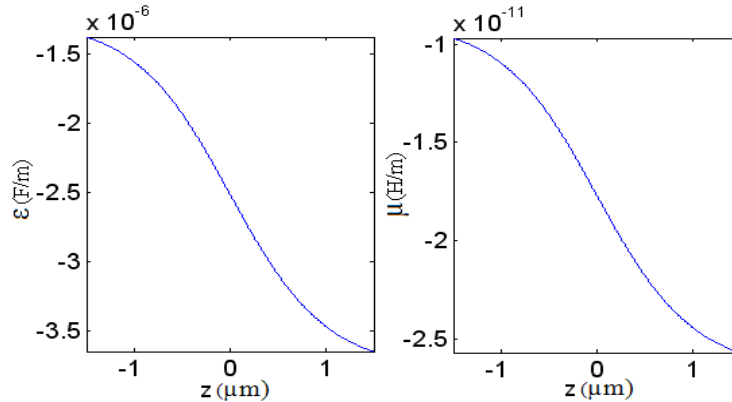


Figure 6.1. The permittivity and permeability vary along the propagation direction according to a hyperbolic tangent function assumed in this chapter.

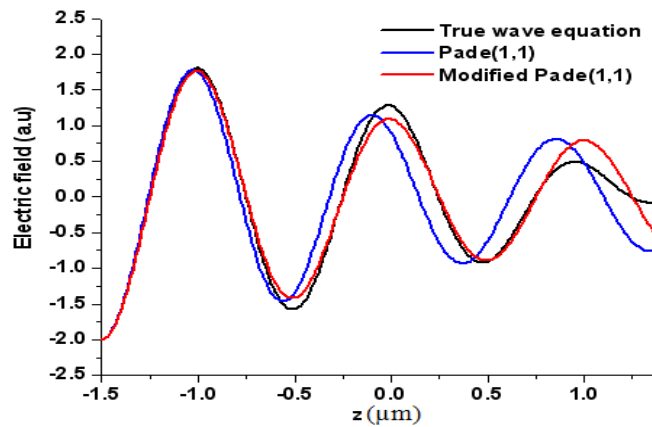


Figure 6.2. Propagation of electric wave in graded-index structure with index profile changing according to hyperbolic tangent function.

### VI.3. Conclusion

In this chapter, a new approximate solution for wave propagation in graded-index media based on Padé approximant operators has been derived. The resulting formulas allow accurate approximations to the true wave equation. It results in a promising tool to investigate wave propagation in media where the permittivity and the permeability change in the propagation direction.

# References

1. V. G. Veselago, "The electrodynamic of substances with simultaneously negative value of  $\epsilon$  and  $\mu$ ," *Sov. Phys. Usp* **10**, 509-514 (1968).
2. R. A. Shelby, D. R. Smith, and S. Schultz, "Experimental verification of a negative index of refraction," *Science* **292**, 77-79 (2001).
3. J. B. Pendry, D. Schurig, and D. R. Smith, "Controlling electromagnetic fields," *Science* **312**, 1780-1782 (2006).
4. K. Kim, D.-H. Lee, and H. Lim, "Resonant absorption and mode conversion in a transition layer between positive-index and negative-index media," *Opt. Express* **16**, 18505-18513 (2008).
5. R. W. Ziolkowski and E. Heyman, "Wave propagation in media having negative permittivity and permeability," *Phys. Rev. E* **64**, 056625 (2001).
6. R. W. Ziolkowski, "Pulsed and CW Gaussian beam interaction with double negative metamaterial slabs," *Opt. Express* **11**, 662-681 (2003).
7. Khai Q. Le and P. Bienstman, "Padé approximate solution for wave propagation in graded-index metamaterials," *J. Opt.* **13**, 024015 (2010).
8. M. Dalarsson and P. Tassin, "Analytical solution for wave propagation through a graded index interface between a right-handed and a left-handed material," *Opt. Express* **17**, 6747-6751 (2009).
9. G. R. Hadley, "Wide-angle beam propagation using Padé approximant operators," *Opt. Lett.* **17**, 1426-1428 (1992).
10. Khai Q. Le and P. Bienstman, "Wide-angle beam propagation method without using slowly varying envelope approximation," *J. Opt. Soc. Am. B*, **26**, 353-356, (2009).
11. Khai Q. Le, "Complex Padé approximant operators for wide-angle beam propagation," *Opt. Commun.* **282**, 1252-1254 (2009).
12. Y. Y. Lu, "A complex coefficient rational approximation of  $\sqrt{1+x}$ ," *App. Numer. Math.* **27**, 141 (1998).
13. G. R. Hadley, "Multistep method for wide-angle beam propagation," *Opt. Lett.* **17**, 1743-1745 (1992).

14. H. A. Van der Vorst, "Bi-CGSTAB: A fast and smoothly converging variant of Bi-CG for the solution of nonsymmetric linear systems," *SIAM J. Sci. Stat. Comput.* **13**, 631-644 (1992).
15. Khai Q. Le, R. G. Rubio, P. Bienstman, and G. R. Hadley, "The complex Jacobi iterative method for three-dimensional wide-angle beam propagation," *Opt. Express* **16**, 17021-17030 (2008).
16. COMSOL, <http://www.comsol.com>

# Chapter VII

## Enhanced sensitivity of a Silicon-On-Insulator surface plasmon interferometer with additional silicon layer

Surface plasmon resonance (SPR) sensors, which use surface plasmon polariton (SPP) waves to probe interactions between biomolecules and sensor surfaces, have attracted tremendous interest in the past decade for the optical detection of small biological or chemical entities in liquids [1]. The concept of the SPP wave is well-known as the perpendicularly confined electromagnetic wave, which propagates along an interface between a metal and a dielectric.

In general, conventional SPR sensors have been restricted to the Kretschmann configuration where a thin metal film is coated on one side of the prism which separates the sensing medium and the prism. Unfortunately, the conventional configuration is not suitable for the integration into optical circuits, because of the bulky structure of the metal-coated prism [2]. To integrate the traditional sensor into optical circuits, input/output ports have to be replaced with optical waveguides. Recent progress in sensitive fiber and waveguide SPR provides options for the miniaturization and integration of SPR sensor systems [2].

Recently a highly integrated and sensitive SPR interference sensor or surface plasmon interferometer (hereafter referred to as SPI) based on silicon-on-insulator technology has been proposed in our group [3-4]. The basic element of this sensor is a surface plasmon interferometer consisting of a thin layer of gold embedded in a silicon slab. Surface modes propagate both at the gold-analyte interface (the sensing arm) and at the gold-silicon interface (the reference arm), and they recombine and interfere at the end of the gold layer. It was demonstrated that the device could achieve a sensitivity of 463.5 nm/RIU (refractive index unit) and a resolution of  $1 \times 10^{-6}$  RIU with regards to wavelength interrogation [3]. However, the sensitivity of the sensor is relatively low and thus an improvement to be competitive to the-state-of-the-art devices is needed.

In this chapter, it is found that an enhanced sensitivity of the SPI can be obtained by adding a silicon layer on top of the Au layer.

## VII.1. SPI on SOI

### VII.1.1. Device structure

The cross section of the SPI sensor is depicted in Fig. 7.1. It consists of three sections. The first and third sections are input and output dielectric waveguides, respectively, connected to a light source and a photodetector. The second section with a length  $L_{SPI}$  plays a role of surface plasmon interferometer where the sensing area is established. The interferometer consists of a thin gold (Au) layer embedded into the silicon membrane (with refractive index  $n=3.4764$ ) on top of a supporting silica ( $SiO_2$ ) layer ( $n=1.444$ ). The difference with the structure proposed earlier in our group is the extra deposited Si layer on top of the Au layer.

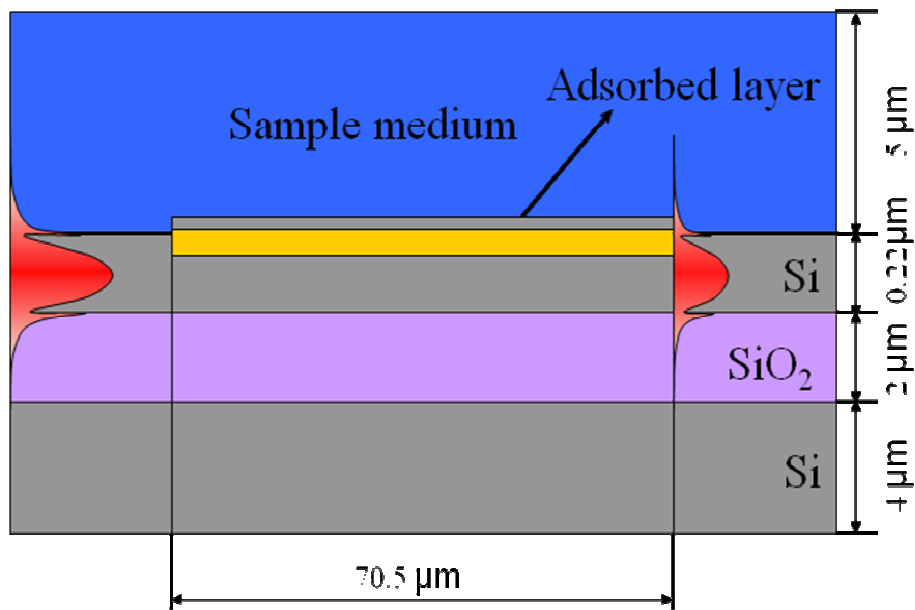


Figure 7.1. Cross section of the SPI sensor on SOI with a 40-nm-thick adsorbed layer.

### VII.1.2. Sensing principle

When TM polarized light arrives at the beginning of the gold layer, it excites two independently propagating surface plasmon modes, which propagate along the top and the bottom interface of the metallic layer. Even though it is covered by a thin Si layer, the phase of the top surface plasmon mode is still influenced by the refractive index of the analyte medium

flowing over the sensor. In contrast, the phase of the bottom surface plasmon mode is insensitive to any refractive index changes. At the end of the gold layer both surface plasmon modes excite the ground mode of the SOI waveguide and, depending on the relative phase of the surface plasmon modes, their contributions to the ground mode will interfere constructively or destructively.

For example, the interferometric nature of the sensor is shown in Fig. 7.2, calculated by an in-house-developed eigenmode expansion solver [5]. In the simulation, the refractive index of Au is described by the Lorentz-Drude model [6]. The transmitted intensity of the fundamental TM mode of the Si slab waveguide is plotted as a function of refractive index of the sensed sample. The operation wavelength is set to  $1.55 \mu\text{m}$ , which is in the near-infrared region and suitable for biosensing applications. When the upper and lower surface plasmon modes arrive in phase at the end of the sensing section of length  $70.5 \mu\text{m}$ , constructive interference leads to maximal transmission, whereas for certain values of sample refractive index the phase difference between the two modes results in destructive interference leading to minima in the transmission spectrum.

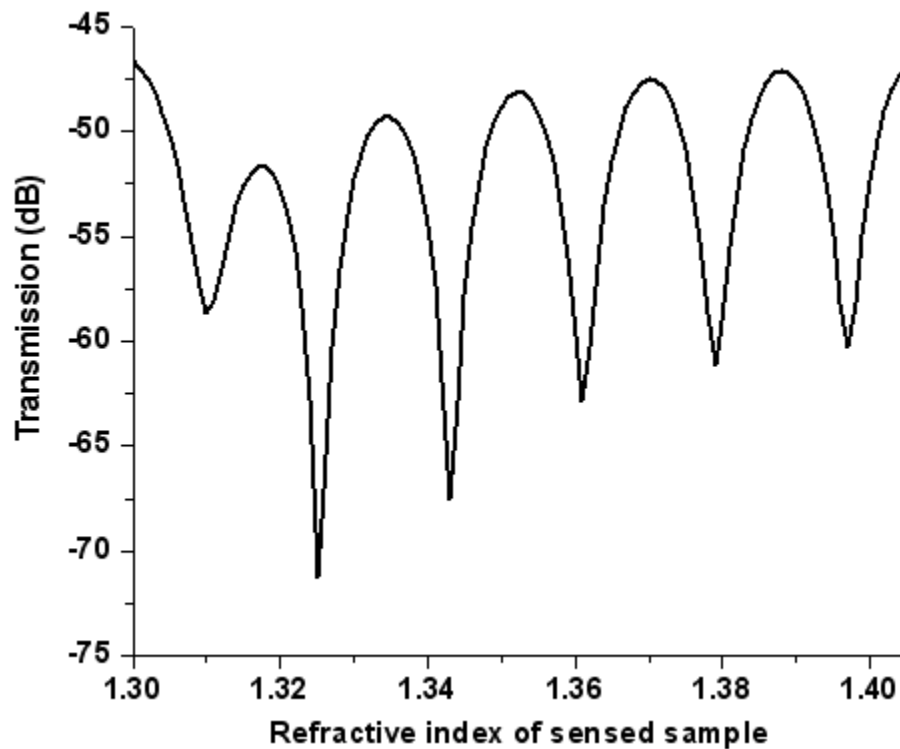


Figure 7.2. Transmission of the sensor depicted in Fig. 7.1 as a function of refractive index of sensed sample.

Besides intensity measurement mode [3] where we use a monochromatic input mode (at a fixed wavelength) and monitor the output power, there also exists a so-called wavelength interrogation mode in this device where a broadband input mode is used and we monitor the position of spectral minima in the transmission spectrum. Therefore, our device can operate in two modes.

## VII.2. Enhanced sensitivity by additional Si top layer

### VII.2.1. Sensitivity enhancement

Using an adsorbed layer to enhance the sensitivity of biosensors was already proposed by Lahav *et al.* [7] to reach a sensitivity enhancement by a factor up to 10 compared to the original SPR sensor based on Kretschmann configuration. In this work, we investigate how a thin adsorbed layer embedded on top of Au layer influences the sensitivity of the interferometric sensor. We also elucidate the mechanisms behind this improvement, which are different from those described in literature.

The bulk sensitivity of an interferometer with spectral interrogation is defined as [8]

$$S_n = \frac{\delta\lambda_{res}}{\delta n_{analyte}} \quad (7.1)$$

where  $\delta\lambda_{res}$  is a shift in the resonance wavelength corresponding to the change  $\delta n_{analyte}$  in the refractive index of analyte.

Apart from the sensitivity, another important parameter that determines the sensor performance is the Q-factor. It determines how accurately  $\delta\lambda_{res}$  can be measured. The higher the Q value, the more accuracy in the measurement of  $\delta\lambda_{res}$  is obtained. The Q-factor is defined as:

$$Q = \frac{\lambda_{res}}{FWHM} \quad (7.2)$$

where FWHM is the full-width at half maximum power.

To compare the overall performance of our sensors, we use the concept of a “figure of merit” (FOM) as the concept covering a detection limit. The higher FOM value, the better performance of sensors is obtained. A typical FOM for these sensors is the ratio of the sensitivity and FWHM given as follows [9]:

$$FOM = \frac{S_n}{FWHM} \quad (7.3)$$

Under the constraint of a constant phase difference the sensitivity can be written as:

$$S_n = \frac{\partial\Phi(\lambda, n_{analyte}) / \partial n_{analyte}}{\partial\Phi(\lambda, n_{analyte}) / \partial\lambda} \quad (7.4)$$

with

$$\frac{\partial\Phi(\lambda, n_{analyte})}{\partial\lambda} = \frac{2\pi L_{SPI}}{\lambda} (n_{g,s} - n_{g,r}), \quad (7.5)$$

$n_{g,s}$  and  $n_{g,r}$  are the group indexes of the sensing and reference waveguides.

This sensitivity is strongly dependent on the group index difference of the top and bottom SP modes of the interferometer. As the difference between the group indexes ( $\Delta n_g$ ) becomes smaller, the sensitivity becomes substantially larger. To improve the sensitivity, one of the best options is making the two modes more alike, which can be accomplished by adding a thin Si layer on top of the Au layer. It can be seen in Fig. 7.3 that the difference between the group indexes of the two modes is smaller than those of our previous sensor.

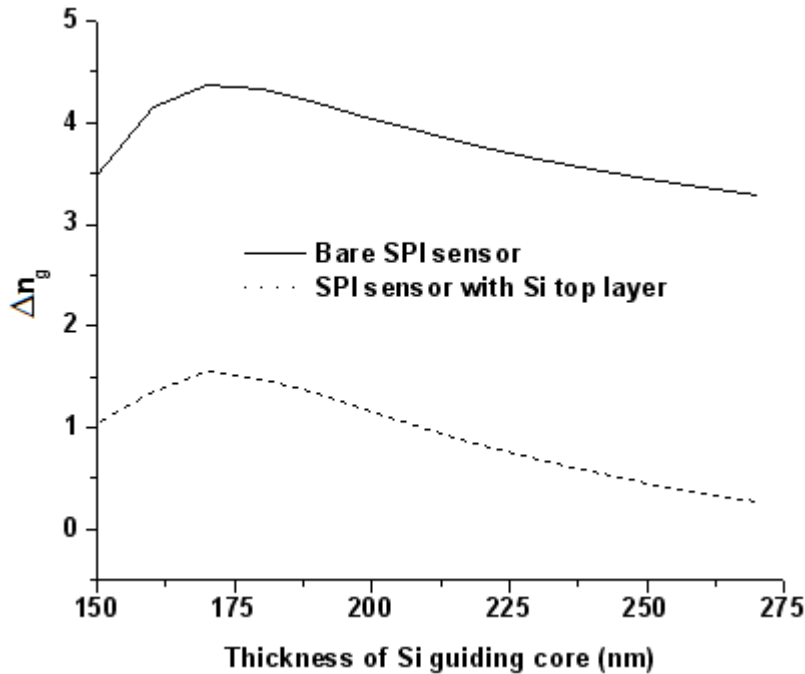


Figure 7.3. Difference of top and bottom surface plasmon modes' group indexes of the interferometer with respect to thickness of Si membrane.

To specify the improved sensitivity of the sensor and to demonstrate that the best material added on top is Si, we calculate the sensitivity with respect to various refractive indexes of the additional top layer. The first structure investigated has a 70-nm-thick Au layer embedded into a 220-nm-thick silicon membrane with 70.5- $\mu\text{m}$ -long sensing area. For each refractive index of the 40-nm-thick additional top layer, we monitor the shift of transmission minima for different analytes in order to calculate the sensitivity of the sensor. We found that the highest sensitivity is 5750 nm/RIU (refractive index unit) with a corresponding refractive index of the additional top layer of 3.476 as seen in Fig. 7.4. This index is the one of Si, again giving evidence for the theory that making the interferometer more symmetrical is the reason for the improvement. The corresponding Q-factor and FOM of the new sensor are 105 and 383 ( $\text{RIU}^{-1}$ ), and that of the old one are 171 and 56 ( $\text{RIU}^{-1}$ ), respectively. It is seen that the overall performance of the new sensor is better than the old one.

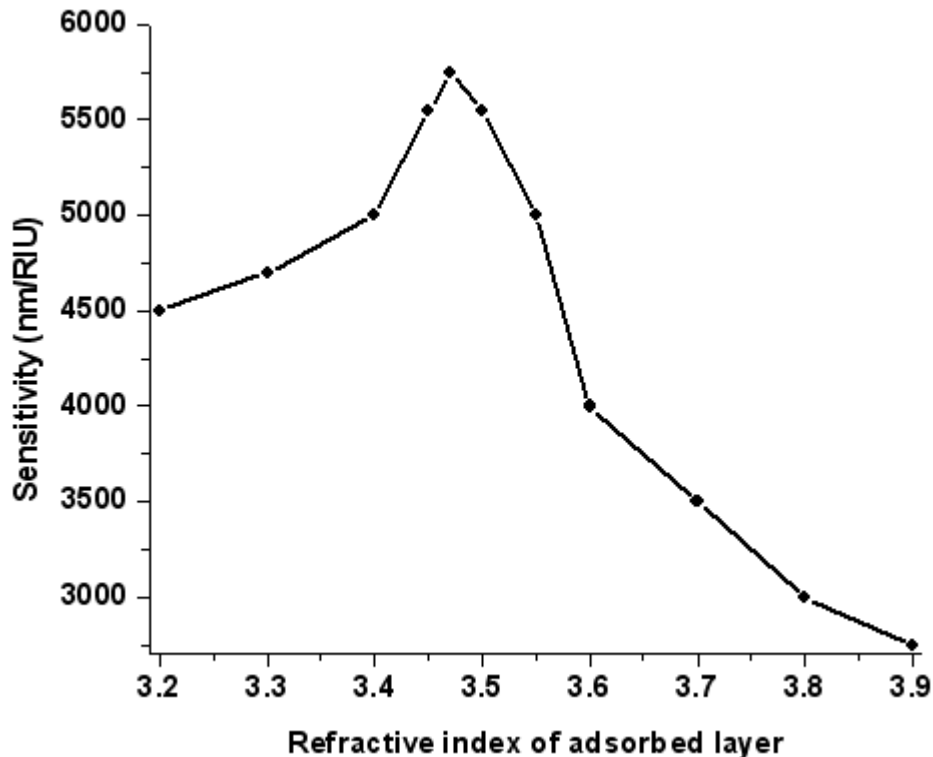


Figure 7.4. Sensitivity of the sensor as a function of refractive index of additional adsorbed layer.

## VII.2.2. Optimization: towards chip-scale sensors

However, since the length of the sensor is relatively long, it is not suitable for densely integrated on-chip applications where the size of the sensor should be as small as possible. We now turn to optimize the device to obtain a small sensor with high sensitivity. The optimization of the sensor consists of determining the best values of the thickness of Si guiding core ( $d_{\text{core}}$ ), the length of sensing area ( $L_{\text{SPI}}$ ), thickness of Au and Si top layer. The selection of those parameters is done such that the transmission of the sensor reaches its minimum at a wavelength of 1.55  $\mu\text{m}$ . The minimum appears when the interference of two plasmon modes is totally destructive and both modes carry the same amount of power. These two conditions lead to the fact that the optimal length of the sensor has to satisfy the two following equations [8]:

$$2(\phi_{b0} - \phi_{t0}) - (k_r^{b0} - k_r^{t0})L_{\text{SPI}} = (2m + 1)\pi, \quad (7.6)$$

$$L_{\text{SPI}} = \frac{1}{k_i^{t0} - k_i^{b0}} \ln \left( \frac{|T_{b0}|^2}{|T_{t0}|^2} \right), \quad (7.7)$$

where  $\phi_{b0}$  and  $\phi_{t0}$  are the phase difference due to the coupling of the incoming silicon waveguide mode to the bottom SP mode and the top SP mode, respectively.  $T_{b0}$  and  $T_{t0}$  are the transmission coefficients of the incoming dielectric mode to the bottom and the top SP modes at the chosen wavelength or refractive index for which the transmission should be minimal, and  $k_r^{b0}$ ,  $k_i^{b0}$ ,  $k_r^{t0}$  and  $k_i^{t0}$  are the real and imaginary parts of the  $k$ -vector of the bottom and top SP modes, respectively.

Eq. (7.6) provides us various possible phase lengths corresponding to the order of the interference effect with  $m=0,1,2,\dots$  and Eq. (7.7) only gives us one single possible power length. The intersection of phase lengths and power length results in optimal pairs ( $L_{\text{SPI}}$ ,  $d_{\text{core}}$ ) of the sensing length and the Si core thickness. For example, with a given thickness of additional Si top layer and Au layer, the phase lengths and the power length as a function of the sensing length and the Si core thickness are depicted in Fig. 7.5. Since there exist various optimal pairs ( $L_{\text{SPI}}$ ,  $d_{\text{core}}$ ), the most optimal one is chosen such that the highest sensitivity and Q-factor is obtained.

Following these design rules, we now seek the most optimal pairs ( $L_{\text{SPI}}$ ,  $d_{\text{core}}$ ) of the SPI sensor as a function of the thicknesses of the Si top layer and the Au layer. Since we aim at small sensors with length shorter than 15  $\mu\text{m}$ , we only choose certain thickness of the Si top layer and

the Au layer. Each time for the optimal pair ( $L_{SPI}$ ,  $d_{core}$ ), the sensitivity and Q-factor of the sensor as a function of the thickness of Si top layer with various Au layers is depicted in Fig. 7.6 (a) and (b), respectively. For each Au layer, the highest sensitivity is found for a given thickness of the Si top layer. It is seen that the highest sensitivity and Q-factor are found for a 35-nm-thick Si top layer and a 60-nm-thick Au layer. The corresponding optimal pair ( $L_{SPI}$ ,  $d_{core}$ ) of the SPI sensor is (15.02  $\mu\text{m}$ , 109.6 nm). The optimal value is this result of a trade-off between two effects: the thicker the additional Si layer, the more symmetrical the system becomes, but the smaller the effect of the liquid on the phase of the top mode will be.

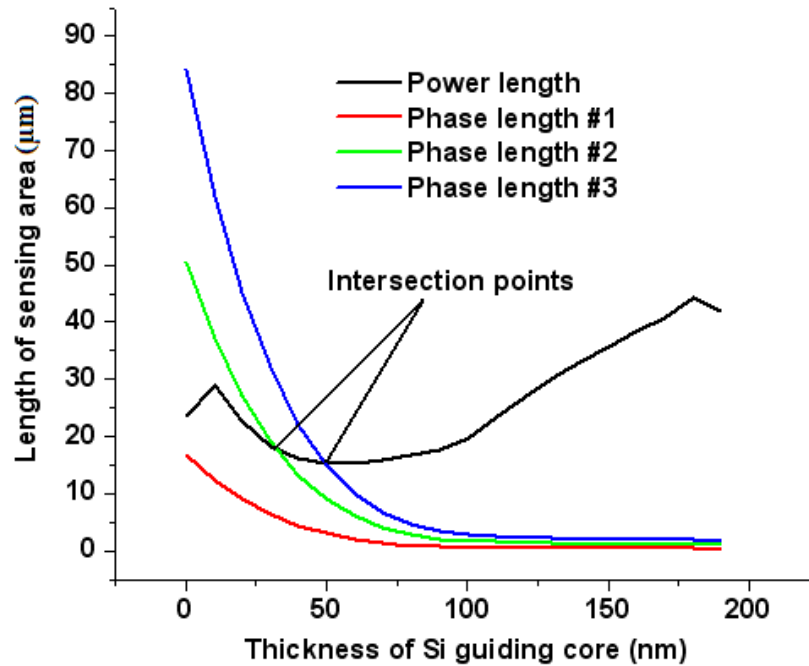


Figure 7.5. Phase lengths and power length of the sensor as a function of thickness of Si waveguide core. The thickness of Au and Si top layer is 60 nm and 35 nm, respectively.

For comparison, the most optimal pair ( $L_{SPI}$ ,  $d_{core}$ ) of the bare SPI sensor is found at (5.63  $\mu\text{m}$ , 140.4 nm). The sensitivity of the optimized sensor with 35-nm-thick Si top layer is around 2500 nm/RIU and that of the bare sensor is around 750 nm/RIU. The transmission spectra of the sensors as a function of wavelength are depicted in Fig. 7.7. The Q-factor of the bare sensor is around 207 while that of the sensor with Si top layer is 148. Following Eq. (7.3), the FOM of the bare sensor has a value of 100 ( $\text{RIU}^{-1}$ ) while that of the sensor with Si top layer is 237 ( $\text{RIU}^{-1}$ ). It implies that the new sensor with the most optimal pair ( $L_{SPI}$ ,  $d_{core}$ ) has better performance than the old one.

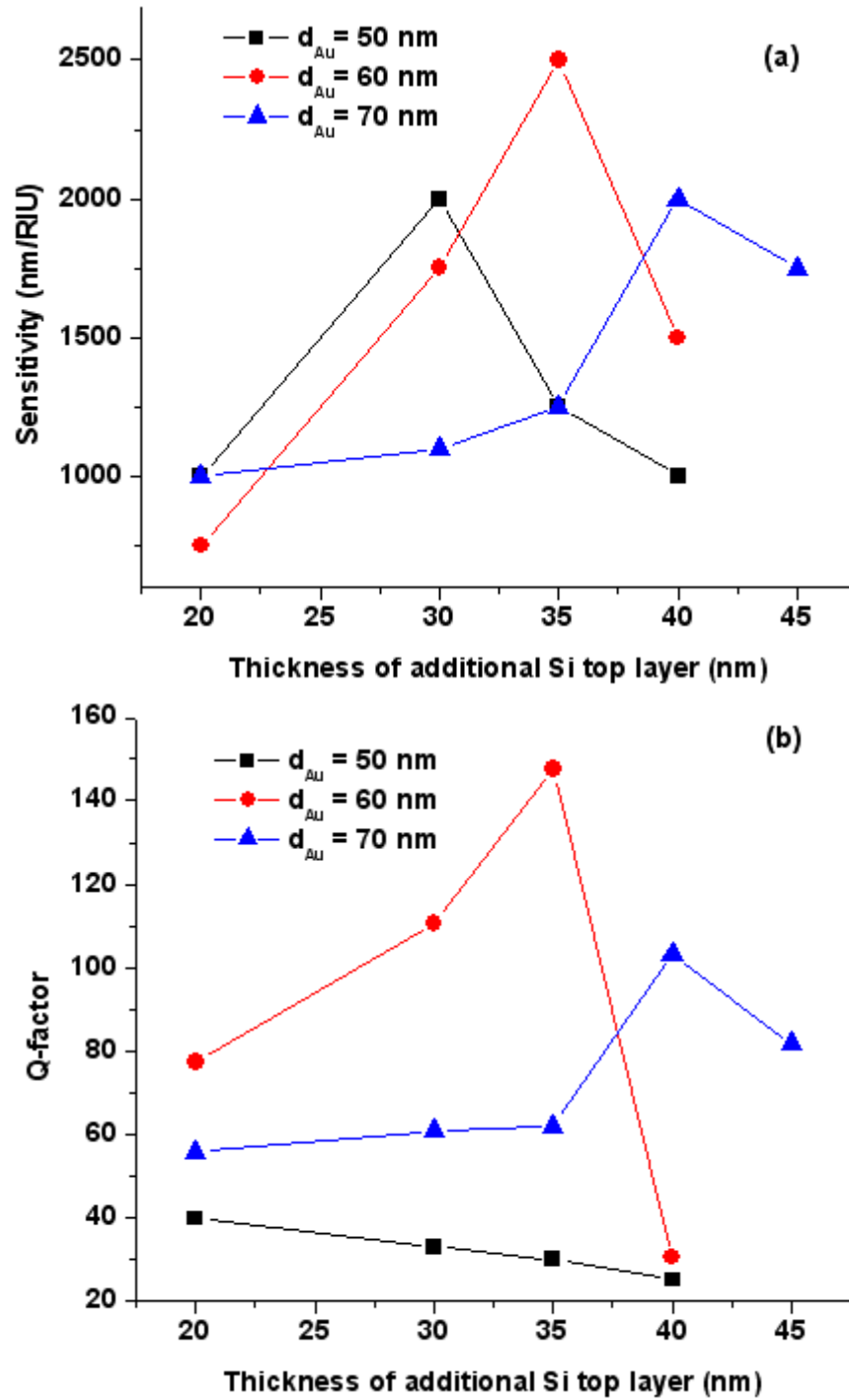


Figure 7.6. Sensitivity (a) and Q-factor (b) as a function of thickness of Si top layer with various Au layer thicknesses, each time for the optimal core thickness and sensor length.

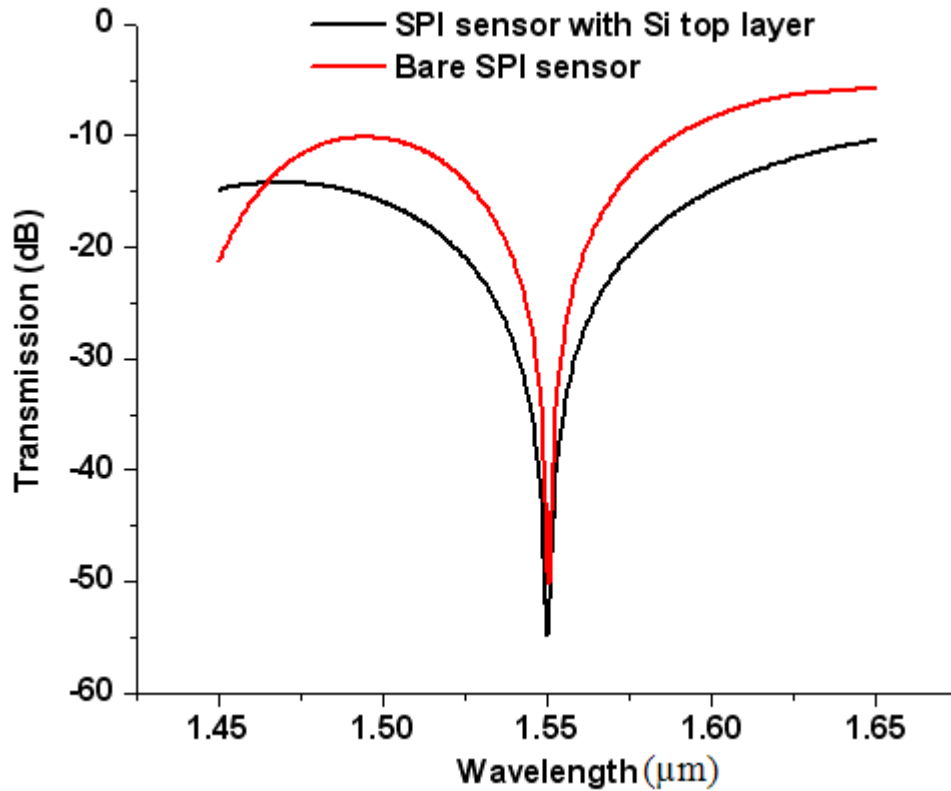


Figure 7.7. Transmission as a function of wavelength. Simulation results for the most optimized structure.

Apart from bulk sensing, the new configuration, which makes the interferometer more symmetrical, also helps to enhance the sensitivity of the device for surface sensing. To model surface sensing, we simulate the response when adding layers of avidin (index 1.45) of different thickness. In reality, complete saturation of the device with avidin, when all the binding sites at the surface are occupied, will be reached for an additional 5 nm layer [10]. It is found that the red shift for such a thin layer of the new sensor is 6.5 nm. The same shift for the original one is only 0.5 nm. The red shift with respect to thickness of the added avidin layer is depicted in Fig. 7.8. It is seen that the resonance wavelength is linearly shifted as a function of the thickness of the added avidin layer.

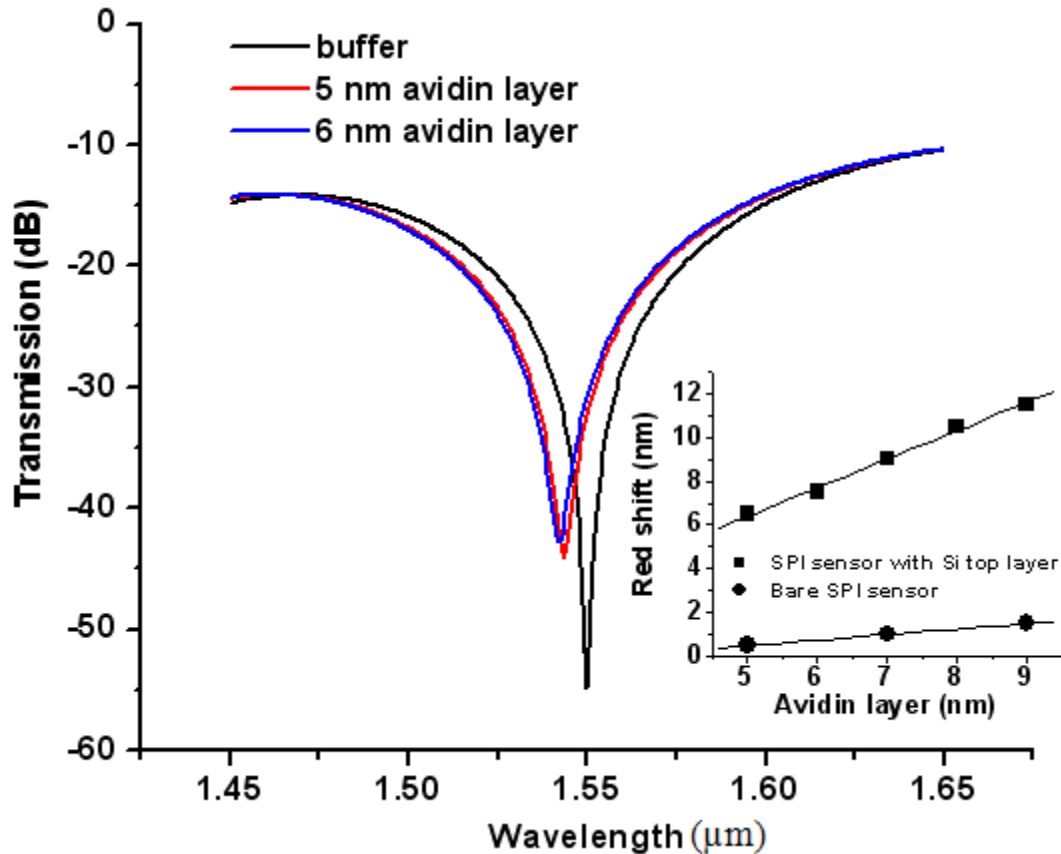


Figure 7.8. Transmission of sensors as a function of wavelength. Inset is red shift for various avidin layers.

### VII.3. Conclusion

In this chapter, we have proposed the use of a Si top layer to make the interferometer more symmetrical to enhance the sensitivity of the surface plasmon interference biosensor on silicon-on-insulator. It was found that with a 35 nm Si layer added on top of a 60 nm Au layer a high sensitivity and FOM of the surface plasmon interference sensor with optimal length of 15.02  $\mu\text{m}$  can be obtained at 2500 nm/RIU and 237 ( $\text{RIU}^{-1}$ ), respectively.

# References

1. J. Homola, S. Yee, and G. Gauglitz, "Surface plasmon resonance sensors: review," *Sens. Actuators B Chem.* **54**, 3–15 (1999).
2. X. D. Hoa, A. G. Kirk, and M. Tabrizian, "Towards integrated and sensitive surface plasmon resonance biosensors: a review of recent progress," *Biosens. Bioelectron.* **23**, 151-160 (2007).
3. P. Debackere, S. Scheerlinck, P. Bienstman, and R. Baets, "Surface plasmon interferometer in silicon-on-insulator: novel concept for an integrated biosensor," *Opt. Express* **14**, 7063-7072 (2006).
4. P. Debackere, R. Baets, and P. Bienstman, "Bulk sensing experiments using a surface plasmon interferometer," *Opt. Letts.* **34**, 2858-2860 (2009).
5. CAMFR, <http://camfr.sourceforge.net>
6. A. D. Rakic, A. B. Djurusic, J. M. Elazar, and M. L. Majewski, "Optical properties of metallic films for vertical-cavity optoelectronic devices," *App. Opt.* **37**, 5271-5283 (1998).
7. A. Lahav, M. Auslender, and I. Abdulhalim, "Sensitivity enhancement of guided-wave surface-plasmon resonance sensors," *Opt. Letts.* **33**, 2539-2541 (2008).
8. P. Debackere, "Nanophotonic biosensor based on surface plasmon interference," PhD Thesis, Ghent University, 2010, 4-22-4-36.
9. L. J. Sherry, S-H Chang, G. C. Schatz, R. P. Van Duyne, B. J. Willey, and Y. Xia, "Localized surface plasmon resonance spectroscopy of single Silver nanocubes," *Nano Letts.* **5**, 2034-2038 (2005).
10. T. Claes, J. G. Morela, K. De Vos, E. Schacht, R. Baets, and P. Bienstman, "Label-free biosensing with a slot-waveguide-based ring resonator in silicon-on-insulator," *IEEE Photon. J.* **1**, 197-204 (2009).

# Chapter VIII

## Enhanced light emission of Silicon LEDs with plasmonic nanoparticles

Silicon-on-insulator (SOI) light-emitting diodes (LEDs) are very promising light sources for optical communication technologies. However, the development of these components is hampered by their low efficiencies. Efforts to improve this have amongst others made use of plasmonic nanostructures [1]. Large efficiency enhancement of luminescence was achieved by placing metal nanoparticles close to light emitters. This has attracted intense research interests devoted to demonstrating such an enhancement in various media [2-3]. Since the surface plasmon resonance frequency is determined by various parameters such as shape, size and distribution of nanoparticles, an accurate theoretical model is very important in the design of nanoparticle enhanced light emitters.

There exist various methods developed to investigate the efficiency enhancement of electroluminescence. Among these, the recently introduced method based on the effective mode volume theory is known as a systematic and rigorous model to predict emission enhancement of quantum well LEDs in the vicinity of metal nanoparticles [4]. However, the method fails to explain the experimental results of enhanced light emission of SOI-LEDs due to silver (Ag) nanoparticles. While the experiment demonstrated that a significant enhancement in electroluminescence was obtained at the average particle radius of 50-70 nm [1], the optimal radius predicted by the effective mode volume theory (referred to as the conventional approach hereafter in this chapter) is only around 20-30 nm. We attribute this to the use of the Drude approximation in determining the enhanced Purcell factor. To overcome this problem, we propose to use the Drude-Lorentz model for metal dispersion, which is well-known as a more accurate model [5]. We also combine this with a calculation without approximations of the enhanced Purcell factor. The calculated results by the improved approach are shown to be in very good agreement with the experiment.

Furthermore, a random assembly of isolated nanoparticles may hold an advantage over the ordered arrays for light emitting devices of finite area [4]. In this chapter, a theoretical model for the optical properties of such nanoparticles using the effective medium theory as means for

optimal design of light emitters is presented. The validity of the model is tested via a comparison to the Mie theory.

The results of this chapter have been published in [6].

## VIII.1. An improved model of plasmonic nanoparticle enhanced light emitters

The theoretical model employed to evaluate the radiation enhancement of SOI-LEDs is often described as a two-step process. The first step is an energy transfer from matter to a surface plasmon-polariton (SPP) mode at the metal-dielectric interface. Owing to the high mode density in the SPP, the Purcell factor  $F_p$  [7] is significantly enhanced. The second step is a transfer of the energy from the confined SPP modes to actual propagation modes with a certain coupling rate, and this process competes with nonradiative loss due to absorption in metal nanoparticles. Typically, tightly-confined large wavevector SPPs are more difficult to couple to the outside world. Hence, the overall radiative efficiency from the excited matter to the free-propagating wave has a complicated dependence on the SPP characteristics. It was shown that for a given original radiative efficiency  $\eta_{\text{rad}}$  we can determine an exact value of the SPP enhancement [4].

The geometry of isolated metal nanospheres being placed on top of an SOI-LED is shown in Fig. 8.1. The effective volume of the SP mode supported by a metal sphere is given as follows [4]:

$$V_{\text{eff}} = \frac{4}{3} \pi a^3 \left( 1 + \frac{1}{2\epsilon_D} \right) \quad (8.1)$$

with  $a$  being the radius of the nanoparticle and  $\epsilon_D$  being the dielectric constant of the surrounding medium.

For a dipole positioned at a distance  $d$  from the particle surface and oriented in the  $z$  direction normal to the surface, the effective density of the SP modes is

$$\rho_{SP} = \frac{L(\omega)}{V_{\text{eff}}} \left( \frac{a}{a+d} \right)^6, \quad (8.2)$$

where the normalized line shape of the dipole oscillation is

$$L(\omega) = \frac{\text{Im}[(\varepsilon_M(\omega) + 2\omega_D)^{-1}]}{\int \text{Im}[(\varepsilon_M(\omega) + 2\omega_D)^{-1}] d\omega} \quad (8.3)$$

with  $\varepsilon_M$  being the metal dispersion. In [4], Eq. (8.3) was calculated by a Drude approximation. This is the main reason the method failed to explain the enhancement of the light emission from SOI-LEDs due to large nanoparticles. However, this can be remedied by considering the more accurate Lorentz-Drude model [5] combined with no approximation of the line shape of the dipole oscillation, which is performed in this work.

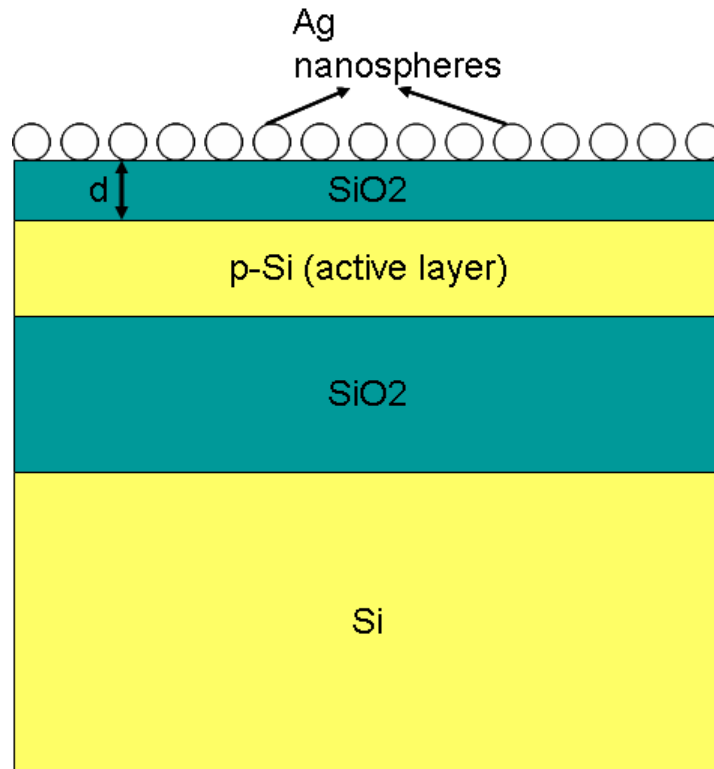


Figure 8.1. Geometry of silicon-on-insulator LEDs with Ag nanospheres embedded on top.

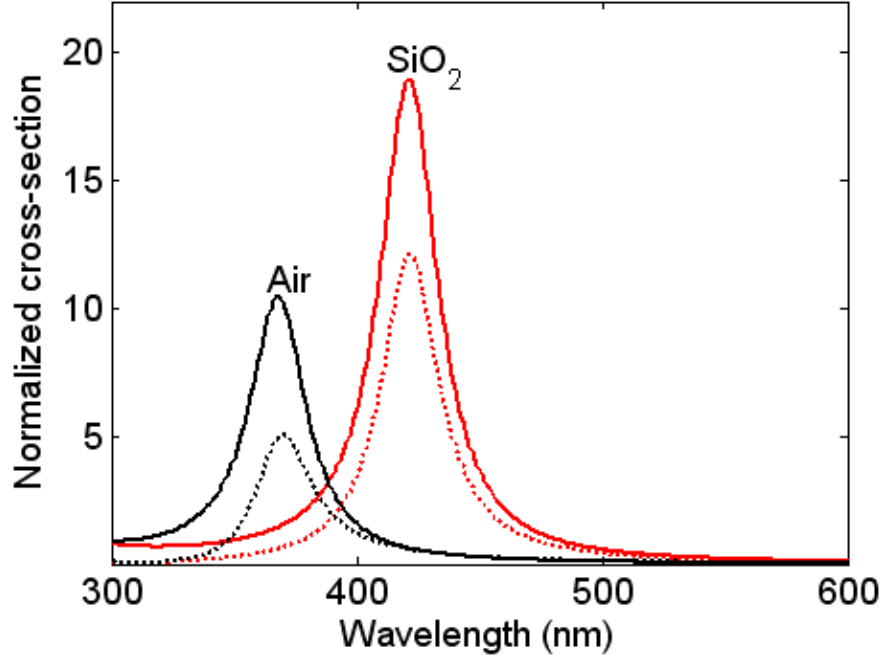


Figure 8.2. Scattering (solid lines) and absorption (dotted lines) cross-sections for a 60 nm diameter Ag sphere embedded in air (black) and SiO<sub>2</sub> (red) normalized by the projected area of the sphere.

For Ag nanoparticles embedded in a silica (SiO<sub>2</sub>) medium, the enhanced fields that occur near metal particles as a result of the SP resonance give rise to an enhanced absorption. According to a generalized form of Kirchhoff's law which is valid for luminescent emission, enhanced absorption corresponds to an enhanced emission [1]. Figure 8.2 shows the scattering and absorption cross-sections for 100 nm diameter of Ag sphere embedded in air and SiO<sub>2</sub> calculated by Mie theory [8]. Cross sections are normalized to the geometry particle cross section. For each embedding medium, a dipole resonance is observed. At the resonance frequency  $\omega_0$ , the Purcell factor  $F_p(\omega_0)$  can be estimated as the ratio of the effective density of the SP modes to that of the radiation components as follows [4]:

$$F_p(\omega_0) = \frac{\rho_{SP}}{\rho_{rad}} = \frac{L(\omega_0)}{V_{eff}} \left( \frac{a}{a+d} \right)^6 \left[ \frac{1}{3\pi^2} \left( \frac{2\pi}{\lambda_D} \right)^3 \frac{1}{\omega_0} \right]^{-1}, \quad (8.4)$$

with  $\lambda_D = \lambda/n$  being the emission wavelength in the dielectric.

Now, with a given original radiative efficiency, the expression for the enhancement factor due to a single metal nanoparticle is described as [4]:

$$F_{\text{single}} = \frac{\eta_{SP}}{\eta_{rad}} = \frac{1 + F_p \eta_{pr}}{1 + F_p \eta_{rad}}, \quad (8.5)$$

where  $\eta_{pr}$  is the radiative coupling efficiency of the SP mode. For an example of InGaN quantum well LEDs, with isolated silver nanoparticles placed in close proximity to the active region, it was shown that the output enhancement due to isolated silver nanoparticles is significant while only modest enhancement can be achieved with an ordered array of nanoparticles. It was shown that a random assembly of isolated particles may hold an advantage over the ordered arrays for light emitter devices of finite area [4]. Therefore, we investigate this further in the next section.

## VIII.2. Optical properties of a random assembly of nanoparticles

While the optical scattering and absorption efficiency determine the conversion of the incident light into the corresponding quantities, they give no information about the directionality of the scattered field. Through the transmission and reflection of light interacting with nanoparticles a better understanding of the process can be obtained. Using the effective medium theory the transmission and reflection of light through a random assembly of nanoparticles can be assumed to be described by those through a slab of nanoparticles.

In this case the optical properties of the slab of non-interacting nanospheres embedded in the host material are well-described by the Maxwell-Garnet theory based on the concept of mean-field inside and outside the nanoparticles. With a low volume filling fraction ( $f$ ) of isolated nanoparticles, the effective dielectric permittivity is given by [9]

$$\varepsilon_{eff} = \left[ \frac{1 + 2f\gamma}{1 - f\gamma} \right] \varepsilon_m, \quad \gamma = \frac{\varepsilon_p - \varepsilon_m}{\varepsilon_p + 2\varepsilon_m}, \quad (8.6)$$

and the reflection and transmission of the slab of nanoparticles with an assumption of normal light incidence are calculated by

$$R = \left| \frac{r(1 - \exp(ikn_{eff}h))}{1 - r^2 \exp(ikn_{eff}h)} \right|^2, \quad m = \frac{n_{eff}}{n_m}, \quad r = \frac{1 - m}{1 + m}, \quad (8.7)$$

$$T = \left| \frac{4m \exp(-ikn_m h)}{(1 + m)^2 [\exp(-ikn_{eff}h) - r^2 \exp(ikn_{eff}h)]} \right|^2, \quad (8.8)$$

where  $k$  is the wavevector of an electromagnetic wave propagating in free space,  $n_m$  and  $n_{eff}$  are the refractive index of the surrounding medium and the effective refractive index of the slab of nanoparticles, respectively, and  $h$  is the slab thickness.

To validate the model the calculated transmission and reflection coefficients are compared to those obtained by the Mie theory. For small values of the surface coverage ( $\eta \ll 1$ ), the transmission and reflection rates of the layer of nanoparticles can be calculated using the Mie cross-sections backward scattering and absorption efficiencies where multiple scattering has been neglected due to the low surface coverage [10]. Figure 8.3 shows the transmission and reflection coefficients (with  $\eta=0.02$  and  $f=0.01$ ) calculated by these two methods. From the figure a good agreement between those methods is found as a means to confirm the validity of the proposed model using the effective medium theory. The same figure shows that at the resonance frequency the low transmission and reflection coefficients lead to a high extinction (scattering plus absorption) efficiency ( $E=1-T-R$ ). That condition favors an enhancement of the radiative efficiency of LEDs.

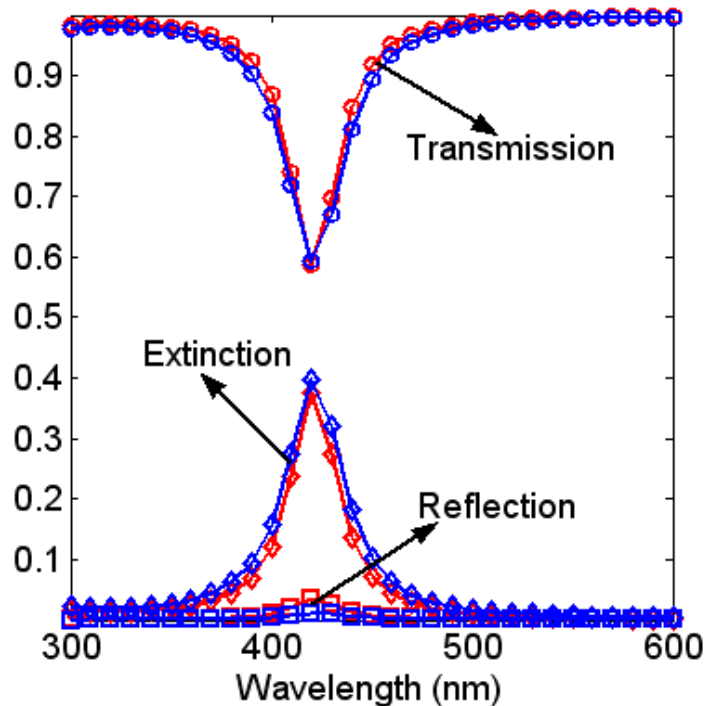


Figure 8.3. Spectra of the transmission and reflection for slab of 60 nm diameter Ag particles embedded in SiO<sub>2</sub> calculated by the effective medium theory (red lines) and the Mie theory (blue lines).

### VIII.3. Enhanced light emission of silicon LEDs by isolated nano-particles

In this section, we employ the developed model to evaluate the enhancement of the electroluminescence efficiency of silicon LEDs in which the active layer is placed in the vicinity of an isolated Ag nanoparticle. The distance  $d$  from the active layer to a Ag particle is 35 nm as in the LED devices used in the experiments described in [11]. The calculated enhancement factor ( $F_{\text{single}}$ ) of the electroluminescence efficiency for a range of the original radiative efficiency of the emitter is shown in Fig. 8.4 as a function of the sphere radius.

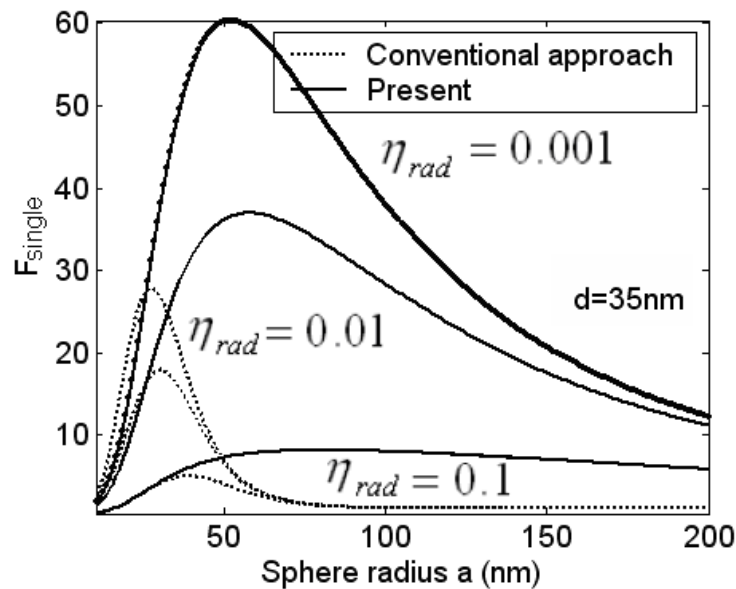


Figure 8.4. Enhancement due to a single Ag sphere on SOI-LEDs with a distance of 35 nm from active layer to metal layer as a function of sphere radius for various original radiative efficiencies calculated by the conventional approach (dotted lines) and the present approach (solid lines).

It can be seen that the enhancement factor exhibits a strong dependence on the nanosphere dimensions, with the peak occurring when the radius is small enough to yield smaller effective mode volume for an enhanced Purcell factor, yet is still sufficiently large to assure strong radiative coupling of the SP mode. Furthermore, it is seen that the higher the original radiative efficiency, the more important the concern for the efficient energy transfers from the SP mode into free-space radiation modes. This situation favors larger nanoparticles that can emit the SP energy photons into free space prior to getting lost in the metal. At the emission wavelength of

900 nm, the enhancement of electroluminescence efficiency calculated by the present method occurs for a particle radius of around 50-60 nm, which is in very good agreement with the experimental results reported in [11], whereas the optimal radius obtained from the conventional approach is only 20-30 nm.

In addition, Figure 8.5 shows the calculated enhancement factor of the electroluminescence efficiency as a function of emission wavelength. It is seen that for a given original radiative efficiency of 0.1, the best enhancement factor is observed at a wavelength of around 890 nm. It is in good agreement with the experimental result of around 900 nm, while the conventional method predicted best enhancement at a wavelength of around 1330 nm. The big difference can be explained that the refractive index of silver calculated by the Drude model is very different from the Drude-Lorentz model. As seen in Fig. 8.6, the refractive index calculated by the Drude-Lorentz model is very well-fitted to the experimental results (experimental data taken from Palik's handbook in [12]), whereas those obtained by the Drude model is very poor-fitted to the experimental results, especially for shorter wavelengths. That is the main reason which causes the conventional method used the Drude model did not correspond to the experimental result.

A single nanosphere may enhance light emission of only a very small emitter. Therefore, with the optimal particle sizes found, one can consider disordered arrays of these isolated nanospheres to achieve practical enhancement of devices such as SOI-LEDs.

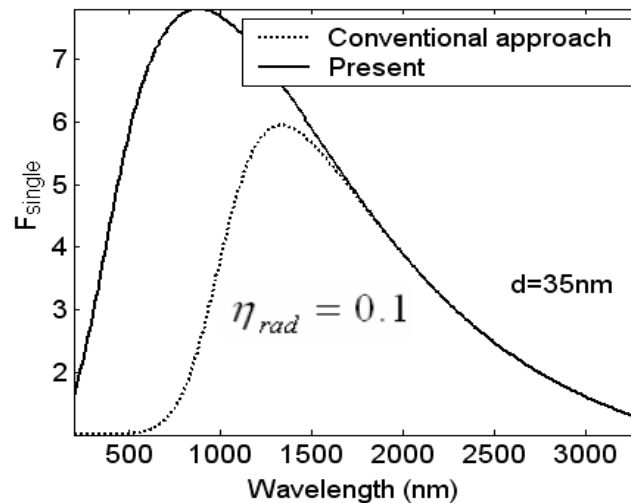


Figure 8.5. Enhancement due to a single Ag sphere on SOI-LEDs with a distance of 35 nm from active layer to metal layer as a function of emission wavelengths calculated by the conventional approach (dotted line) and the present approach (solid line).

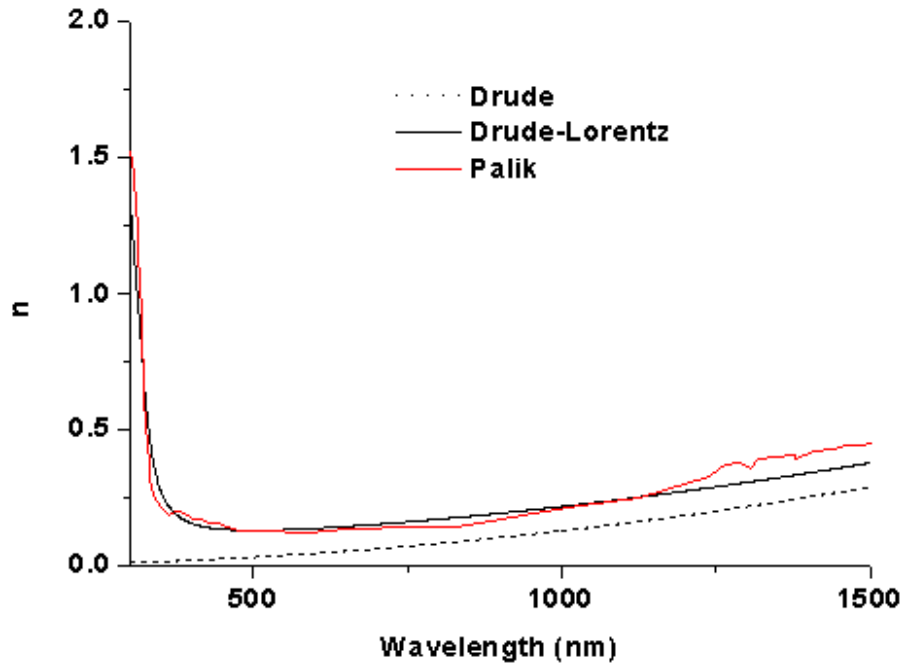


Figure 8.6. Real part of refractive index of Ag calculated by the Drude model, the Drude-Lorentz model and the experimental result (data taken from Palik's handbook in [12]), respectively.

## VIII.4. Conclusion

In this chapter, the systematic and rigorous model based on the effective volume mode theory has been improved to evaluate the enhancement of the electroluminescence efficiency of SOI-LEDs due to isolated Ag nanoparticles. The improved model has well explained the plasmonic enhanced light emission of SOI-LEDs as reported in an experiment. In addition, the effective medium theory has been proposed for modeling optical properties of a random assembly of nanoparticles. Hence, it is very useful for the design of metal nanoparticle enhanced light emitters.

# References

1. K. R. Catchpole and S. Pillai, "Surface plasmons for enhanced silicon emitting diodes and solar cells," *J. Lumin.* **121**, 315-318 (2006).
2. K. Okamoto, I. Niki, A. Shvartser, Y. Narukawa, T. Mukai, and A. Scherer, "Surface-plasmon-enhanced light emitters based on InGaN quantum wells," *Nature Mat.* **3**, 601-605 (2004).
3. S. Kuhn, U. Hakason, L. Rogobete, and V. Sandoghdar, "Enhancement of single-molecule fluorescence using a gold nanoparticle as an optical nanoantenna," *Phys. Rev. Lett.* **97**, 017402 (2006).
4. G. Sun, J. B. Khurgin, and R. A. Soref, "Plasmonic light-emission enhancement with isolated metal nanoparticles and their coupled arrays," *J. Opt. Soc. Am. B* **25**, 1748-1755 (2008).
5. A. D. Rakic, A. B. Djurusic, J. M. Elazar, and M. L. Majewski, "Optical properties of metallic films for vertical-cavity optoelectronic devices," *App. Opt.* **37**, 5271-5283 (1998).
6. Khai Q. Le and P. Bienstman, "Optical modeling of plasmonic nanoparticles enhanced light emission of silicon light-emitting diodes," *Plamronics* (2010).
7. M. Purcell, "Spontaneous emission probabilities at radio frequency," *Phys. Rev.* **69**, 681 (1946).
8. C. F. Bohren and D. R. Huffman, *Absorption and scattering of light by small particles* (Wiley-Interscience, New York, 1993).
9. D. C. Kohlgraf-Owen and P. G. Kik, "Numerical study of surface plasmon enhanced nonlinear absorption and refraction," *Opt. Express* **16**, 10823-10834 (2008).
10. Y. A. Akimov, K. Ostrikov, and E. P. Li, "Surface plasmon enhancement of optical absorption in thin-film silicon solar cells," *Plasmonics* **4**, 107-113 (2009).
11. S. Pillai, K. R. Catchpole, T. Trupke, G. Zhang, J. Zhao, and M. A. Green, "Enhanced emission from Si-based light-emitting diodes using surface plasmons," *Appl. Phys. Lett.* **88**, 161102 (2006).
12. E. D. Palik, "Handbook of optical constants of solids," Academic Press: Orlando, FL, 1985.

# Chapter IX

## Enhanced light absorption of thin-film silicon solar cells by plasmonic core-shell nanostructures

The interaction of light waves with nanostructures, leading to enhanced light emission and absorption is a key question in the development of optical devices such as light-emitting diodes and solar cells (SCs) [1-3]. Efficient thin-film SCs based on microcrystalline silicon ( $\mu\text{-Si}$ ) or amorphous silicon ( $\text{a-Si}$ ) with broadband absorption require that the thickness of the active layer should be at least a few micrometers. Unfortunately, this is unfeasible due to high, defect-related carrier recombination [4]. Therefore, it is crucial to enhance light absorption in thin-film Si SCs.

In the past few years, many techniques have been proposed to enhance light absorption. One of the most widely used techniques is the light-trapping or light-incoupling technique based on scattering surface textures [5-7]. In addition, resonant enhancement of the near-field and increased scattering cross section via the excitation of surface plasmon polaritons on metallic nanostructures are widely used as well [8-11].

In this chapter, another promising approach to enhance light absorption in the active layer of  $\text{a-Si}$  SCs is proposed, which we presented in [12]. It is done by placing plasmonic core-shell nanostructures consisting of a silica ( $\text{SiO}_2$ ) core coated with a silver (Ag) shell, on top of thin-film  $\text{a-Si}$  SCs. We evaluate the scattering properties of this core-shell structure with Mie theory in 3D using a calculation tool made by Charamsinou *et al.* [13]. Then, the calculation for the absorption enhancement of SCs using core-shell antennas is carried out. It is found that the core-shell particle results in a significantly broad and strong scattering cross section (scattering efficiency above 3 in the 400-800nm wavelength range), making it possible to achieve broadband absorption enhancement. In order to demonstrate this enhancement mechanism, 2D COMSOL simulations of  $\text{a-Si}$  solar cells with core-shell antennas are presented. This work was done in collaboration with Aimi Abass from the Department of Electronics and Information Systems, Ghent University.

## IX.1. Optical properties of a single core-shell nano-antenna

A core-shell nano-antenna structure would make a good tool to boost absorption in a solar cell, as compared to pure metal nanoparticles, simply because of the fact that we have more freedom in tuning the resonances in the core-shell structure. Indeed, it is possible to tune the resonance of the nanoparticle while maintaining its total size [14]. With this, it is possible to make these particles scatter incoming light evenly and efficiently in the active material, in a wavelength region of our choosing, while still having their size relatively small so as to limit reflections. These core-shell structures are therefore promising for boosting absorption in solar cells with thickness in the range of hundred of nanometers. The fact that these antennas only have metal in their shell, not throughout the structure, also leads to less absorption of light by the metal.

The goal of this work is to use the core-shell nano-antennas as scatterers to spread light evenly and effectively in the active material. One therefore should look at the scattering and absorption characteristics of these antennas. To study them, the analytical Mie scattering theory is used to calculate the scattering  $\sigma_s$  and the absorption  $\sigma_a$  efficiency. The scattering and absorption efficiency are the fraction of light scattered on and absorbed by the antenna. They are calculated by normalizing the scattering and absorption cross section with the geometrical cross section of the antenna [2].

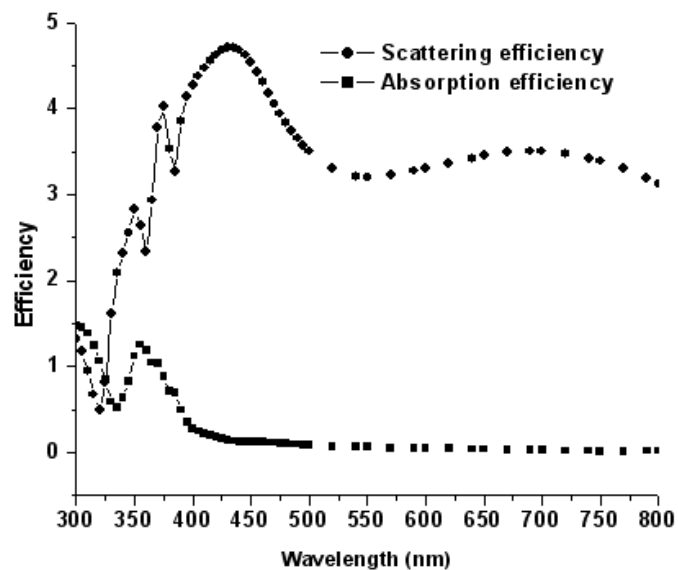


Figure 9.1. Scattering and absorption efficiency for a 34 nm radius  $\text{SiO}_2$  core and 28 nm thick Ag shell embedded in air.

For solar cell applications one needs that  $\sigma_s$  is as large as possible and  $\sigma_a$  is as small as possible, preferably close to 0. These are the main traits desired from a scattering agent for improving absorption in the active material. Fig. 9.1 shows the calculated  $\sigma_s$  and  $\sigma_a$  for a core-shell nanoparticle in vacuum with 34 nm SiO<sub>2</sub> and 28 nm Ag shell.  $\sigma_s$  is shown to be larger than 1 in the whole wavelength range of 325-800 nm. This means that throughout this range, the nano-particle scatters more power than is incoming on its diameter. This can happen due to a whirlpool effect similar to that discussed by Bashevoy *et al.* [15]. The presence of the antenna sucks in more power from a cross-section larger than its size.

Furthermore, it can be seen in Fig. 9.1 that the power that is captured is mostly scattered and not absorbed. This is shown by the fact that nowhere in the range from 400-800 nm does  $\sigma_s$  become smaller than  $\sigma_a$ , even at the resonance. At wavelengths larger than 390 nm,  $\sigma_a$  goes below 50% and decreases rapidly to 0 while  $\sigma_s$  drops more slowly and is still around 3 even at 800 nm wavelength. This suggests that the nano-antenna still acts as a fairly good scatterer even at longer wavelengths far from its plasmonic resonance. Thus, a broad absorption enhancement can occur even for wavelengths above 800 nm.

Apart from having a good scattering capability we have to make sure that the scattered light enters the active material. In addition, one also needs to deal with Fabry-Perot effects of the solar cell multilayer system to ensure optimum light trapping.

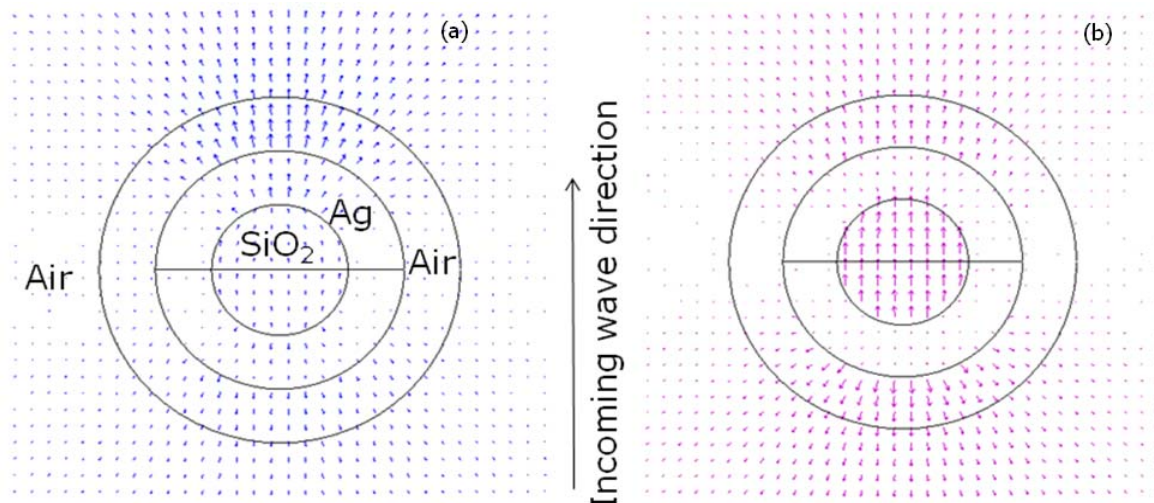


Figure 9.2. Scattered power profile from the nano-antenna: (a) at resonance ( $\lambda = 445$  nm) and (b) off resonance ( $\lambda = 600$  nm).

To see where the nano-antenna should be placed in our solar cell structure, a 2D COMSOL simulation to examine the scattered power profile is performed. Fig. 9.2 (a) shows the scattered Poynting vector at the resonance wavelength 445 nm and Fig. 9.2 (b) shows the same at 600 nm. The additional circle outside the nano-antenna is used for  $\sigma_s$  calculations. The incoming wave direction on this figure is from the bottom to the top. At resonance, forward scattering is more dominant than backward scattering indicated with bigger arrows at the upper part of the sphere in Fig. 9.2 (a). Off resonance, the backward and the forward scattering are quite similar. It is seen in both figures that the scattered power is well spread to all directions except the horizontal. It is significant that the nano-antenna does not preferentially backscatter light.

Putting these things into consideration, it is highly recommended to put these nano-antennas on the front contact. One can further optimize the absorption by engineering the cell's Fabry-Perot conditions (which also diminishes back-scattering). This is done by engineering the thicknesses of the multilayer system. Putting the nano-antennas in the middle of the active layer is also an option, although it is technologically much harder to accomplish.

## IX.2. Enhanced light absorption by a single nano-antenna

The cross-section of the solar cell with a nano-antenna placed on the top is sketched in Fig. 9.3. The refractive indices of materials used in all simulations are taken from Ref. [16]. Here, we show a proof-of-principle, where we took for the thickness of the a-Si layer 300 nm in view of its high absorption efficiency from the solar spectrum AM 1.5G and this a-Si thickness was also usually used by other authors in literatures [17]. Fig. 9.4 depicts the absorption enhancement in SCs with nano-antennas for varying sizes of the SiO<sub>2</sub> core and the Ag shell. The absorption enhancement is defined as follows:

$$\frac{\sum_{\lambda} A_{nanoantenna}(\lambda) - \sum_{\lambda} A_0(\lambda)}{\sum_{\lambda} A_0(\lambda)} \times 100\%, \quad (9.1)$$

where  $A_{nanoantenna}$  and  $A_0$  are the absorption in the active layer with and without antenna as a function of wavelength, respectively. The absorption in the active layer is calculated by integrating the Poynting vector (power flow) in the active region which we then normalize with input power. All simulations were done by 2D COMSOL with transverse magnetic (TM) polarization.

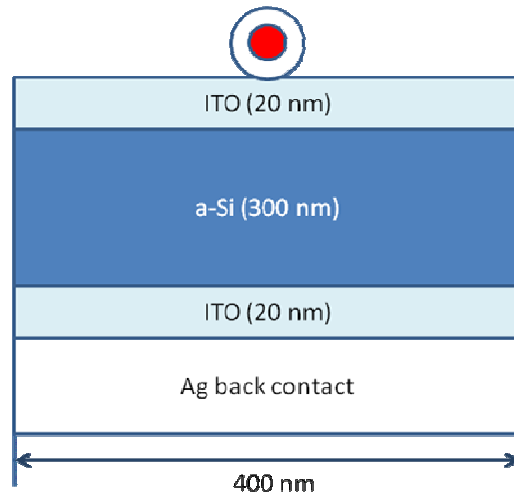


Figure 9.3. Geometry of the investigated amorphous Si solar cell with a core-shell nanosphere placed on top.

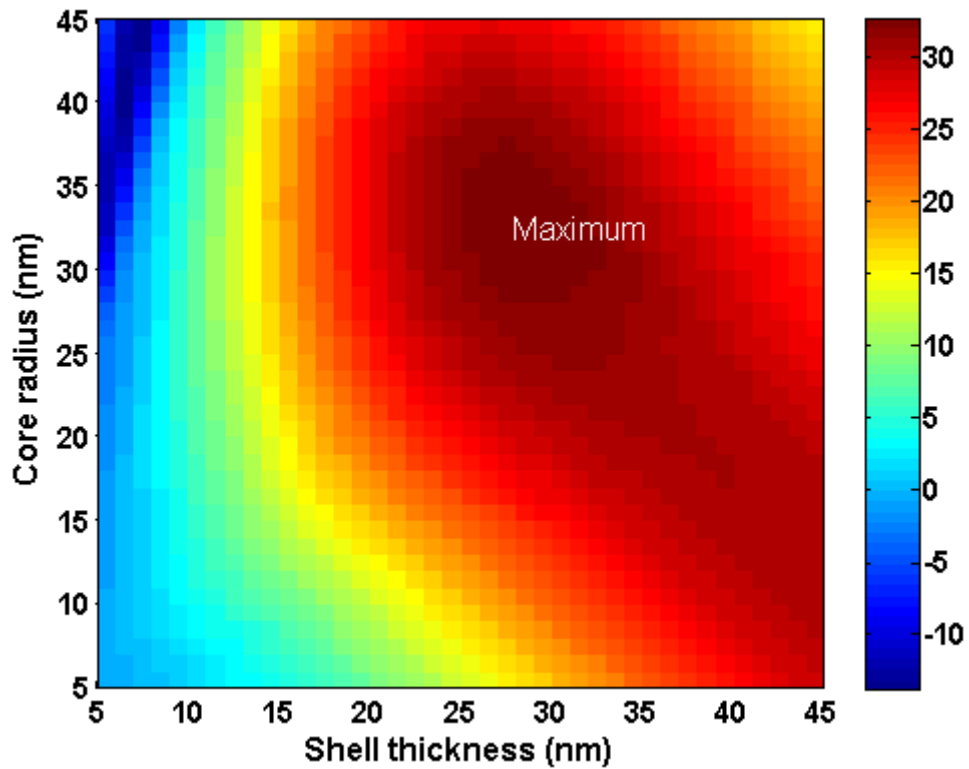


Figure 9.4. Absorption enhancement (%) of the investigated SC as function of core radius and shell thickness of nano-antennas.

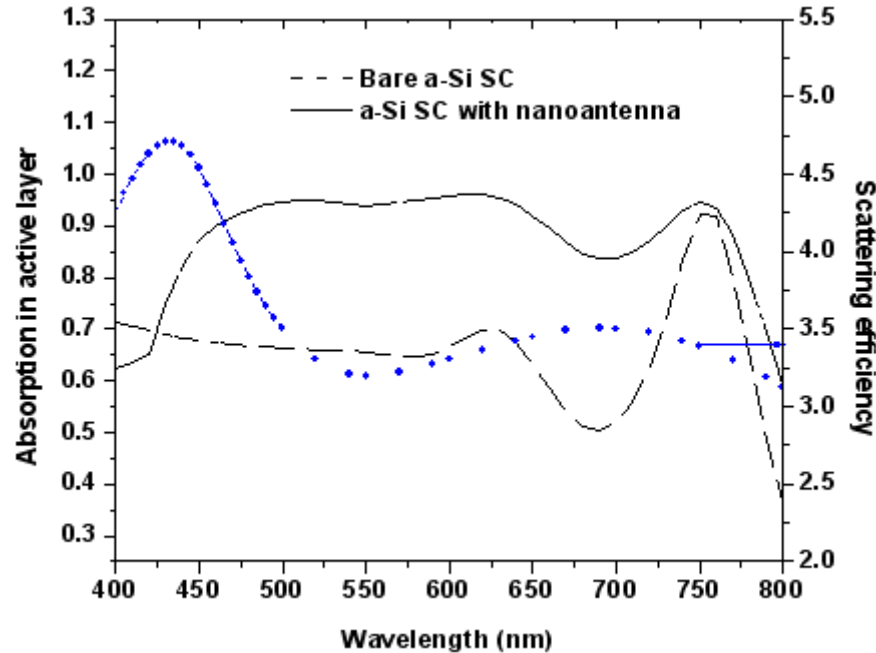


Figure 9.5. Light absorption in the active layer of the SC with and without adding a nano-antenna on top (black lines) and the scattering efficiency of the core-shell nano-antenna (blue line).

It is found that a maximum enhancement up to 33 % can be obtained at the optimal size of the antenna consisting of 34 nm core radius and 28 nm shell thickness. This enhancement is attributed to resonant light scattering of the core-shell nanostructure, which functions as an antenna. From Fig. 9.5 broadband absorption enhancement can be observed when adding nano-antennas on top of the SC. The same figure shows the scattering efficiency of the core-shell antenna in air. It is seen that the core-shell antenna has a high scattering efficiency in a wavelength range larger than the resonant scattering wavelength  $\lambda=445$  nm. Furthermore, the core-shell antenna has a second resonant wavelength at 690 nm. So, nano-antennas in SC can lead to a broadband absorption enhancement. This may be the reason why the high enhancement up to 33 % when using nano-antennas is obtained.

### IX.3. Conclusion

In this chapter, the use of the core-shell nanostructures to enhance light absorption in thin-film a-Si solar cells has theoretically been proposed. Through the interaction of incident light waves with core-shell antennas, broadband absorption enhancement was achieved. An integrated absorption enhancement up to 33 % in the 400-800 nm was demonstrated.

# References

1. K. R. Catchpole and S. Pillai, "Surface plasmons for enhanced silicon emitting diodes and solar cells," *J. Lumin.* **121**, 315-318 (2006).
2. K. R. Catchpole and A. Polman, "Plasmonic solar cell," *Opt. Express* **16**, 21793-21800 (2008).
3. H. A. Atwater and A. Polman, "Plasmonics for improved photovoltaic devices," *Nature Mater.* **9**, 205-213 (2010).
4. W. Wang, S. Wu, K. Reinhardt, Y. Lu, and S. Chen, "Broadband light adsorption enhancement in thin-film silicon solar cells," *Nano Lett.* **10**, 2012-2018 (2010).
5. R. A. Pala, J. White, E. Barnard, J. Liu, and M. L. Brongersma, "Design of plasmonic thin-film solar cells with broadband absorption enhancements," *Adv. Mater.* **21**, 3504-3509 (2009).
6. C. Haase and H. Stiebig, "Thin-film silicon solar cells with efficient periodic light trapping texture," *Appl. Phys. Lett.* **91**, 061116 (2007).
7. R. Dewan, M. Marinkovic, R. Noriega, S. Phadke, A. Salleo, and D. Knipp, "Light trapping in thin-film silicon solar cells with submicron surface texture," *Opt. Express* **17**, 23058-23065 (2009).
8. S. Pillai, K. R. Catchpole, T. Trupke, and M. A. Green, "Surface plasmon enhanced solar cells," *J. Appl. Phys.* **101**, 093105 (2007).
9. C. Rockstuhl, S. Fahr, and F. Lederer, "Absorption enhancement in solar cells by localized plasmon polaritons," *J. Appl. Phys.* **104**, 123102 (2008).
10. F. J. Tsai, J. Y. Wang, J. J. Huang, Y. W. Kiang, and C. C. Yang, "Absorption enhancement of an amorphous silicon solar cell through surface plasmon-induced scattering with metal nanoparticles," *Opt. Express* **18**, A207-A220 (2010).
11. H. Shen, P. Bienstman, and B. Maes, "Plasmonic absorption enhancement in organic solar cells with thin active layers," *J. Appl. Phys.* **106**, 073109 (2009).
12. Khai Q. Le, A. Abass, B. Maes, and P. Bienstman, "Plasmonic nano-antennas for absorption enhancement in thin-film Silicon solar cells," 3<sup>rd</sup> NANOMETA, Austria (2011).

13. I. Charamisinau, G. Happawana, G. Evans, A. Rosen, R. A. Hsi, and D. Bour, "Semiconductor laser insert with uniform illumination for use in photodynamic therapy," *Appl. Opt.* **44**, 5055-5068 (2005).
14. S. Ghadarghadr, Z. Hao, and H. Mosallaei, "Plasmonic array nanoantennas on layered substrates: modeling and radiation characteristics", *Opt. Express* **17**, pp. 18556-18570 (2009).
15. M. V. Bashevoy, V.A. Fedotov, and N. I. Zheludev, "Optical whirlpool on an absorbing metallic nanoparticle", *Opt. Express* **13**, pp. 8372-8379 (2005).
16. E. D. Palik, "Handbook of optical constants of solids," Academic Press: Orlando, FL, 1985.
17. W. Bai, Q. Gan, F. Bartoli, J. Zhang, L. Cai, Y. Huang, and G. Song, "Design of plasmonic back structures for efficiency enhancement of thin-film amorphous Si solar cells," *Opt. Lett.* **34**, 3725-3727 (2009).

# Chapter X

## Summary and perspectives

### X.1. Summary

This dissertation consists of two different parts. The first part is dedicated to improving the wide-angle beam propagation method, a widely used technique for the design and simulation of guided-wave photonic devices. Such a method is conventionally based on Padé approximant operators. Its widespread use is undoubtedly attributed not only to its accuracy but also to its simplicity and ease of implementation. However, conventional Padé approximant operators fail to properly address evanescent modes. In order to circumvent this issue, we proposed a novel class of approximants, the so-called modified Padé approximant operators. Such new operators not only allow more accurate approximations to the true Helmholtz equation than the conventional operators, but also give evanescent modes their desired damping.

Furthermore, we have shown that these new operators can also be used for time-domain beam propagation problems. Such time-domain methods enable the propagating analysis of reflective structures and model ultrashort pulses propagating in wide-angle waveguides. Through comparisons to results based on conventional operators the usefulness of the new operators has been demonstrated. They offer the advantages of using larger propagation resolution for the same accuracy with an associated reduction of computational times.

In addition, through an adaptation of the recently introduced CJI method for the solution of wide-angle beam propagation we have developed a very promising alternative method for demanding problems. For large 3D waveguide problems with refractive index profiles varying in the propagation direction, the CJI method can speed-up beam propagation up to 4 times compared to other state-of-the-art methods including GMRES and Bi-CGSTAB. The resulting CJI-WA-BPM has also been extended to higher-order Padé-based and semivectorial WA-BPM. It was also employed for the analysis of nonlinear propagation problems. Through benchmark results it was demonstrated convincingly that the resulting method is very competitive for demanding problems. As a final task, the CJI-WA-BPM has been integrated into the LightPy framework. Such an integrated module is very useful for those who want to design and simulate practical guided-wave photonic devices.

Apart from WA beam propagation problems for uniform waveguide structures, a novel Padé approximate solution for wave propagation in graded-index metamaterials has been developed. The resulting method offers a very promising tool for such demanding problems.

The second part of the dissertation is focused on the study of improved performance of optical devices including label-free optical biosensors, light-emitting diodes and photovoltaic devices by means of numerical and analytical methods.

For silicon-on-insulator surface plasmon interference biosensors we have proposed to add an additional silicon top layer to enhance their sensitivity. An enhanced sensitivity up to 5 times has been obtained.

Furthermore, we have developed an improved model to investigate enhanced light emission of silicon light-emitting diodes by isolated metallic nanoparticles. The resulting model for demanding problems is not only in good agreement with experiments but also allows to study the influence of a random assembly of uncoupled nanoparticles on light emitting devices.

Finally, we studied enhanced light absorption of solar cells. We have proposed to use the core-shell nanostructure as a nanoantenna to improve light absorption of thin-film amorphous silicon solar cells up to 33 %. Such a new structure offers another promising approach to improve performance of solar cells.

## **X.2. Perspectives**

It is seen that the CJI method has the ability to significantly speedup WA beam propagation. The resulting CJI-WA-BPM is excellent for the analysis of 3D optical waveguides with refractive index profiles varying in the propagation direction. For scalar problems, a straightforward implementation performs well. For the semi-vectorial CJI-WA-BPM where polarization effects are taken into account, in order to stabilize it we proposed to use an extra algorithm called the iterated Crank-Nicholson scheme. However for full-vectorial CJI-WA-BPM where the polarization effect and the coupling between field components are included, the stabilization is still challenging. We have tried to address these issues, but without success at this time. Since this is a very challenging problem, new algorithms should be developed. That may be the topic for further work to improve the CJI-WA-BPM. The same problem also occurred when we tried to develop a bi-directional version of CJI-WA-BPM.

In addition, there are several topics that could be the subject of further work. Parallelisation of the algorithms proposed may lead to very powerful 3D WA-BPM models. Another future

topic of interest can be the development of CJI-WA-BPM for metallic waveguides. With modified Padé operators the CJI-WA-BPMs performed propagation in 3D metallic structures with improved stability and accuracy than those based on the conventional one. However, compared to the other existing methods such as the EME and FDTD method the resulting CJI-WA-BPM is very slow for demanding problems. Therefore, extra work should be done to improve the convergence rate of CJI for metallic structures.

Moving to the studies of a surface plasmon interference biosensor, up to now the enhancement sensitivity is only demonstrated theoretically. The fabrication and experimental demonstration is obviously a further topic of interest. Furthermore, the use of an extra absorbed layer can be a potential approach to improve the sensitivity of other existing optical biosensors.

In order to investigate the influence of spherical nanoparticles on light emission of LEDs, an improved model based on the effective mode volume theory has been developed. Such a model can undoubtedly be applied to more general LEDs. Also, the core-shell structures studied in the context of solar cells could be useful for LEDs too, which could also be a topic of further interest.

Apart from using core-shell structures to enhance light absorption of solar cells, there are several other promising ways to improve light absorption. Recently, a high-performance optical absorber based on plasmonic metamaterials has been proposed [1]. These structures can be applied to the back structures of solar cells to get light reflected into active region to improve light absorption. In addition, tailoring the front contact of solar cell with triangular gratings is another option to achieve enhancement. All of these proposals can be the subject of further work.

## References

1. J. Hao, J. Wang, X. Liu, W. J. Padilla, L. Zhou, and M. Qiu, "High performance optical absorber based on a plasmonic metamaterial," *Appl. Phys. Lett.* 96, 251104 (2010).

